Polyoxometalates-Functionalized Electrodes for (Photo)Electrocatalytic Applications: Recent Advances and Prospects

Bruno Fabre, Clement Falaise, Emmanuel Cadot

Polyoxometalates-Functionalized Electrodes for (Photo)Electrocatalytic Applications: Recent Advances and Prospects

Bruno Fabre*,[1] Clément Falaise[2] and Emmanuel Cadot[2]

[1] *Univ Rennes, CNRS, ISCR (Institut des Sciences Chimiques de Rennes)-UMR 6226, F-35000 Rennes, France*

[2] *Institut Lavoisier de Versailles (UMR-CNRS 8180), UVSQ, Université Paris-Saclay, 45 Avenue des Etats-Unis, 78000 Versailles, France*

Outline

1. Introduction and Scope.

Polyoxometalates (POMs) represent one class of fascinating compounds largely explored in inorganic chemistry, highlighted by the large number of complexes with structural and functional diversities which have been discovered in the last twenty years.[1,2,3,4] POMs can include in their molecular framework many elements in a wide range of structures with various electronic configurations and bonding patterns which can impart an unmatched and tunable range of physical and chemical properties.[5] However, the capacity of POMs to exchange electrons is really one of the most striking properties which make them a relevant class of efficient electrocatalysts for a wide range of significant reactions, from hydrogen evolution reaction (HER) to multi-electron CO_2 reduction.[6–10] Interestingly, depending on the targeted electrochemical reaction and the desired selectivity, the structure, the composition and the functionalization strategy of the POM assembly can be tailored in an appropriate way. Furthermore, these discrete anionic molecules, often described as soluble oxide analogues, can be easily and durably attached to (semi)conducting (photo)electrode surfaces, using different immobilization procedures such as the chemical grafting on surface, the electrostatic entrapment within polymer films, the dispersion within porous materials or the incorporation as building blocks in extended 3D networks. Provided that the key properties of POMs, in particular electrochemical, are not degraded after their transfer from the solution to the electrode surface, and that the POMs are not released from the electrode surface under operating conditions, POMs-functionalized surfaces appear to be excellent candidates for promoting efficiently supported multi-electron electrocatalysis with attractive potentialities directed toward the development of electroanalytical and biosensing devices.

This review is intended to provide an up-to-date description of recent advances since the mid-2010s in the elaboration and the involvement of POMs-functionalized (photo)electrodes in (photo)electrocatalytic reactions. Only POMs irreversibly attached through strong interactions

(covalent, electrostatic, supramolecular and chimisorption) will be considered in this manuscript and homogeneous electrocatalytic reactions promoted by dissolved POMs will not be discussed. The Section 2 will give an overview of the most striking properties exhibited by POMs with particular emphasis on their electrochemical properties and their ability to be engineered to build complex assemblies with wide structural diversity. Section 3 will provide a state-of-the-art of recent and diverse immobilization procedures used to durably attach POMs to both conducting and semiconducting electrode surfaces. Effects of both the attachment method of POMs and the nature of the underlying electrode surface on the electrocatalytic activity of the resulting POMs-modified electrodes will be then scrutinized and discussed in the following sections 4 to 6. Finally, the last section will give some concluding remarks and will propose future investigation avenues to exploit the most promising (photo)electrocatalytically active (photo)electrode/POMs assemblies for the development of sensitive and selective POMs-based electrochemical sensors, electroanalytical devices and efficient solar-driven fuel cells.

2. POMs as Electrocatalytically Active Multiredox Centers

POMs are anionic metal oxide species mostly composed of redox metal centers (Mo, W, or V) in their highest oxidation states .[11] These electron-poor molecular units are usually formed from condensation of the basic oxometalates, generally the tetraoxoanions $[MO_4]^{n-}$, in acidic medium giving connected $\{MO_n\}$ polyhedra through corner or edge shared junctions.[11] POMs have emerged as an appealing class of molecular catalysts and redox mediators for catalytic systems involving multi-electron and/or multi-proton transfers. In this section, the most important properties of the POMs illustrated by representative examples will be described. This includes critical discussions about *i*) the relationship between the redox activity and the structure properties, *ii*) the tunability of the redox properties and the proton-coupled electron transfer, *iii*) the intra- and intermolecular electron transfers, *iv*) the electron-storage capacity, *v*) the ability of vacant POMs to coordinate catalytically-active metal centers or clusters and *vi*) the supramolecular and self-assembly properties of POMs, that emerge from their unique solvation properties.

2.1. Structure- redox activity relationship of native POMs

To develop stable POM-based electrocatalysts, it is often required to use POMs exhibiting reversible or pseudo-reversible redox activity that arises from the empty and non-bonding d orbital of the metal centers. The structural features of POMs, especially the nature of the building metal polyhedral of the metal-oxo frameworks, are closely link to their redox-properties. This observation was first done by Pope who proposed, in 1972, a classification of POM structures into three types.[12] Since this historical classification, considerable advances of structural chemistry of POMs, result in extending the Pope's classification to six types (see Figure 1).

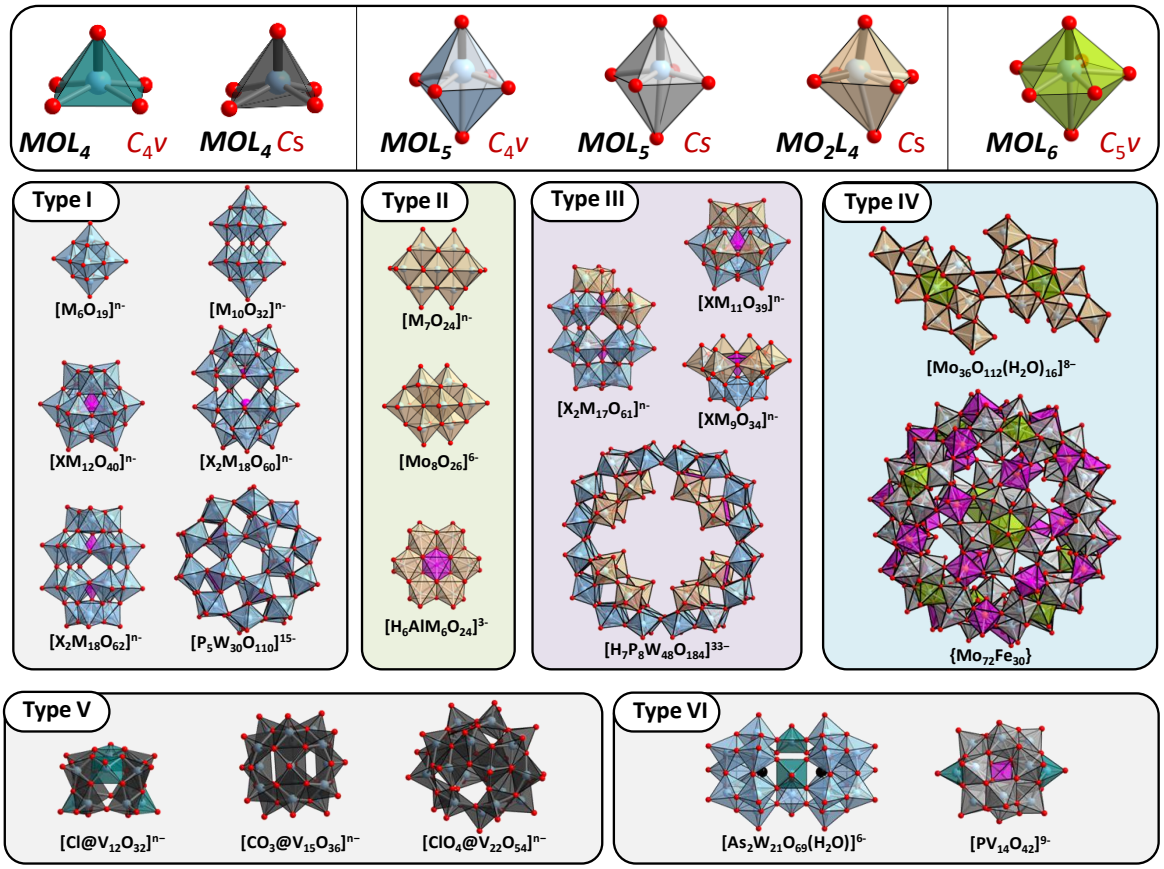

Figure 1.The principal broad POM subsets ordering based on the point group of the polyhedra MO_XL_y of the POMs (O: oxygen atoms doubly bonded to the metal center; L = oxygen atoms singly bonded to the metal center). Type I: POMs built from octahedra MOL_5 with C_{4v} symmetry. Type II: POMs built from octahedra MO_2L_2 with C_s symmetry. Type III: POMs built from both octahedra MO_2L_2 with *Cs* symmetry and octahedra MOL_5 with C_{4v} symmetry. Type IV: POMs exhibiting at least one pentagonal bipyramid MOL_6 with C_{5v} symmetry. Type V: POMs built exclusively on square pyramids MOL_4; Type VI: POMs built from assembly of square pyramids MOL_4 and octahedra. The pink polyhedral represents heteroatoms X (e.g. P^V, Si^{IV}, B^{III}, Al^{III}…).

The first class, named Type I, represents all POMs in which all metalate centers (mostly Mo^{6+} or W^{6+}) are in octahedral sites with a single unshared oxygen atom (MOL_5 with C_{4v} symmetry). Illustrative examples of this family are the Lindqvist $[M_6O_{19}]^{n-}$, the Keggin $[XM_{12}O_{40}]^{n-}$, the Dawson $[X_2M_{18}O_{40}]^{n-}$ or the Preyssler-type anion $[P_5W_{30}O_{110}]^{15-}$. Type I POMs exhibit reversible redox activity, and their reduction leads generally to mixed-valence POMs with delocalized electrons over the metals. The second structural type, namely Type II, correspond to the polyoxoanions built from addenda atoms with two mutually *cis* M=O bonds (MO_2L_4 with C_s symmetry). These POMs do not exhibit reversible redox process because their reduction involves the addition of electrons into anti-bonding orbitals, producing important

structural rearrangement of the polyanion. Type II archetypes are Anderson-type POMs or the heptamolybdate $[Mo_7O_{24}]^{6-}$. The POM structures built from MO_2L_4 octahedra with C_s symmetry and with MOL_5 with C_{4v} symmetry, such as lacunary Keggin ($[XM_{11}O_{39}]^{n-}$, $[XM_9O_{34}]^{n-}$) or the macrocyclic-based POMs $[H_7P_8W_{48}O_{184}]^{33-}$, lie on the structural type III. These POMs are particularly interesting in the frame of (photo)electrocatalytic applications because *i*) they exhibit redox activity similarly to the Type I POMs, and *ii*) they exhibit nucleophilic oxygen atoms that are able to coordinate a large variety of transition metals and catalytically-active metal atom clusters, making them particularly interesting for rational development of molecular electrocatalysts (see section 2.5).[13–17] The type IV represents the POMs containing the pentagonal bipyramid MOL_6 with a C_{5v} symmetry. Such polyhedra have been identified as a key building block for the construction of giant POMs including molybdenum wheels ({Mo_{154}}, {Mo_{176}}…), Keplerate anions ({$Mo_{72}Fe_{30}$}, {Mo_{132}}…).[18] While these POMs can contain mixed valence M^V/M^{VI} metals, no investigation has demonstrated, so far, that such POMs may exchange reversibly electrons. The structural type V corresponds to the POMs exclusively built on square pyramids MOL_4. Such POMs, are mostly built on vanadium based hollow arrangements encapsulating a wide variety of anions (CO_3^{2-}, Cl^-, I^-, SCN^-, ClO_4^{2-}…).[19] Such redox-active compounds are rarely described in aqueous solution,[20] recent works demonstrate however these POMs are able to undergo a large number of successive mono-electronic exchange in organic media. For example, the spherical POM $[I@V_{18}O_{42}]^{5-}$ exhibits eight redox events in acetonitrile.[21] Another illustrative example is $[Cl@V_{12}O_{32}]^{5-}$ capped by two Ca^{2+} cations that can undergo reversibly four mono-electronic redox processes while its uncapped analogue exhibits only a single reversible redox process.[22] Although the reasons of these contrasting electrochemical behaviors have not yet fully understood, the use of capping agents appears promising avenue to exploit further the redox activity of Type V POMs. The last structural type (Type VI) corresponds to the POMs resulting

from the condensation of octahedra MOL_5 and square pyramids MOL_4. They often exhibit rich redox activity, as evidenced for sandwich-like compounds $[(XW_9O_{33})_2(VO)_3]^{9-}$ with X= As^{III} or Sb^{III}.[23]

2.2. A tunable redox-active inorganic platform

Different older and recent reviews have discussed in depth how to tune the electrochemical properties of POMs.[24,25] In short, the electrochemical properties of POMs are mostly influenced by the global charge of the POMs, the metalate composition and its environment including nature of the solvent, the proton concentration (pH), the cation concentration (this parameter affects mostly redox properties of POMs in organic solvents), and the presence of neutral additives (macrocyclic host, polymers, proteins…) able to desolvate at least partially the POM units through the formation of supramolecular adducts or aggregates.

The first reduced states of archetypal Type I POMs have been intensively studied and are now well described. It was shown that the first reduction potential of Keggin type POMs, $[XM_{12}O_{40}]^{n-}$ with X= Mo^{VI} or W^{VI}, are mostly controlled by negative overall ionic charge (*n*) of the POMs. This is easily tuned by changing the central heteroatom X (P^V, Si^{IV}, B^{III}, Co^{II}...). As revealed by Pope, the reduction potential of $[XW_{12}O_{40}]^{n-}$ anion decreases linearly when the global charge increases (about -180 mV per unit charge).[26] The magnitude of the effect of the overall charge of POMs on the first electron-reduction process appears to be correlated with the POM size, as showed by systematic experimental and theoretical studies on the Preyssler anions $[M@P_5W_{30}O_{110}]^{n-}$, a POM-type structure with doughnut-shaped arrangement allowing encapsulation of various cations (M = Na^+, Ca^{2+}, Ln^{3+}, Th^{4+}…). It was observed the first redox potential varies with a slope of about 45 mV per charge unit.[27–29] This is four times lower than the slope observed for Keggin anions that are much smaller than the Preyssler anions (590 $Å^3$ and 1600 $Å^3$ for Keggin and Preyssler ions, respectively). Moreover the global charge of POMs also controls their ability to undergo proton-coupled reduction processes.[26] For instance, the reduction of the Keggin anions in acidic aqueous medium involves systematically its

protonation when the global charge reaches −6. The possibility of protonation makes electrochemical properties of POMs very sensitive to pH, not only in term of values of the half-wave potentials but also in the nature of the redox process. Keeping the overall charge constant, the nature of heteroelement of a Keggin anion exhibits a modest effect on the redox properties, as highlighted by comparison of the first redox potential of the Keggin anion $[XW_{12}O_{40}]^{5-}$ with $X = B^{III}$ (-491 mV *vs* Saturated Calomel Electrode, SCE), Al^{III} (-410 mV *vs* SCE) and Ga^{III} (-387 mV *vs* SCE).[30] Obviously, the metalate composition influenced notably the electrochemical behavior of POMs. For instance, the half-wave potential of the first mono-electronic event of a $[SiW_{11}MO_{40}]^{n-}$ with M = V(V), Mo(VI) or W(VI), increases in the following order: $[SiW_{12}O_{40}]^{4-}$ (-180 mV *vs* Ag/AgCl) < $[SiW_{11}MoO_{40}]^{4-}$ (+335 mV *vs* Ag/AgCl) < $[SiW_{11}VO_{40}]^{5-}$ (+440 mV *vs* Ag/AgCl). A large series of archetypal Keggin and Dawson type POMs with various compositions can be prepared from polycondensation of vanadium and molybdenum centers on the lacunary polyoxotungstates, allowing to cover a wide potential range.[31–34]

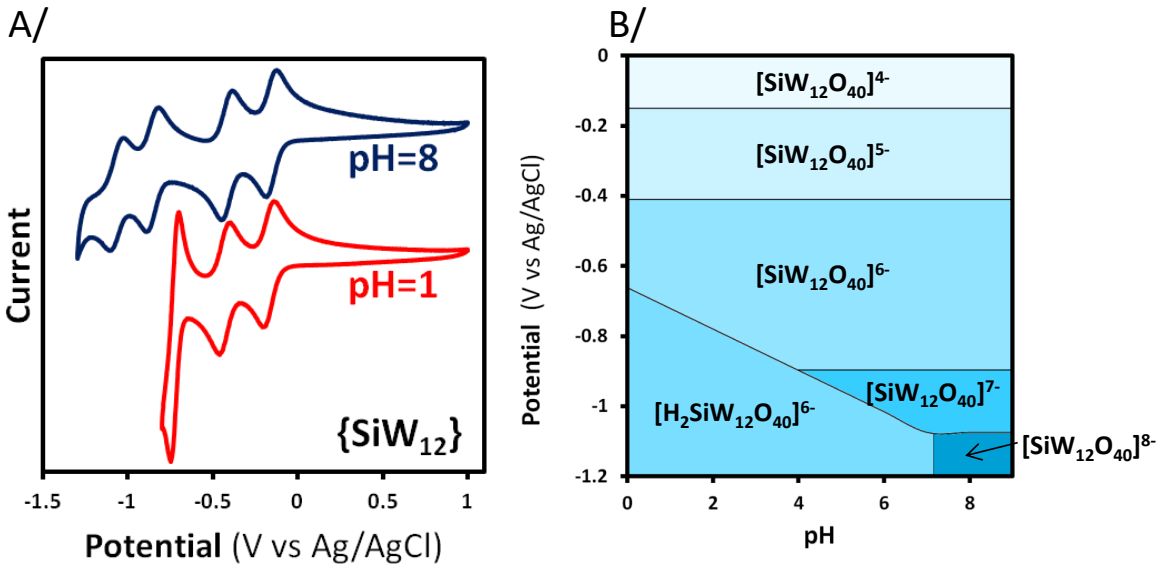

Figure 2. A/ Cyclic voltammograms of the dodecatungstosilicate at pH 1 and 8. B/ Potential-pH diagram of the dodecatungstosilicate $\{SiW_{12}O_{40}\}$.

To highlight the key role of pH on the electrochemical behavior of POMs, the archetypal Keggin-type dodecatungstosilicate can be selected as an illustrative example. Under acidic

conditions (pH < 4), the cyclic voltammogram (CV) of α-$[SiW_{12}O_{40}]^{4-}$ shows three quasi-reversible electron transfer steps (see Figure 2) involving one, one and two electrons for the first, the second and the third reduction waves, respectively.[35,36] The redox potential of the two first processes remains constant from pH 0 to 8, however notable changes are observed for the third one.[35] This third wave, corresponding to a two-electron reduction coupled with two protons (α-$[SiW_{12}O_{40}]^{6-}$ + 2e- + $2H^+$ → α-$[H_2SiW_{12}O_{40}]^{6-}$), shifts toward more negative potentials by about 59 mV per pH unit. For pH higher than 4, the two-electron processes are separated into two monoelectronic steps. As a consequence, the CV at pH 8 shows four distinct redox waves.[37] The redox behavior of dodecatungstosilicate in function of pH is quite representative of the proton-electron coupled phenomena observed for the archetypal Keggin- or Dawson-type POMs. For such entities, the pH decrease induces generally the merging of two mono-electronic waves into one two-electron wave due to the addition of two protons.

The redox behavior of POMs is also strongly influenced by the nature of the solvent.[38] For instance, the first redox wave of α-$[SiW_{12}O_{40}]^{4-}$ and $[P_2W_{18}O_{62}]^{6-}$ is shifted by about -957 and -992 mV, respectively, when dimethylformamide is used instead of water.[38] It is observed that the $E_{1/2}$ of the first redox wave shifts linearly to more negative potentials with decreasing solvent acceptor number which describes its Lewis acid properties.[38] In the presence of H^+ in organic solvent, the two first well-resolved one-electron processes of Keggin anions, such as $[PW_{12}O_{40}]^{3-}$, can converge into a single two-electron process.[39,40] Similar effects on the voltammetric behavior of POMs in organic solvents can be also observed thanks to the ionic pairing with alkali cations (Li^+, Na^+…). Indeed, it has been shown that the well-resolved one-electron transfer processes of Keggin-type POMs $[XMo_{12}O_{40}]^{n-}$ (X = P, Si) in acetonitrile, merged into a single two-electron process as the concentration of Li^+ or Na^+ was increased.[41] As a general trend, the presence of Li^+ or Na^+ facilitates the POM reduction process in organic solvent. This effect is much more pronounced for POMs exhibiting high charge density due to

stronger ion-pairing effects.[42] In contrast, the ion-pairing modifies weakly the redox properties of POMs in aqueous solution.[43] However, recent studies have evidenced that the use of neutral supramolecular additives provides tuning of POM redox properties in water. For instance, the encapsulation of POMs within neutral organic macrocycles (cyclodextrins) profoundly affects the voltammetric behavior of the inorganic guest, inducing significant shifts of the first redox event towards more negative potentials (up to -250 mV for $[PW_{12}O_{40}]^{3-}$).[44,45] In such systems, the stabilization of the oxidized form of the POM is a direct consequence of the chaotropic properties of the POMs (see Section 2.6 for details).

2.3. Electron delocalization: intra- and inter-molecular electron transfer

The electron delocalization is also an important feature of the reduced POMs and is crucial for the development of POM-based electrocatalysts because the fast intra-molecular mobility of the electrons makes efficient their transfer toward the catalytic sites, allowing multi-electron transfer reactions. It is also important to notice the POMs are able to provide inter-electron transfer not only in solution, but also in solid offering a way to increase, in some extent, the conductivity of the insulating porous catalytic matrices such as Metal-Organic Frameworks.

The introduction of electrons in polyoxomolybdates or polyoxotungstates leads to intense blue colored compounds in solution, usually named "heteropoly blues".[11] This class of mixed valence POMs belongs to the class II compounds according to the Robin-Day classification.[46] In such compounds, the added 'blue' electrons are delocalized over different metal sites of the polyanions owing to fast thermal hopping ($\sim 10^9$-10^{11} s^{-1}) at room temperature. Actually, this electron hopping can take place either by optical excitation or by thermally activated transfer, and consequently trapping of the 'blue' electron is then possible by limiting the thermally-induced vibrations of the polyanions. The UV-vis spectra of "heteropoly blues" exhibit broad and intense absorption for wavelengths higher than 600 nm which are due to intervalence charge transfers (IVCTs; $Mo^{V} \rightarrow Mo^{VI}$ or $W^{V} \rightarrow W^{VI}$).[47,48] The optical activation energy can be deduced

from the position of the IVCTs. The decrease of the temperature leads to the trapping of the electron of one metal center, as extensively evidenced by electron spin resonance (ESR) methods. In context, it was demonstrated the electron hopping rate strongly depends on the junction between adjacent MO_6 octahedra. More precisely, the delocalization of the electron appears easier through corner sharing octahedra that favor dπ-pπ orbital overlap. This conclusion arises mostly from ESR measurements of one-electron reduced archetypal POMs.[33,49,50] The ESR spectra of one-electron reduced Lindqvist anion $[M_6O_{19}]^{3-}$, a POM containing exclusively edge-shared MO_6 octahedra, exhibit hyperfine components for spectra recorded below 25 K and 117 K for the tungsten and the molybdenum derivatives, respectively. In contrast, the Keggin anions $[XW_{12}O_{40}]^{n-}$, that contain twelve WO_6 octahedra connected by corner -sharing junctions exhibit no hyperfine structure even at temperature near to 10 K, while for the molybdenum based Keggin anions, hyperfine structure remains resolved for temperature up to 45 K. This situation contrasts with that of many other POMs such as Dawson-type POMs or the decatungstate ion $[W_{10}O_{32}]^{4-}$. Figure 3a represents the electron delocalization pathway over the different metal centers with regard to the type of connections between the WO_6 octahedra. ESR experiments of the reduced Dawson anions revealed the added electron is mostly delocalized on the 12 equatorial metal centers; this conclusion is in full agreement with electrochemical and NMR data obtained for the two-electron reduced anion. For a "heteropoly blue" containing an even number of 'blue' electrons, antiferromagnetic spin coupling predominates leading to a diamagnetic behavior. For POMs exhibiting two non-equivalent metal sites, the extra 'blue' electrons are delocalized over the 8 and 12 equatorial metal centers of $[W_{10}O_{32}]^{6-}$ and $[P_2W_{18}O_{62}]^{8-}$, respectively.[51–53] The origin of this strong antiferromagnetic coupling between the pair of delocalized electrons has been debated.[51,54–57] Finally, Coronado and coworkers have demonstrated by *ab initio* calculations but also experimentally, that the

antiferromagnetic coupling mostly arises from the combination of spin density transfer and coulombic repulsion while the magnetic exchange has only a minor influence.[53,58,59]

In contrast to the electron mobility within aromatic-based organic systems, that is restricted mainly to 1D or 2D delocalization of the π electrons, the reduced polyanions exhibit 3D delocalization within a wide variety of patterns such as a twelve metal-based sphere (Keggin anions), a twelve metal-based barrel (Dawson), a cube (decatungstate) or an octahedral (Lindqvist anions). Lower dimension delocalization (1D or 2D) could be achieved using vanadium- or molybdenum-substituted polyoxotungstates. For instance, vanadium di-substituted Keggin anions such as $[SiMoV_2W_9O_{40}]^{7-}$ exhibit electron hopping between the two vanadium centers. Interestingly the protonation of the V−O−V bridge can cancel or reduce strongly the electron dynamics, making the two vanadium nuclei non-equivalent at the ESR time scale (see Figure 3b).[60] The study of trivanadium systems allows to evidence also that the electron hopping and delocalization occur through electron transfer either through the V−O dπ−pπ overlap when vanadium centers share corner, or through direct V−V d_{xy} interactions when the vanadium centers are connected by edge-shared junctions. In contrast to the di and tri-substituted systems, electron trapping is observed at room temperature for the vanadium or molybdenum mono-substituted systems.

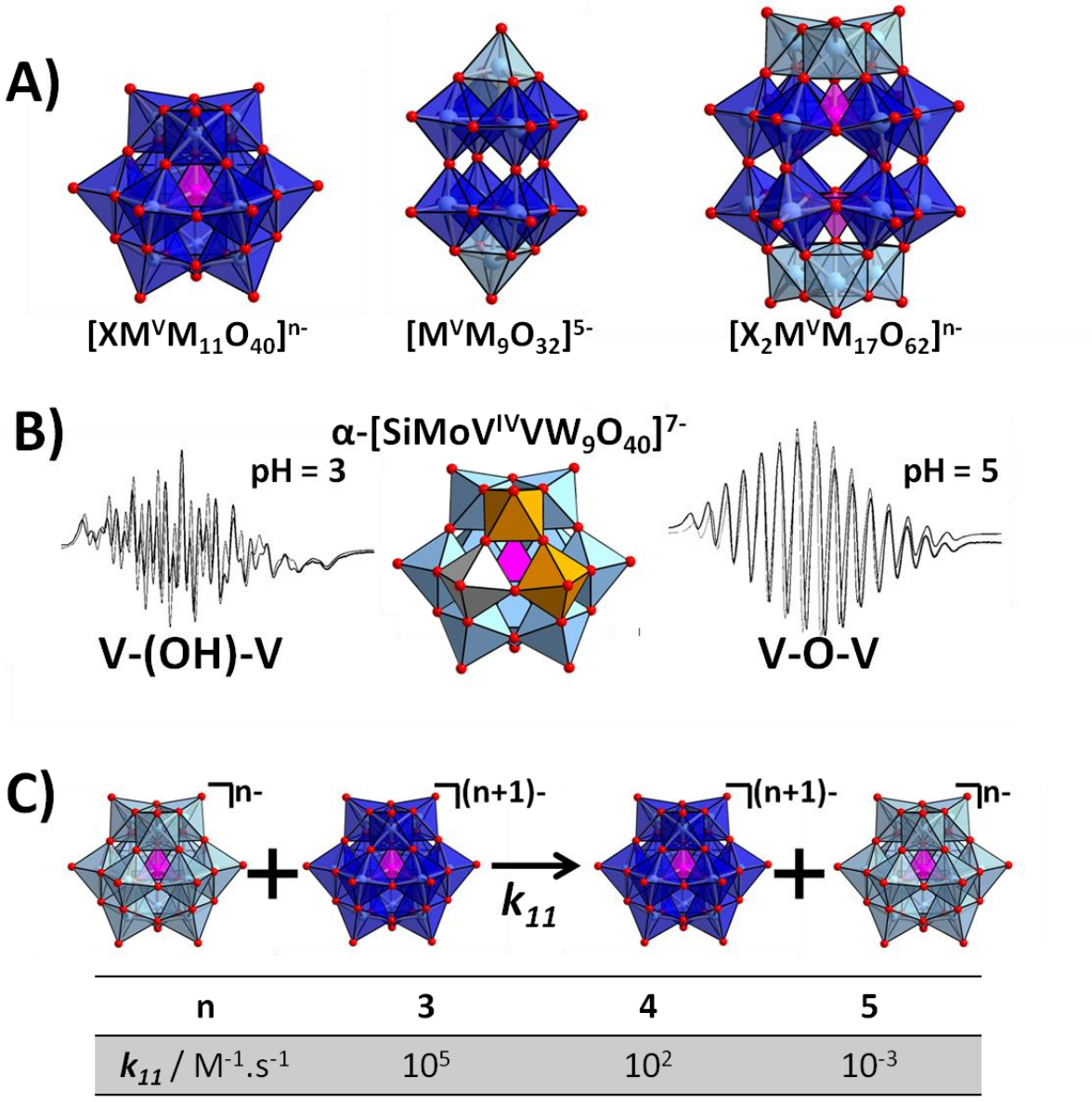

n	3	4	5
k_{11} / $M^{-1}.s^{-1}$	10^5	10^2	10^{-3}

Figure 3. A/ Illustration showing the electron delocalization of three reduced archetypal POMs. Dark blue polyhedral represents the metal centers involved in the electron delocalization. B/ Illustration showing the effect of the protonation on the ESR spectra of one-electron reduced Keggin α-$[SiMoV^{IV}VW_9O_{40}]^{7-}$, which prevent the electron hopping between the two vanadium centers. Adapted with permission from ref 60. Copyright 1996 American Chemical Society. C) Illustration showing the rate constant of the inter-electron transfer between Keggin-type POMs is dramatically associated to the overall charge of the interacting POMs.

Interestingly, the electron delocalization is not limited to the closed neighboring metalate centers since numerous studied have revealed the possibility of inter-molecular electron exchange occurring either in solution or in the solid-state. NMR is an appropriate tool to perform such phenomena in solution.[61–63] The ^{31}P NMR spectra of aqueous mixture of oxidized

and one-electron reduced dodecatungstophosphate $[PW_{12}O_{40}]^{3-}$/$[PW_{12}O_{40}]^{4-}$ have revealed that the exchange of the 'blue' electron is faster than the NMR time scale, as evidenced by the presence of single broad peak centered between the chemical shifts of oxidized and one-electron reduced POMs.[62] Quantitative analysis indicates that the rate constant ($k_{11;}$ Figure 3c) for electron self-exchange between $[PW_{12}O_{40}]^{3-}$ and $[PW_{12}O_{40}]^{4-}$ is about 10^5 M^{-1} s^{-1} at zero ionic strength which is in fairly good agreement with the calculated value using the Sutin's semi-empirical method.[64] In absence of ionic strength, the k_{11} for electron self-exchange between $[PW_{12}O_{40}]^{4-}$ and $[PW_{12}O_{40}]^{5-}$ is dramatically decreased to 10^2 M^{-1} s^{-1}. This trend is confirmed by the analysis of the inter-molecular electron transfer between the highly charged Keggin anions $[AlW_{12}O_{40}]^{5-}$ and $[AlW_{12}O_{40}]^{6-}$, indicating a k_{11} value about 10^{-3} M^{-1} s^{-1}. Obviously, increasing the electrostatic repulsions leads to the statistical decrease of collision frequency between the anions, that is manifested by the decrease of the self-exchange rate constants. Indeed, the formation of the "electron-tranfer" complexes $[[PW_{12}O_{40}]_{ox}\bullet\bullet\bullet[PW_{12}O_{40}]_{red}]^{7-}$ and $[[AlW_{12}O_{40}]_{ox}\bullet\bullet\bullet[AlW_{12}O_{40}]_{red}]^{11-}$ exhibit a significant difference in their coulombic energies (4.54 kcal mol^{-1} and 11.2 kcal mol^{-1} for P and Al- based systems, respectively).[61]

In contrast, 'blue' electron is not easily transported from one POM to another in the solid-state because of the strongly isolated electronic structures of the POM units intercalated by insulating cations. This is an important drawback for the development of electrodes based exclusively on POMs. This is why most electrodes used for (photo)-(electro)-catalysis required the use of conductive additives (e.g., black carbon). So far, only few investigations have been engaged to study the electron-transport properties in the solid-state and to improve their electrical conductivity. A systematic investigation of the charge-transport properties of $[S_2Mo^{V}_2Mo^{VI}_{16}O_{60}]^{6-}$ tetra-alkylammonium salts $[(C_nH_{2n+1})_4N]^+$ with various alkyl chain lengths (n = 2, 3, and 4) has revealed the electrical conductivity followed an Arrhenius-type behavior and decreased with increasing alkyl chain length of tetraalkylammonium (from ~10^{-8}

S cm^{-1} for n = 2 to ~10^{-12} S cm^{-1} for n = 4, at 300 K), suggesting the electron mobility in the solid is facilitated by shortening the inter-POMs distances.[65] Coordination assemblies of Preyssler anions bridged with transition metal cations lead to tunable, redox-active metal oxide frameworks with intrinsic conductivity seemingly to be controlled by the nature of the bridging metal. However, the resulting conductivity of such assemblies still remains quite moderate (up to 15 µS cm^{-1}).[66,67] Another strategy for increasing the electrical conductivity of POMs based crystalline solids consists in developing hybrid materials in which mixed valence POMs are electrically plugged to wires of cationic π-molecules (tetrathiafulvalene derivatives).[68]

2.4. POMs: an odd electron reservoir

In contrast to the well-documented knowledge on the first reduced states of POMs, only few are known on the highly reduced states of POMs. Actually, most of the state-of-art is limited to few electrochemical studies published 50 years ago by a group of French chemists from University of Paris (Souchay, Launay & Hervé, …),[36,37,69–76] that have revealed the archetypal Keggin-type POMs can accept a large number of electrons. Based on their observations, they have suggested the polyanions $[SiMo_{12}O_{40}]^{4-}$, $[BW_{12}O_{40}]^{5-}$, $[SiW_{12}O_{40}]^{4-}$, and $[H_2W_{12}O_{40}]^{6-}$ are able to be reduced, without any significant structural changes, by 12, 18, 20 and 32 electrons, respectively.[70,71,73,76] In contrast, the $[PW_{12}O_{40}]^{3-}$ anion cannot be reduced beyond six electrons. This relatively low electron accumulation appears surprising because its first redox wave is observed at higher potential than the other polyoxotungstates $[XW_{12}O_{40}]^{n-}$ with X = Si, B and H_2. Much more recently, Cronin and coworkers have shown that the Dawson-type POM $[P_2W_{18}O_{62}]^{6-}$ is an appealing water-soluble charge carrier because this POM can accept a high number of electrons which reaches 18 electrons per POM unit.[77] While the electron-storage mechanism within the Dawson-type POMs should retain still some misteries, the reduction process of the Dawson-type anion is associated to its protonation.

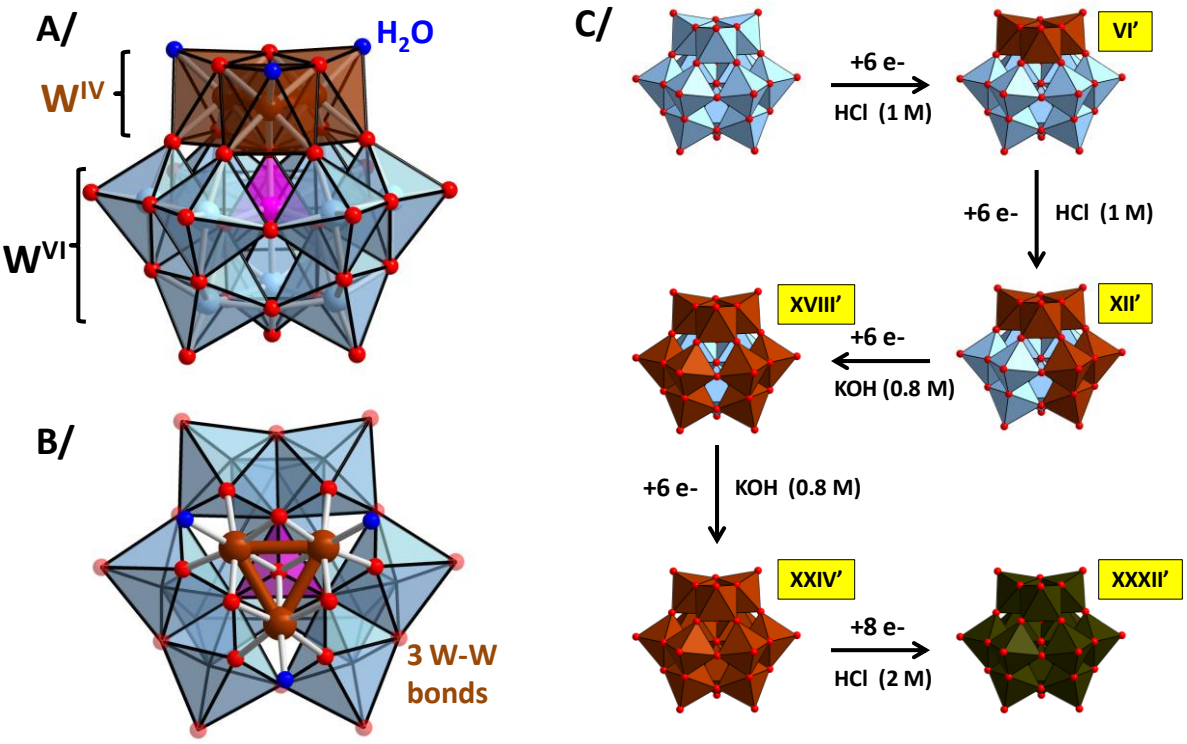

Figure 4. A) and B) Illustrations of the structure of the six-electron reduced "heteropoly brown" $[BW^{IV}_3W^{VI}_9O_{37}(H_2O)_3]^{5-}$ in which the six electrons are localized in a $\{W_3O_{13}\}$ triad. C) Illustration showing the different steps described by Launay to reduce through controlled potential electrolysis the metatungstate ions $[H_2W_{12}O_{40}]^{6-}$ up to the highly-reduced state containing up to 32 electrons per polyanion.

These pionnered studies have revealed the electrochemical reduction of Keggin anions in acid solution, especially the polyoxotungstates $[XW_{12}O_{40}]^{n-}$ with X = Si, B and H_2, can lead to the formation of a brownish six-electron reduced POMs that belong to the Robin-Day class I mixed-valence compounds. In contrast to the "heteropoly blues", the electrons within "heteropoly browns" appear located within three W-W bonds forming a W^{IV} based triad that have been clearly evidenced by ^{183}W NMR studies and X-ray diffraction analysis.[78–81] Interestingly, the structural analysis revealed the terminal oxygen atoms of the electron-rich metal triad are diprotonated such as water molecules (see Figure 4).[78,79] It must be mentioned the overall charge density of the "heteropoly browns" $[XW_{12}O_{37}(H_2O)]^{n-}$ is the same as that of the oxidized parent $[XW_{12}O_{40}]^{n-}$. The six-electron reduced POM belonging to the class "heteropoly browns" are denoted VI′ (the Roman numeral indicates the number of added

electrons) in order to differentiate them from the “heteropoly blues” denoted VI. So far, the knowledge about the mechanism of VI’ formation is limited but several processes have been proposed such as the disproportionation of the four-electron heteropoly blue according to equation 2 IV→ II + VI’.

The formation of the “heteropoly browns” is an important feature of the electron accumulation properties of POMs and should lead to important future developpements in electrochemical devices that required massive electrons transfer. In a seminal paper published in 1976,[71] Launay have observed that successive electrolyses at controlled potential can lead to the formation of highly reduced metatungstate anions $[H_2W_{12}O_{40}]^{n-}$ containing 6, 12, 18, 24 and 32 electrons. Figure 4 shows the different steps used to prepare such highly reduced compounds. It must be worth to mention that basic solutions were required to reduce the XII’ and XVIII’ species which are poorly soluble in acidic solution. Launay proposed the species VI’, XII’, XVIII’ and XXIV’ exhibited one, two, three and four electron-rich W^{IV}-based triads, respectively. According to the molecular orbital calculations developed by Cotton for the molecular clusters $\{M_3O_{13}\}$[82] Launay proposed that the XXXII’ species could be understand by filling of the non-bonding levels of the four electron rich triads $W^{IV}{}_3O_{13}$. Up to now, there is no report on the characterizations of the XII’, XVIII’ and XXII’ or XXXII’ “heteropoly browns” derivatives. The mechanism of the high reduction states formation for the $[H_2W_{12}O_{40}]^{6-}$ ion has been investigated by cyclic voltammetry.[83] Analysis of the experimental data suggests: *i*) the slow disproportionation reaction of IV gives the heteropoly brown VI’ and heteropoly blue II, and *ii*) the fast disproportionation of two-electron reduced heteropoly brown XII’ forms the heteropoly browns XII’ and XVIII’.

Although POMs are well-known "electron reservoirs" or electron sponges, the fundamental knowledge on the physico-chemical phenomena occurring during their reduction processes seems little known and probably deserves to be re-explored in order to optimize the use of

POMs in processes requiring the massive transfer of electrons, such as multi-electron electrocatalytic reactions as well as applications related to energy storage/conversion.

2.5. Modification of the intrinsic electrocatalytic properties of POMs.

2.5.1. Inclusion of redox active metallic centers within the POMs framework

As written above, the richness of the POMs chemistry arises from their capabilities to include in their framework almost all the elements of the periodic table belonging to the s-, d-, f- or p-blocks. Such a wide diversity in terms of composition gives rise to an extraordinary structural richness that originates mainly from the coordination capability of the addenda atoms (coordination number or the symmetry of the coordination sphere). Not only to expand further the redox-active scale of the mixed metal POM species, these addenda metal centers are able to behave as active catalytic centers, allowing the coordination of catalytic substrates to be further converted along the electrocatalytic process through electrons and/or protons transfer, e.g. CO_2, nitrite, nitrate or O_2 reduction. Actually, the mixed metal POM assemblies result from a main metal-oxo framework which includes the addenda atoms. This metal-oxo framework results from the conventional early elements of groups V and VI such as V^V, W^{VI}, Mo^{VI}, Nb^V or Ta^V and then constitutes the backbone of the molecular assembly. From a practical point of view, the synthesis of the mixed metal POM assemblies can be achieved either *i*) from sequential steps procedures that consist to react preformed molecular species, such as saturated or polyvacant POMs with metallic cations, coordination complexes or metallic clusters; or *ii*) through one-pot procedures. In any case, the formation of POM-based molecular species results from complex mechanisms and depends upon many parameters such as pH, ionic strength, nature of the counter-ions, temperature, concentration of the reagents, solvent, presence of weakly chelating ligands (sulfate, acetate…). Even if the chemist aims to control and rationalize to some extent the self-condensation processes that lead to the target species, it should be noted that the design of POM relies in many cases on serendipity. Actually, the high lability and the

dynamical character of the metal-oxo bonds give rise to highly subtle effects induced by ionic strength changes or solvent effects, which are difficult to be predicted. For instance, formation of the nano-sized and highly symmetric wheel-shaped molybdenum blue $\{Mo_{154}\}$, $\{Mo_{176}\}$, $\{Mo_{248}\}$ or $\{Mo_{360}\}$ results from one-pot bottom-up procedures by acidification of monomeric tetraoxomolybdate ions $[MoO_4]^{2-}$ under reducing conditions in aqueous solution.[84–87] The numerous successive elementary steps considered in the overall mechanism of growth must be continually and dynamically directed towards a convergent aggregation pathway leading in its ending step to highly symmetrical wheel-like or spheroidal assemblies. Furthermore, in these gigantic POM species, the high symmetry arising from ring-shaped or spheroidal arrangements suggests that solvent effects, involving water molecules of the hydration shell take place to minimize the POM-solvent interfaces. Actually, considering the close-compact spheroidal or ring-shaped structure of the archetypical POMs, such as the so-called Lindqvist, Keggin, Dawson, Preyssler or other conventional arrangements, solvent effects should be considered as a general and important structure-directing agent within the POM synthesis. Among the metallic addenda atoms which behave as active electrocatalytic sites in synergy with the POM framework, the 3d transition metals appear very popular. They are cheap, abundant and easy to manipulate. Furthermore, most of them are highly reactive as cationic divalent M^{2+} or trivalent M^{3+} species toward anionic POM species mainly with regard to their intrinsic hardness which make them oxophilic species. Then, Mn, Fe, Co, Ni, or Cu transition metals as cationic species were combined with polyoxometalate subunits leading to a wide variety of compounds wherein these elements appear as isolated centers in their POM matrix environment, clusterized as central aggregates or functionalized with specific exogenous ligands (different from oxo, hydroxo or aquo ligands). Thus, it would be tedious and probably unappropriated in the context of this review to give an exhaustive list of the plethoric mixed metal polyoxometalate compounds, therefore, only those built from tungsten-containing POM framework will be

considered because these robust molecular matrices exhibit redox activity on potential ranges in relationship with their electrocatalytic behavior.

The simplest chemical system that exemplifies nicely the coordination process between a cationic transition metal species and polyoxometalate ions relies on the chelating behavior of the monocavant polyoxotungstates such as the Keggin-type species α-$[XW_{11}O_{39}]^{n-}$ ($X = P^{V}$ or Si^{IV}) or the Dawson-type α_2-$[P_2W_{17}O_{61}]^{10-}$ (see Figure 5Aa). The di- or trivalent 3d transition metal reacts in such conditions to give the monomeric species $\{M(H_2O)(XW_{11}O_{39})\}$ or $\{M(H_2O)(P_2W_{17}O_{61})\}$, which contains both the aqua group $\{M\text{-}OH_2\}$. Actually, such a process can be extended to other vacant polyoxometalates, such as the divacant γ-$[SiW_{10}O_{36}]^{8-}$ or the tricavant α-A-$[XW_9O_{34}]^{n-}$ giving the corresponding saturated species (see Figure 5Ab-c) .[88–90] For instance, condensation of Fe(III) cation onto the mono-, di- or tricacant vacant tungsto-silicate pre-formed species can lead to the mono-, di- and tri-iron substituted species α-$[Fe(H_2O)(SiW_{11}O_{39})]^{5-}$, γ-$[(Fe(H_2O)O)_2(SiW_{10}O_{36})]^{6-}$ and α-$[(Fe(H_2O)O)_3(SiW_9O_{34})]^{7-}$, respectively (see Figure 5Ab-c). Furthermore, these terminal aquo groups are polarized enough to undergo ionization process that can induce controlled dimerization process of monomeric units into dimeric ones.[91,92] Such a process shows perfectly how the presence of 3d metallic cation embedded within the POM framework can extend the condensation process toward nanosized multi-modular assemblies. Therefore, changing the synthetic conditions such as pH or ratio between the 3d metal and the POM subunit allowed isolation of di-, tri-, tetra- and hexamodular species. For instance, the seminal work of Kortz showed that the archetypical cubane-type cluster $\{Ni_4O_4\}$ can be grafted onto the trivacant polyoxotungstate $\{PW_9\}$ subunit (see Figure 5 Ba).[93] This corresponding pseudo-cuboidal $\{Ni_4O_4\}$-supported POM unit was found as constitutional building blocks in many multi-modular nanosized derivatives. In addition, the presence of outer assembling groups, such as phosphate, silicate, borate or carboxylate expands the structural diversity of these arrangements. In this way, Ni_8- and Ni_{12}-

containing dimeric and trimeric species, respectively, were obtained wherein the surrounding POM modules consisted of the trivacant subunit A-α-$[SiW_9O_{34}]^{10-}$.[94] Besides, by changing the tricavant-type structure for the B-α-$[P_2W_{15}O_{56}]^{12-}$, derived from the Wells-Dawson anion, the condensation process led to a large tetrameric species containing the central $\{[Ni_{14}(OH)_6(H_2O)_{10}(HPO_4)_4\}$ core.[95] At last, very large and spectacular Ni_{25}- and Ni_{36}- hexameric assemblies were reported exemplifying nicely the common feature of such a class of mixed-metal compounds wherein the POM subunits act as modulator within the condensation of the 3d metallic cations, allowing the formation of well-defined polyoxo(hydroxo)aquo clusters $\{M_xO_y(OH)_z(H_2O)_w\}^{n+}$ surrounded by the protecting POM subunits.[96] Using similar approaches, many Co-[97–100], Mn-[101–103], Fe-[91,104–106] or Cu-containing[107–109] POMs have been reported, illustrating the high structural diversity in the resulting mixed metal arrangements in relationship with the synthesis conditions and the stereo-chemical and coordinating properties of the preformed POM subunits. Nevertheless, in the landscape of the 3d metal-containing POMs, some structural invariants appear independent of the nature of the 3d metal M with M = Cr, Mn, Fe, Ni, Co, Cu, Zn. Among these arrangements, there are the sandwich-type dimeric compounds based on the B-type trivacant moieties B-$[XW_9O_{33}]^{9-}$ (with X = As^{III}, Sb^{III} or Bi^{III})[110,111] that sandwiched three isolated $\{M\text{-}OH_2\}$ groups between two trivacant subunits. Besides, the Weakley-type compounds based on the B-type trivacant subunits deriving either from the Keggin-type B-$[XW_9O_{34}]^{n-}$ with X = Si^{IV} or P^{V} or the from Dawson derivative B-$[P_2W_{15}O_{56}]^{12-}$ contain four *in plane* metallic cations forming a $\{M_4(H_2O)_2\}$ cluster, in which the four metallic cations are held together by the terminal oxygen atoms of the two symmetric B-type trivacant subunits (see Figure 5 Da).[112–116] Furthermore, it should be mentioned also the Kreb's anion, which corresponds to another archetypical arrangement widely represented in the mixed-metal polyoxometalates chemistry (see Figure 5Ca-c).[117] This arrangement is composed of two trivacant B-β-$[SbW_9O_{33}]^{9-}$ subunit linked by four bridging groups which can vary in

their composition. This arrangement has been reported as the full tungsten-containing anion $[Sb_2W_{22}(OH)_2O_{74}]^{12-}$, while the two outer bridging groups $\{WO_2(OH)\}^+$ can be substituted by a large variety of divalent or trivalent metal cations giving the mixed metal derivatives $[M_2(H_2O)_6(WO_2)_2(SbW_9O_{33})_2]^{(14-2n)-}$ (M^{n+} = Fe^{3+} or Fe^{2+}, Co^{2+}, Mn^{2+}, Cu^{2+}, Ni^{2+}…) anions. At last, the arrangement of the Krebs' anion has been also reported with the presence of four Fe^{3+} metal cations sandwiched between the two B-β-$[XW_9O_{33}]^{9-}$, giving the general formula $[Fe_4(H_2O)_{10}(XW_9O_{33})_2]^{n-}$ where X = As^{III}, Sb^{III}, Se^{IV} or Te^{IV} (see Figure 5). Actually, various elements such as Co, Ni, Cu, Mn can be substituted within these four central positions.[115] In addition, the macrocyclic anion $[H_7P_8W_{48}O_{184}]^{33-}$ deriving from the connection of four $[H_2P_2W_{12}O_{48}]^{12-}$ units can be viewed as a supervacant anionic template. Actually, this macrocyclic anion exhibits high hydrolytic stability in a large pH range (1-9)[118] and can be easily manipulated in the presence of usual 3d metallic cations such as Fe, Co and Cu leading to striking large 3d metal clusters closely embedded within the macrocyclic anion (see Figure 5 Ea-b). Thus, $\{Cu_{20}\}$ or $\{Fe_{16}\}$-metal clusters were found firmly anchored within the macrocycle $\{P_8W_{48}\}$ while these 3d cations were bound together through hydroxo groups or sometimes through exogenous ligands such as azido group.[119,120] Otherwise, condensation reaction of the trivacant species $[AsW_9O_{33}]^{9-}$ in the presence of tungstate at pH = 4-5 leads to a spectacular macrocycle where four $\{AsW_9O_{33}\}$ subunits are held together by four cis-$\{WO_2\}^{2+}$ connectors.[121] The resulting compound $[MAs_4W_{40}O_{140}]^{28-}$ with M = K^+ or NH_4^+ exhibits four equivalent coordination sites while only two are available for divalent 3d cations due to a striking allosteric effect arising from a significant distortion of the POM framework upon the coordination processes of two Co^{2+} ions (see Figure 5 Ec).[122] Actually, this macrocyclic cryptate species reacts with other transition metals such as Ni^{2+},[123] VO^{2+},[124,125] Pd^{2+} [126] and Ln^{3+} [127] offering interesting redox and coordinating properties while its electrocatalytic properties

remain unexplored.

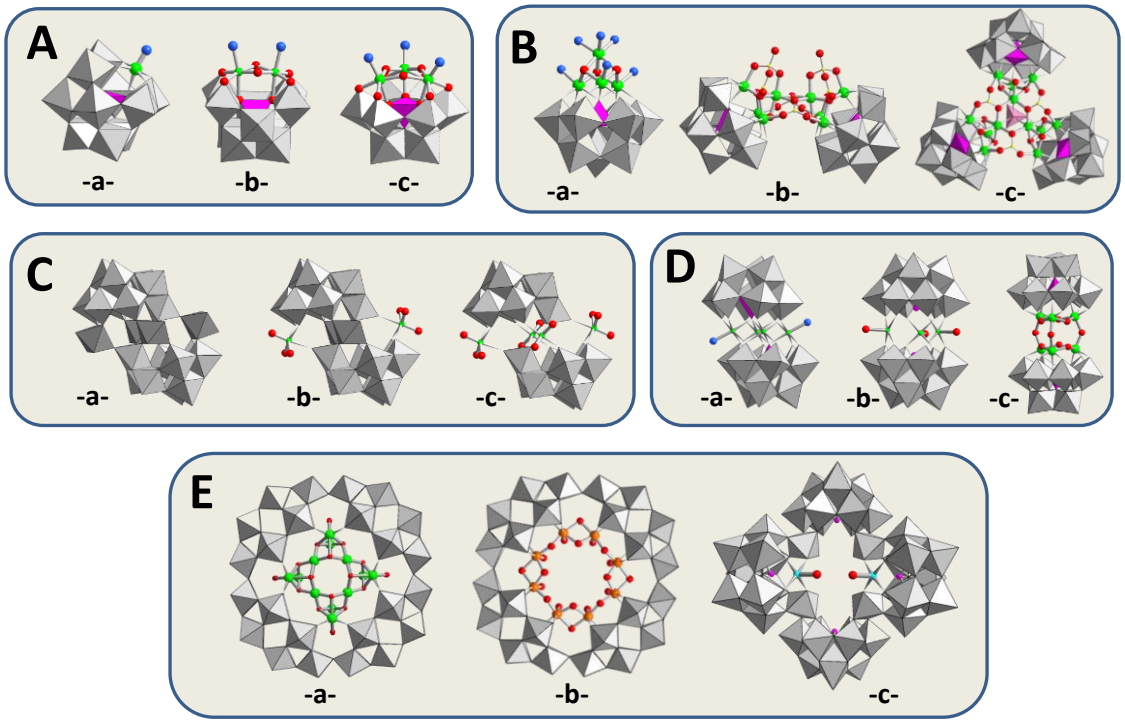

Figure 5. Selected mixed-metal POM assemblies based on various archetypical polyoxotungstate subunits. A) Transition metal containing mono-, di- and trisubstituted Keggin type anions. B) monomeric (a), dimeric, and trimeric (c) assemblies built from the $\{PW_9Ni_4\}$ building block. C) Krebs anions derivatives as full tungsten-containing species $[Sb_2W_{22}(OH)_2O_{74}]^{12-}$ (a); di-substituted (b) and tetrasubstituted anions (c). D) three different sandwiched-type compounds where a) two B-$\{XW_9O_{34}\}$ subunits (X = Si^{IV} or P^V) are held together by four transition metal cation in the weakley type arrangement, b) two $\{XW_9O_{33}\}$ (with X = As^{III}, Sb^{III} or Bi^{III}) are linked by three *d*-metal centres, c) two A-$\{XW_9O_{34}\}$(X = P^V, Si^{IV} or Ge^{IV}) are associated by a central $\{M_6O_9\}$ core. E) Macrocyclic POM arrangements based on the $\{P_8W_{48}\}$ assembly containing a) a central $\{Cu_{20}\}$ or b) $\{Fe_{16}\}$ cluster cores. c) $\{As_4W_{40}\}$ cryptate containing two isolated $\{M\text{-}OH_2\}$ groups.

2.5.2. Cluster containing polyoxometalates

Another route that leads to the POMs modification consists to associate preformed stable chemical units, such as clusters. According to the definition given by Cotton, this class of molecular material corresponds to molecular aggregates wherein the metal centers are held together by metal-metal bonding.[128] Interestingly, those containing metal centers from group V and VI exhibits low oxidation states that contrast with high oxidation states of metal centers within POM framework. This is the way to elaborate rich mixed-valence molecular materials in which oxidation states can vary from +VI to nearly *zero*. In context, the Mo-S type clusters

appear very attractive since they metal-sulfide analogue, such as MoS_2 are known to behave as efficient HER electrocatalysts.[129,130] Furthermore, it has been also shown that Mo-S cluster derivatives exhibits themselves intrinsic HER electrocatalytic activity. For instance, $[Mo_3S_{13}]^{2-}$ anion and derivatives built on the $\{Mo_3S_7\}$ core have been used as model to mimic the HER functioning of the MoS_2-based catalysts.[131] Beside, another cluster-type based on the $\{Mo_3S_4\}$ core has revealed interesting HER activity.[132] This cationic $\{Mo_3S_4\}^{4+}$ unit can be easily functionalized by various ligands, making the resulting coordination complexes easily manipulable with regard to the targeted application. One of the most illustrative applications is probably the use of the organometallic complex $[L_3Mo_3S_4]^+$, where L corresponds to the hydrophobic methylcyclopentadyenyl ligand as co-catalyst deposited onto silicon pillared surface. The resulting photoelectrode was shown to function without HER overpotential by using only 10% of the solar intensity ranging within the NIR domain.[133] Actually, several reports showed that cationic aquo thiomolybdic clusters are able to react with basic polyoxotungstate ions, leading to various POM assemblies.[134] In context, hybrid chalco-POM derivatives can be formed from the condensation of the $[Mo_3S_4]^{4+}$ cation onto preformed polyoxotungstates such as $[SiW_{11}O_{39}]^{7-}$ or $[AsW_9O_{33}]^{9-}$ ions.[135,136,137] Furthermore, the $\{Mo_3S_4\}$ unit can be grafted straightforwardly onto the large macrocyclic POM $[H_7P_8W_{48}O_{184}]^{33-}$ leading to $\{P_8W_{48}\}$-supported $\{Mo_3S_4\}$ catalyst (see Figure 6). Solution studies (see Figure 6 c and d) revealed that synergy arises from the direct interplay between both covalently grafted components, i.e. the $\{Mo_3S_4\}$ catalytic unit and the $\{P_8W_{48}\}$ as electron-collecting unit. Furthermore, such a chalco-POM catalyst has been used as a cocat for the preparation of modified silicon photocathodes, showing that the HER synergy is amplified significantly in the heterogeneous electrochemical process.[138]

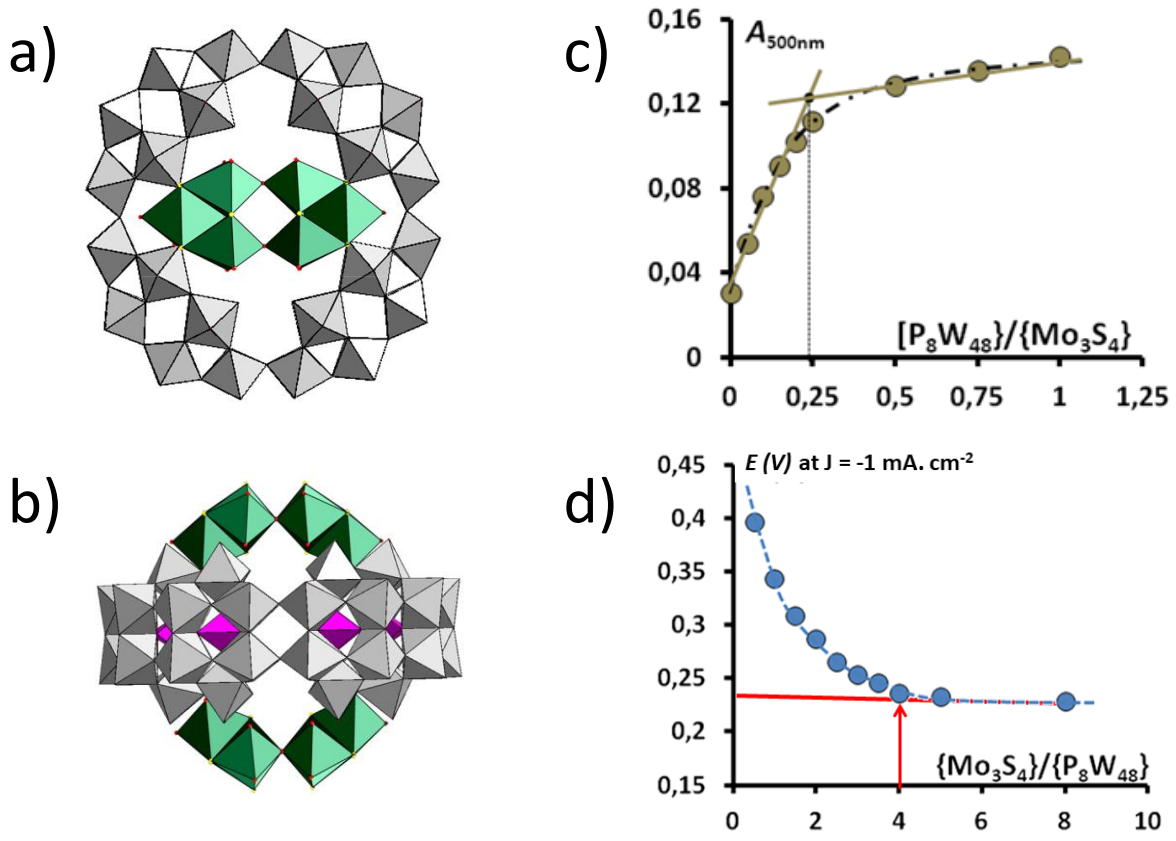

Figure 6. a) top view and b) side view of schematic view of reacting species, i.e., $\{Mo_3S_4\}^{4+}$ electrophilic and $\{P_8W_{48}\}$ nucleophilic units leading to the POM-supported $\{Mo_3S_4\}$ electrocatalysts. c) UV−vis titration of a $\{Mo_3S_4\}$ solution by $\{P_8W_{48}\}$: variation of the absorbance at 500 nm shows a breaking point corresponding to four $\{Mo_3S_4\}$ per $\{P_8W_{48}\}$; d) Electrochemical titration of a $\{P_8W_{48}\}$ solution by a $\{Mo_3S_4\}$ unit showing the HER overpotential measured at a fixed current decrease continuously until a plateau corresponding to the limiting stoichiometry $4\{Mo_3S_4\} + \{P_8W_{48}\}$.

2.6. Superchaotropic properties of POMs with regard to electrocatalysis

POM units employed as electrocatalysts on electrode surfaces are often associated with additional cationic or non-ionic components, such as carbon micro/nanostructures, polymers or MOFs materials. During decades, the attachment of the POMs on surfaces has been mostly viewed through the prism of the electrostatic interactions; however recent observations have highlighted that the situation is often more intricate, and that the role of solvent effects is often predominant for categorie of POMs exhibiting low charge density. In the different context of basic supramolecular chemistry, numerous studies have evidenced that POMs interact strongly with biological moieties such as proteins, peptides or membranes. The first explanations for such a striking phenomenon were given based on the investigations of supramolecular

interactions involving POMs with model non-ionic substrates such as micelles, cyclodextrins or polymers.[139–142] The desolvation process of POMs through supramolecular interactions with these non-ionic units leads to robust supramolecular aggregates in water. The release of the "high energy" hydration shell around the POMs corresponds to a highly favorable thermodynamic process that is featured by an enthalpy gain and an entropy penalty.[44,143,144] In other words, the hydration properties of POMs represent often the main contributor among the conglomerate of weak attractive interactions capable of maintaining supramolecular assemblies.

In context, POMs have be introduced in the historical Hofmeister's series (see Figure 7) that provide an extended classification of anions with regard to their ability to increase (salting-in) or decrease (salting-out) the solubility of proteins.[144] According to this classification, chaotropic or salting-in anions are weakly hydrated, highly polarizable, with low charge density and have the propensity to strongly adsorb on apolar interfaces. Actually, the most popular Keggin-type POMs, but also the giant Mo-blue wheels $\{Mo_{154}\}$ have been ranged within the super-chaotrope categorie.[87] Herein, the term "super-chaotrope" is directly related to the remarkable propensity of these ions to assemble with organic moieties (surfactant, macrocycle or polymer) into highly stable hybrid aggregates deriving from host-guest adducts, micelles or lamellar or globular arrangements.[87,139,140,145–147] It is important to note that the chaotropic character of POMs declines when the global charge density of the POMs increases. For instance, the binding constant between the γ-cyclodextrin and the Keggin anions changes dramatically following the order: $[PW_{12}O_{40}]^{3-} < [SiW_{12}O_{40}]^{4-} < [BW_{12}O_{40}]^{5-} < [H_2W_{12}O_{40}]^{6-}$.[44]

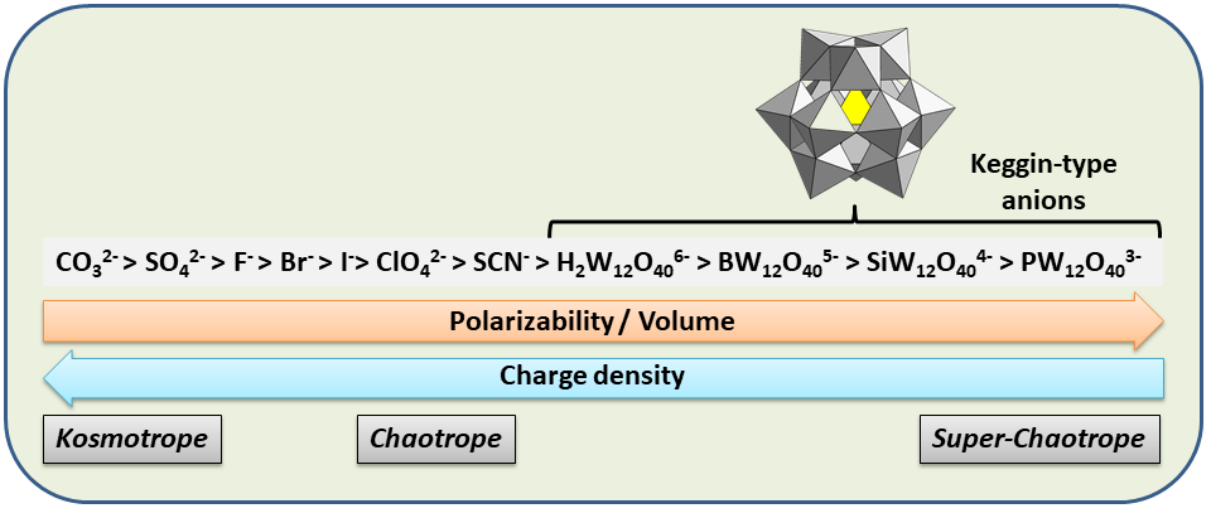

Figure 7. Extended Hofmeister series with specification of the superchaotropic entities.

While often underestimated, recent articles have demonstrated that the mastering of the chaotropic properties of POMs has led to innovative approaches for stabilizing POMs toward hydrolytic processes,[141] or for designing hierarchical multi-component architectures,[142,147,148] such as hybrid open frameworks, host-guest assemblies,[44,45,87] or stimuli responsive soft matter systems. So far, this chaotropic effect has not yet considered as the assembly driving force for designing non-conventional electrodes, while most of POMs employed for modifying (photo)electrodes belong to the super-chaotrope categorie. We think that the propensity of POMs to self-assemble with carbon additives or to be trapped into porous matrices (e.g. MOF) should be reconsidered under the prism of their chaotropic behavior.

3. Immobilization of POMs and Derivatives on (Photo)Electrode Surfaces

3.1. Attachment procedures.

It is worth recalling that the attachment of an electrocatalyst to an electrode surface is essentially motivated in order to take advantage of its intrinsic electrocatalytic properties observed in solution. The transposition from a homogeneous to a supported electrocatalytic reaction using an immobilized catalyst provides numerous benefits especially when synthetic and sensing applications are targeted, such as the use of ultra-small amount of catalyst, the recyclability of the catalyst and the facile separation of electrogenerated product(s) (and therefore easy purification). The two first aspects are particularly relevant when costly or high added value catalysts elaborated in several steps are involved. Besides, the overall efficiency of the electrocatalytic process is dependent on i) the rate of the reaction arising from the electrocatalyst-incorporating assembly (monolayer, multilayered or polymer film, or micro/nanostructured material), ii) the permeation of the substrate and the electrogenerated product(s) through the film, and iii) the transport of electrons across the film from the bulk electrolytic solution to the electrode surface.[149] Therefore, interplay between POM assembly and the support must fulfill some prerequisites to produce catalytically active and efficient POM-modified (photo)electrodes.[150] The support must be preferably porous and permeable to allow the facile transport of species through the film, while a strong affinity not only with POM but also with the surface of the bulk electrode is also required to retain durably and strongly the electrocatalyst within the active film. At last, even though POMs are usually multi-redox centers able to promote fast electron exchanges, the presence of electronically conducting matrice may be beneficial for highly enhancing the electron conduction through the film from the bulk electrode to the POM redox active sites.[149] Based on such considerations, the immobilization strategies of POMs reported since the mid-2010s fall into three broad categories: i) covalent or electrostatic attachment to monomolecular films or 3D metal-organic

frameworks (MOFs), ii) chemisorption on metal (e.g. Ni foam and metal nanocrystals) or carbon (graphene, graphene oxide and carbon nanotubes) micro/nanostructures and iii) electrostatic entrapment within charged polymer films (see Figure 8).

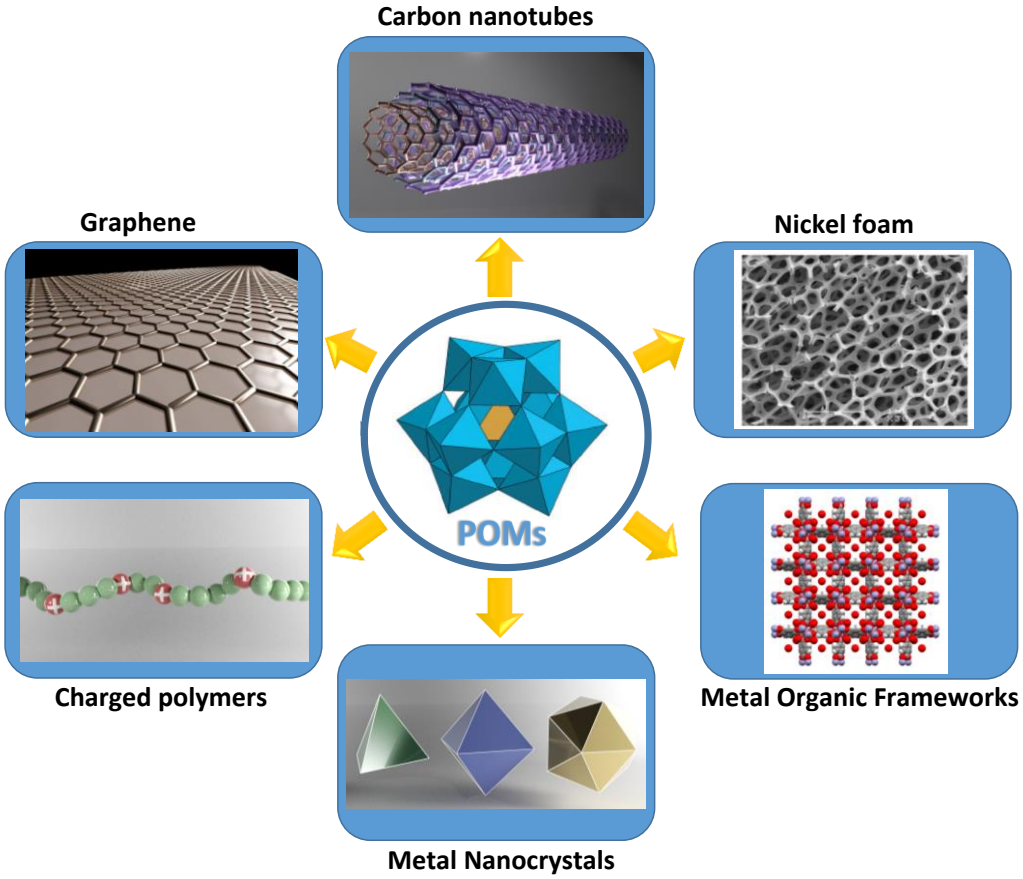

Figure 8. Immobilization strategies of POMs on (photo)electrode surfaces.

In most cases, the POM is first attached to the immobilization support and the resulting assembly is then dispersed in an appropriate solvent before being deposited by drop-casting or spin-coating on the (photo)electrode surface. Carbon black is sometimes added to the dispersion to improve the electron conduction of the assembly and/or an additional Nafion® layer acting as an electrostatic barrier is deposited on the POM-modified electrode. In other cases (incorporation of POM in an electropolymerized film, grafting to a monolayer covalently bound to the electrode surface or to a metal foam), the electrocatalyst is directly immobilized in a single step on the electrode surface. The thickness of the catalytic layer deposited on the electrode is usually optimized in order to reach the maximum electrocatalytic efficiency.

Once prepared the POM-modified electrode, the (photo)electrocatalytic reaction is then conducted in a solvent in which the immobilized POM is totally insoluble to avoid its detachment from the electrode. The different aforementioned immobilization procedures will be discussed in more details in the following sections.

3.2. Conducting vs Semiconducting Electrodes.

The nature of the electrode used to immobilize an electrocatalyst, such as POM, may impact positively or negatively the electron-transfer kinetics of the overall electrocatalytic process. Usually, when a conventional conducting electrode (usually glassy carbon or graphite) is used, the impact is rather weak provided that its conducting properties are not electrochemically degraded, i.e. the applied potentials are within the stability window of the electrode, or it is not poisoned by chemical species (namely, substrates, electrogenerated products and electrolyte components). Under such conditions, the electrode acts as a catalytically inert material delivering (or accepting) fastly electrons to (from) the immobilized electrocatalyst. Furthermore, its conducting properties are not affected by light. This situation totally contrasts with that encountered for a photoactive semiconducting electrode for which the electrochemical process can be activated by photogenerated charge carriers (electrons or holes). Consequently, the use of semiconducting electrodes instead of non-photoactive ones could provide a real benefit in the field of the electrochemical catalysis in terms of energy gain. The basic concept of the light-activated electrochemical catalysis (or *photoelectrocatalysis*) is that when a semiconductor (SC) surface is irradiated with light of adequate energy $h\nu$ higher than the bandgap energy of SC (E_g), an electron/hole pair (e^-/h^+) is generated in SC resulting in a delocalized electron in the conduction band (higher unoccupied energy level, CB) and a delocalized hole in the valence band (lower occupied energy level, VB) (see Figure 9).[151–153] After charge separation, the photogenerated charge carriers (i.e. electrons or holes for *p*- or *n*-type SC, respectively) are swept to the surface, transferred to the immobilized electrocatalyst units in close proximity, then to the substrate after hopping between the adjacent catalytic sites.

It is worth stressing that the photoeffects are generally observed at *n*-type and *p*-type SC electrodes for redox processes located at potentials positive and negative of SC's E_f, respectively. In other words, the oxidation of bound reduced species by photogenerated surface holes or the reduction of bound oxidized species by photogenerated surface electrons will be primarily responsible for the photocurrents observed at illuminated modified *n*- (called *photoanode*) or *p*-type (*photocathode*) SC electrodes, respectively.[153,154] As a result of the photogenerated minority charge carrier-induced activation of the redox process, the electrocatalytic reaction at illuminated modified photoanode or photocathode is often observed at less positive or negative potentials, respectively, compared to the case of similarly modified conducting electrodes. This beneficial potential shift called *photovoltage* is significantly dependent on numerous factors, such as the SC bandgap, the CB/VB edge positions, the dopant concentration and the illumination level.

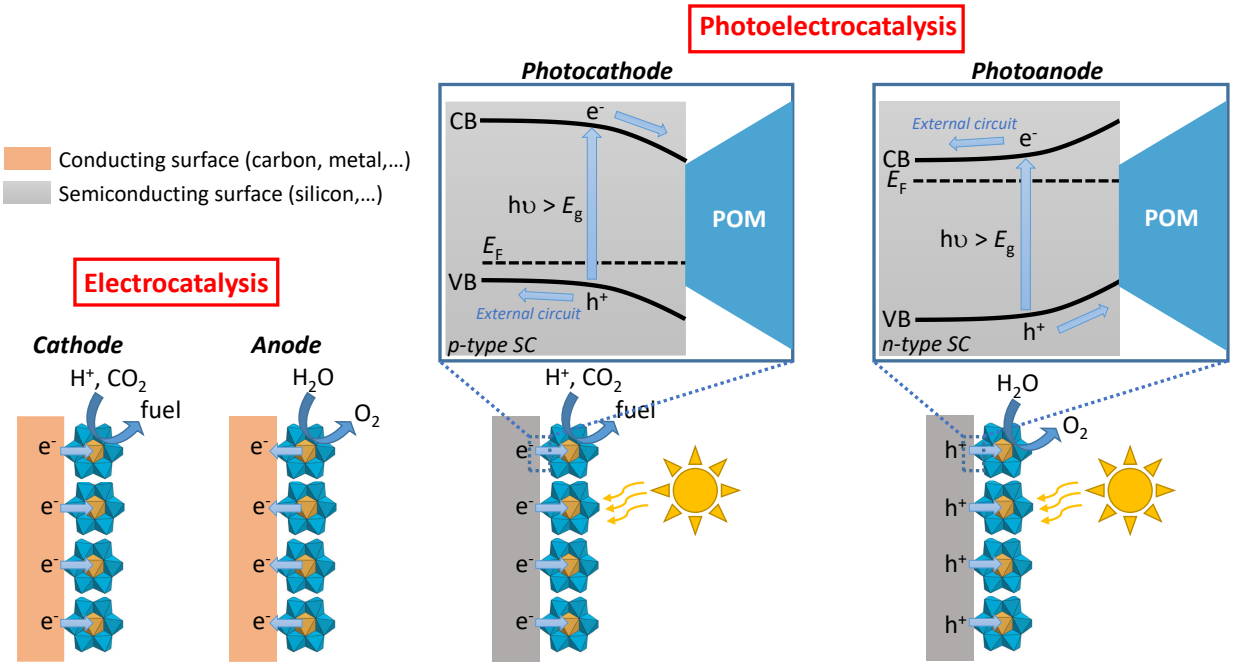

Figure 9. Simplified representations of the (photo)electrocatalytic reactions at POM-modified conducting and semiconducting electrodes, illustrated with reactions of high interest: hydrogen evolution (HER), CO_2 reduction (CDRR) and oxygen evolution (OER) reactions. The insets correspond to the photoinduced charge transfer processes at illuminated POM-modified *p*-type photocathode (left) and *n*-type photoanode (right). The immobilization support of POM (monolayer, polymer, MOF, metal or carbon micro/nanostructures) is omitted for clarity. *Unlike metals, semiconductors have two types of charge carriers, namely electrons and holes. For a n-type doped semiconductor, the electrons are the majority charge carriers because their concentration is much higher than that of holes and the*

electrochemical potential of the semiconductor, the so-called Fermi level E_F, lies just below the conduction band (CB) edge. For a p-type semiconductor, the holes are the majority charge carriers because their concentration is much higher than that of electrons, and E_F now lies just above the valence band (VB) edge.

Depending on both band edge positions of valence and conduction bands of SCs and E_g, the illuminated photoelectrodes can promote efficiently either electrochemical reduction reactions of interest, such as HER or CDRR, or oxidation reactions, such as OER (see Figure 10).

From a practical point of view, the SC electrodes are illuminated using an artificial light source such as a Xe lamp, which produces a white light that closely mimics natural daylight. Such an artificial light is calibrated *vs* the reference solar spectrum (air mass 1.5 global spectrum referred to as AM1.5 G with an irradiance of 100 mW cm^{-2}) allowing the performance comparison of functionalized photoelectrodes from different research laboratories (Fig. 8b). So, small E_g SCs, such as silicon (E_g = 1.1 eV), absorb a large fraction of the available solar spectrum and consequently will be able to deliver high photocurrent densities. In contrast, large E_g SCs, such as metal oxide TiO_2 (E_g = 3.2 eV), only absorb a small fraction of solar spectrum which leads to small photocurrent densities.

Finally, in the context of a photoactive electrode, the optical absorption of the deposited catalytic layer (i.e. POM and the immobilization support) may be a critical issue for effective photoelectrocatalysis because it may lead to the decrease in the photocurrent densities with respect to the bare photoelectrode. Consequently, the thickness, composition and morphology of the deposit must be optimized to enable high electrocatalytic efficiency (as for the case of non-photoactive conducting electrodes) while not substantially reducing light intensity transmitted to the SC.

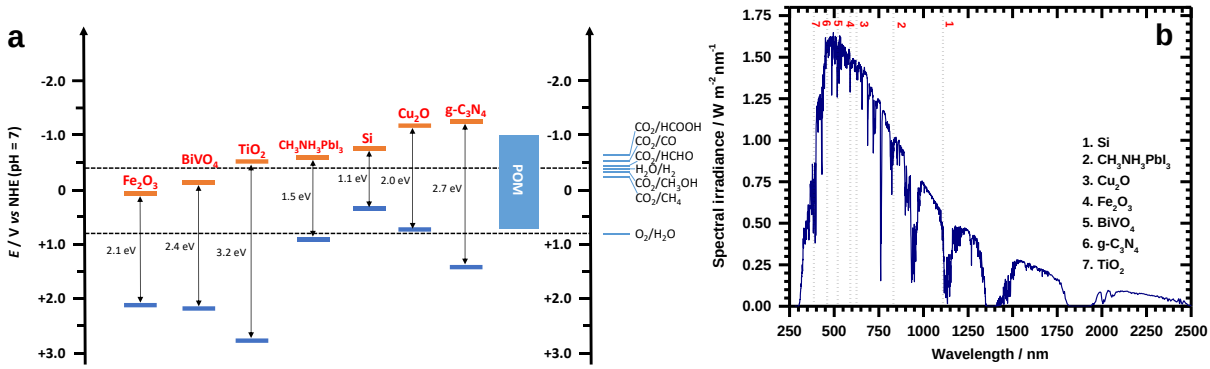

Figure 10. a) Positions of conduction (orange rectangles) and valence (blue rectangles) bands for selected semiconductors at pH 7, with their respective energy bandgap, used as photoelectrodes for immobilizing POMs as electrocatalysts. The electroactivity window of POMs and the potentials of several CO_2 reduction and water redox couples are also depicted at pH 7 *vs* Normal Hydrogen Electrode (NHE). b) AM1.5 G solar spectrum (ASTM G173-03 reference spectrum, data from National Renewable Energy Laboratory) with positions of energy bandgap of various semiconductors of interest.

4. POMs-Functionalized Conducting Electrodes

4.1. Electrostatically entrapped POMs

Owing to the anionic nature of POMs, their incorporation into positively charged polymer films or their intercalation in layer-by-layer (LBL) assemblies with metal ion complexes is a straightforward approach to strongly and durably immobilize such entities on electrode surfaces. Recent relevant examples have demonstrated that POMs such as the Dawson $[P_2W_{18}O_{62}]^{6-}$, or 3d-metal containing $[Co_9(H_2O)_6(OH)_3(HPO_4)_2(PW_9O_{34})_3]^{16-}$ or Ni^{II}-crown-type $[Ni_4(P_8W_{48}O_{184})(WO_2)]^{28-}$ entrapped in polypyrrole films or microparticles were electrocatalytically active for the H_2O_2 reduction,[155] OER[156] or bromate reduction,[157] respectively. Nevertheless, it is clear that the electrostatic entrapment of POMs into electronically conducting polymer (ECP) films is nowadays much less explored for designing catalytically active POM-modified electrodes while this immobilization approach pioneered by the Keita, Nadjo and Bidan's groups was very popular in the 80s-90s.[158–162] As a matter of fact, a plausible reason to explain such a trend is that the electrocatalytic process occurs usually in a potential window wherein the polymer film is converted to an electronically insulating form by either electrochemical reduction (for reduction processes such as HER) or overoxidation (for oxidation processes such as OER). Under such conditions, the polymer matrix does not participate (and even hinder) to the charge transport and only the electron hopping between the embedded POM sites shall be considered as the main charge transport mechanism. So, it is anticipated that the overall reaction kinetics of the electrocatalytic process should be slower than that for the case where the polymer would retain its conductive properties. This hypothesis is somewhat inconsistent with literature data on redox polymer-modified electrodes which have demonstrated that charge propagated through a redox polymer film by electron hopping was not necessarily limiting for efficient electrocatalysis.[163] Besides conductivity issue, the ECPs show often a low permeability, a high hydrophobicity and a limited stability over

electrochemical cycling which may explain the lack of recent interest in these materials as immobilization matrices of POMs.

Based on the aforementioned considerations, charged polyelectrolytes, surfactants and LBL assemblies have merged as promising alternatives to immobilize more durably POMs and yield catalytically active modified electrodes. First, the encapsulation of the weakley-type $[Cu_4(H_2O)_2(PW_9O_{34})_2]^{10-}$ species in a cationic surfactant, such as dimethyldioctadecylammonium (DODA), has enabled access to honeycomb structure microporous and electroactive films exhibiting an electrocatalytic activity towards the reduction of bromate BrO_3^-.[164] Although this encapsulation approach offers some benefits, in terms of simplicity and controlled morphology, it is anticipated that the retention of POMs by the cationic surfactant is weaker than that expected by a cationic polymer network. Therefore, several charged polyelectrolytes have been selected to fabricate robust and electrocatalytically active POM-functionalized electrodes. Accordingly, the ruthenium-containing POM molecular catalyst $[\{Ru_4O_4(OH)_2(H_2O)_4\}(\gamma\text{-}SiW_{10}O_{36})_2]^{10-}$ immobilized in a poly(diallyldimethylammonium) film showed a considerable reactivity for the electrocatalytic oxidation of ethanol and methanol with a Faradaic efficiency exceeding 94%.[165] In another significant example, the Weakley-type anion $[Co_4(H_2O)_2(PW_9O_{34})_2]^{10-}$ (see Figure 5D-a) immobilized in an ionic polymer, poly(vinyl butyl imidazolium), performed remarkable electrocatalytic OER under alkaline conditions with a very low overpotential of 0.20 V and a very high current density of 250 mA cm^{-2} (at 1.75 V *vs* Reversible Hydrogen Electrode RHE).[166] Very recently, Streb and co-workers have developed a POM-derived composite OER electrode by electrostatically attaching this Weakley-type anion $[Co_4(H_2O)_2(PW_9O_{34})_2]^{10-}$ on a cationic polymer polyethylenimine shell decorating commercial TiO_2 nanoparticles used as a low-cost, eco-friendly and nanoscale support.[167] The resulting composite showed promising electrocatalytic OER performance in 0.1 M aqueous KOH solution over prolonged periods (>10

h). The integrity of POM under such electrochemical conditions is however questionable. Indeed, Finke and co-workers have shown that this mixed metal Co-W Weakley-type POM $[Co_4(H_2O)_2(PW_9O_{34})_2]^{10-}$ was gradually degraded to catalytically superior CoO_x species under controlled-potential OER electrolytic tests in phosphate buffer (pH 8).[168] Moreover, several studies have demonstrated the hydrolytic decomposition of heteropolyoxotungstates when both alkaline and oxidative electrochemical conditions were fulfilled.[169]

Table 1. POM-LBL Assemblies for Electrocatalysis

Anionic POM	Cationic Layer	Bilayer Number	Electrocatalytic Reaction	Ref
$[SiW_{10}O_{36}(PhPO)_2]^{4-}$	Ru(II) metallodendrimer ($Ru_4C_{125}N_{24}H_{92}P_8F_{48}$)	1-8	NO_2^- reduction	170
$[Cu_{20}Cl(OH)_{24}(H_2O)_{12}(P_8W_{48}O_{184})]^{25-}$	Ru(II) metallodendrimer ($Ru_4C_{125}N_{24}H_{92}P_8F_{48}$)	-	IO_3^- reduction	171
Crown-type POMs: $[Fe_{16}(P_8W_{48}O_{184})(OH)_{28}(H_2O)_4]^{20-}$, $\{Ni_3[Ni_4(H_2O)_{16}(P_8W_{48}O_{184})(WO_2)(H_2O)_2]\}^{22-}$, $\{Co_2[Co_4(H_2O)_{16}(P_8W_{48}O_{184})]\}^{28-}$	Ru(II) metallodendrimer ($Ru_4C_{125}N_{24}H_{92}P_8F_{48}$)	1-8	NO_2^- reduction	172
$[SiW_{12}O_{40}]^{4-}$	$[Mn(III)TRP]^{5+}$, $[Zn(II)TRP]^{4+}$ or $[Ni(II)TRP]^{4+}$	2-10	NO_2^- reduction	173
$[Co_4(H_2O)_2(PW_9O_{34})_2]^{10-}$	Dye methyl green	1-15	NO_2^- or IO_3^- reduction	174
$[Fe^{III}(P_2W_{17}O_{61})]^{8-}$, $[Cu^{II}(P_2W_{17}O_{61})]^{8-}$, $[P_2W_{18}O_{62}]^{6-}$	Cu-phthalocyanine	1-4	Phosphate reduction	175
$[Fe^{III}(P_2W_{17}O_{61})]^{8-}$, $[Cu^{II}(P_2W_{17}O_{61})]^{8-}$, $[Ni^{II}(P_2W_{17}O_{61})]^{8-}$	Poly(diallyldimethylammonium) + Ag nanoparticles	1-4	NO_2^- or NO_3^- reduction	176
Crown-type POMs: $[Cu_{20}Cl(OH)_{24}(H_2O)_{12}(P_8W_{48}O_{184})]^{25-}$, $[Ni_4(P_8W_{48}O_{148})(WO_2)]^{28-}$	Poly(diallyldimethylammonium) + Ag nanoparticles	1-4	NO_2^- or NO_3^- reduction	177
$[Ni_4(P_8W_{48}O_{148})(WO_2)]^{28-}$	Ag nanoparticles	1-4	ClO_3^- reduction	178
$[PW_9V_3O_{40}]^{3-}$	Poly(ethyleneimine) + Pt@Pd nanoparticles	1-6	H_2O_2 reduction	179
$[Pd^{II}(PW_{11}O_{39})]^{5-}$	Amino-terminated poly (amido-amine) dendrimer	1-5	Methanol oxidation	180

Abbreviations: Ph = Phenyl. TRP = μ-{meso-5,10,15,20-tetra (pyridyl) porphyrin} tetrakis {bis(bipyridine) chloride ruthenium(II)}$(PF_6)_4$.

The second immobilization route using electrostatic process, namely the LBL assembly, constitutes a simple and reliable method to build well-ordered redox-active architectures with excellent control on the film thickness and the surface coverage of the entrapped functionality.[181] So, Keggin-, Dawson- and crown-type POMs and their transition metal ion-substituted derivatives have been assembled with various cationic components, such as redox-

active Ru(II) metallodendrimers,metal-complexed porphyrins, or non-electroactive polymer layers, to produce functional electrodes which were active for the electrocatalytic reduction of some oxyanionic species (e.g. nitrite), hydrogen peroxide reduction or oxidation of methanol (see Table 1).[170–180] Compared with POMs-incorporating ECP films, such assemblies offer some benefits such as an enhanced permeability, a better robustness over electrochemical cycling and a better resistance against some interferents. Interestingly, the assembly with redox-active cationic complexes enabled to extend the electroactivity window of the functional electrodes.[170–173,175] Furthermore, additional incorporation of metal nanoparticles (e.g. Ag), notated NPs hereafter, was found to be also beneficial for increasing the electronic conductivity of such assemblies.[176–179]

4.2. POMs/Metal Organic Frameworks (MOFs) Assemblies

4.2.1. Definition

POM@MOF. The non-covalent immobilization of POMs into Metal-Organic Frameworks (MOFs), a class of porous crystalline solids built from the reticulation of metal centers by organic ligands, represents an appealing approach to develop heterogeneous electrocatalytically active systems named POM@MOF (see Figure 11). Unlike the other porous materials (zeolites, activated carbon, mesoporous silica), MOFs are hybrid organic–inorganic hosting matrices that exhibit a wide structural diversity, wide pore sizes, flexibility, high porosity and extremely large surface area (up to 10 000 m^2/g).[182] The intrinsic structural features of MOFs make them interesting for encapsulating molecular catalysts, such as POMs. Within the MOFs, the entrapped homogeneous POM-based catalysts can benefit of the improved stability and easier recyclability and also a better diffusion of reactants to the POM units. Some recent reviews have been published on the synthetic strategies, the characterization methods and the catalytic properties of POM@MOFs.[183–185]

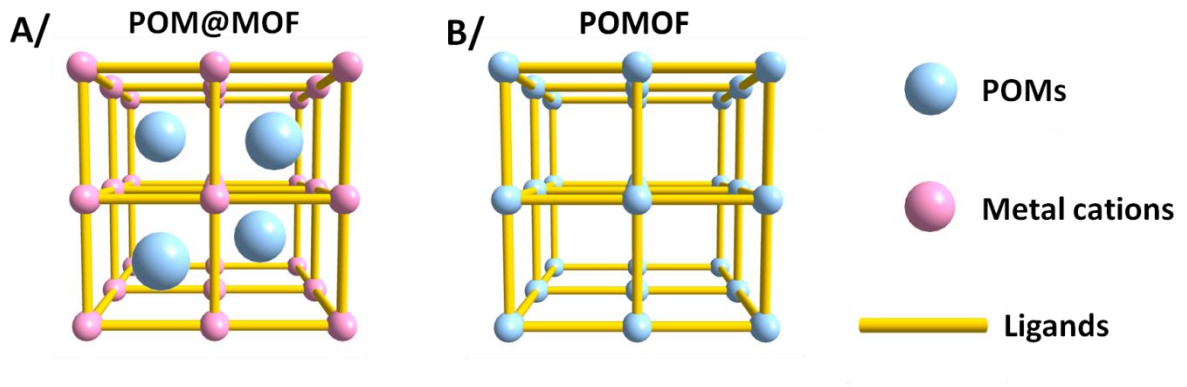

Figure 11. A) Illustration of a POM@MOF material resulting from immobilization of a POM within a MOF structure. B) Illustration of a POMOF structure that results from the assembly of POMs and organic ligands.

POMOF. These compounds represent a class of coordination polymers that are built from the assembly of transition metals, POMs and organic ligands. Such compounds are generally prepared by hydro/solvothermal treatments. The POMOF arrangement can be broadly subdivided into two families. The first one corresponds to the structures based on the ε-Keggin-type POMs stabilized by capping metallic cations (mostly Zn^{2+}) that are generally connected by (poly)carboxylate ligands. The resulting anionic frameworks generally exhibit voids in which organic cations are located. The second family of POMOF is built from N-donor ligands recognized to bind soft metal ions, such as Ag^{I}, $Cu^{I/II}$, Co^{II} or Ni^{II}. In contrast to the first POMOF family, this second class exhibits usually dense structures.

4.2.2. Non-covalently immobilized POMs in MOFs (POM@MOF)

As electrocatalysts, the POM@MOF compounds have been used mostly for water oxidation. Nevertheless, a recent report highlights their ability to reduce also CO_2 into CO. The activity of POM@MOF can be also exploited to perform the electrocatalytic reduction of bromate ions and H_2O_2 in aqueous solution. Table 2 summarizes the different reports dealing with the electrocatalytic activities of these POM@MOF based systems.

Table 2. POM@MOFs based systems for electrocatalysis

POM	MOFs	Electrocatalytic Reaction	Overpotential (mV)	Tafel slope ($mV.dec^{-1}$)	Ref
$[Co_4(H_2O)_2(PW_9O_{34})_2]^{10-}$	MIL-101 (Cr^{3+})	Water oxidation (pH = 8)	493 (1 mA cm^{-2})	69	186

$[Co_4(H_2O)_2(PW_9O_{34})_2]^{10-}$	MIL-100 (Fe^{3+})	Water oxidation (pH = 8)	N/A	N/A	187
$[Co(H_2O)(CoW_{11}O_{39})]^{7-}$	MIL-100 (Fe^{3+})	Water oxidation (pH = 8)	N/A	N/A	187
$[CoW_{12}O_{40}]^{6-}$	ZIF-8 (Zn^{II})	Water oxidation (pH = 7)	800 mV	783	188
$[Co_3O_3(H_2O)_3(SiW_9O_{34})]^{10-}$	ZIF-8 (Zn^{2+})	Water oxidation (pH = 13)	2730 (10 mA cm^{-2})	69.4	189
$[Co_3O_3(H_2O)_3(SiW_9O_{34})]^{10-}$	ZIF-67 (Co^{2+})	Water oxidation (pH = 13)	470 (10 mA cm^{-2})	113.6	189
$[SiW_{12}O_{40}]^{4-}$	HKUST-1 (Cu^{2+})	Water oxidation (pH = 14)	340	73	190
$[SiW_{12}O_{40}]^{4-}$	ZIF-8 (Zn^{2+}) + [Fe(salen)(OH)] as co-catalyst	Water oxidation (pH = 13)	516 (1 mA cm^{-2})	344	191
$[Co(H_2O)(CoW_{11}O_{39})]^{7-}$	PCN-222(Co)	CO_2 reduction (CO production)	N/A	216	192
$[PW_{12}O_{40}]^{3-}$	HKUST-1 (Cu^{2+})	BrO_3^- reduction (pH = 2)	N/A	N/A	193
$[PMo_{12}O_{40}]^{3-}$	HKUST-1 (Cu^{2+})	BrO_3^- reduction (pH = 2)	N/A	N/A	193
$[PMo_{12}O_{40}]^{3-}$	HKUST-1 (Cu^{2+})	H_2O_2 reduction (pH = 7.4)	N/A	N/A	194

Abbreviations: MIL: Matériaux de l'Institut Lavoisier; ZIF: Zeolitic Imidazolate Frameworks; HKUST: Hong Kong University of Science and Technology; PCN: Porous Coordination Network; N/A= Not available

In 2010, the group of Hill discovered that the noble metal-free catalyst $[Co_4(H_2O)_2(PW_9O_{34})_2]^{10-}$ was an efficient molecular catalyst for water oxidation.[13] The encapsulation of this POM required MOF exhibiting large cavities, such as the mesoporous MOFs, namely the MIL-100 or the MIL-101. This Weakley-type POM $[Co_4(H_2O)_2(PW_9O_{34})_2]^{10-}$ was immobilized on Cr^{3+}-based MIL-101 by an ion exchange method involving the F^- anions. Such a process allows the introduction of about 7 POMs per POM cavity. The electrocatalytic performance of the resulting material has been investigated in borate buffer (pH = 8). It was showed that the $[Co_4(H_2O)_2(PW_9O_{34})_2]^{10-}$@MIL-101 material exhibited a moderate overpotential (493 mV for a current density of 1 mA cm^{-2}) and the calculated Tafel slope was about 69 mV dec^{-1}.[186] Long-term electrolysis over ~3 hours at 1.3 V *vs* NHE yielded a slight decrease of the current density (from 1.6 to 1.5 mA cm^{-2}), which was thought to be caused by the release of the POM. The POM leaching during electrocatalysis is probably favored by the large apertures of the MIL-101 large window size (17 Å) that are larger

than the POM size (~10 Å). Based on this observation, the group of Kögerler has employed a mesoporous Fe^{3+}-based MIL-100, a MOF with pore windows of 5.5 Å and 8.6 Å, as host matrix for the encapsulation of POM-based water oxidation catalysts.[187] The encapsulation of $[Co_4(H_2O)_2(PW_9O_{34})_2]^{10-}$ and another cobalt-based Keggin-type POM $[Co(H_2O)(CoW_{11}O_{39})]^{7-}$, recognized for its ability as water oxidation catalyst has been achieved through one-pot hydrothermal preparation of the MOF. At pH = 8, the two POM@MOF composites display lower onset potential and a higher current density than those of the native POM. Nevertheless, no significant difference in the electrocatalytic activity was observed between these two hybrid materials.

In 2018, the group of Das reported the use of the Keggin-type anion $[CoW_{12}O_{40}]^{6-}$ as acidic form encapsulated within the archetypal ZIF-8, a MOF built from zinc centers and imidazolate ligands, with the perspectives of developing efficient and robust electrocatalyst for water oxidation.[188] This successful synthetic approach has been also used for encapsulation of other Keggin-type POMs in various ZIF hosts (Zeolite Imidazolate Framework) (see Figure 12A). The electrochemical performance of this composite material has been studied using a $\{H_6[CoW_{12}O_{40}]\}$@ZIF-8 modified electrode prepared by dropping a mixture of $\{H_6[CoW_{12}O_{40}]\}$@ZIF-8 with black carbon and Nafion® on a glassy carbon electrode. In acid condition (pH = 1.9), the authors observed the oxidation of the Co center ($Co^{II} \rightarrow Co^{III}$) of the encapsulated $[CoW_{12}O_{40}]^{6-}$ ion, occurring at a lower potential than that usually found for the free POM (shift of about -120 mV). Moreover, the authors found that the oxidation process from Co^{III} to Co^{IV} is also observable in the POM@MOF assembly. Das et al. explain this unsusual redox event by a partial electronic redistribution of the POM unit in $\{H_6[CoW_{12}O_{40}]\}$@ZIF-8 which results from electronic density donation from the MOF to the low lying W-centered LUMOs of the POM. At neutral pH, a large current onset over the potential range of Co^{II} and Co^{III} oxidations is observed and attributed to the electrocatalytic

water oxidation. In such conditions, the {$H_6[CoW_{12}O_{40}]$}@ZIF-8 exhibits a turnover frequency of 10.8 mol O_2 (mol Co)$^{-1}$ s^{-1} which remains highly stable over 1,000 cycles. Furthermore, no formation and contribution of CoO_x along the water oxidation electrocatalysis was detected. However, the measured overpotential remains quite high (~800 mV *vs* RHE) at a current density of 1 mA cm^{-2}, and the Tafel slope is also high (783 mV dec^{-1}) due to the inherent resistive nature of ZIF-8 that induces high ohmic resistance. All these characteristics have been reported for POM-MOF materials with a low POM loading (25% of cavities occupied by POMs). Larger loading, up to one POM per cavity, does not improve the electrochemical performance. Besides, The cavity of ZIF-8, that exhibits similar size to that of the Keggin-type POM, behaves as a protecting matrix which prevents any hydrolytic decomposition of the POMs. For instance, mechanical mixtures of POM and ZIF-8 exhibit weak electrocatalytic efficiencies due to the degradation of the POM after only few cycles. Such investigations upon water oxidation catalysis have been also extended to other Keggin-type POMs encapsulated within ZIF-8, leading to constrated catalytic performances. For instance, the encapsulated $[Co_3O_3(H_2O)_3(SiW_9O_{34})]^{10-}$ ion (see Figure 5A-c for the structural arrangement) in ZIF-8 with low loading (about 6% of ZIF cage are occupied by the POM), shows very weak activity in basic conditions (0.1M KOH), featured by high overpotential and low current density.[189] In contrast, the same Keggin-type POM entrapped within ZIF-67, a porous host with similar structure to that of ZIF-8 where Zn^{2+} coordinated nodes have been substituted for Co^{2+}, exhibits excellent electrocatalytic activity (see Figure 12A).[189] This POM@MOF material exhibits a lower overpotential (470 mV *vs* RHE for a current density of 10 mA cm^{-2}), decreasing significantly the overpotential of the hosting ZIF-67 matrix (580 mV *vs* RHE for a current density of 10 mA cm^{-2}) and Tafel slope of about 113.6 mV dec^{-1}. The OER performance of $[Co_3O_3(H_2O)_3(SiW_9O_{34})]^{10-}$ @ZIF-67 is also enhanced in comparison with the respective activities of its individual components (see Figure 12C). Therefore, such a synergistic effect

was believed to result from *i*) a better electron transfer from the MOF to the electron-poor POMs and *ii*) undercoordinated Co nodes in the ZIF-67 frameworks due to the presence of POMs which induce defects. The electrocatalyst system $[Co_3O_3(H_2O)_3(SiW_9O_{34})]^{10-}$@ZIF-67 exhibited high electrochemical stability since no decrease of the OER activity has been observed for at least 12 hours of electrolysis.

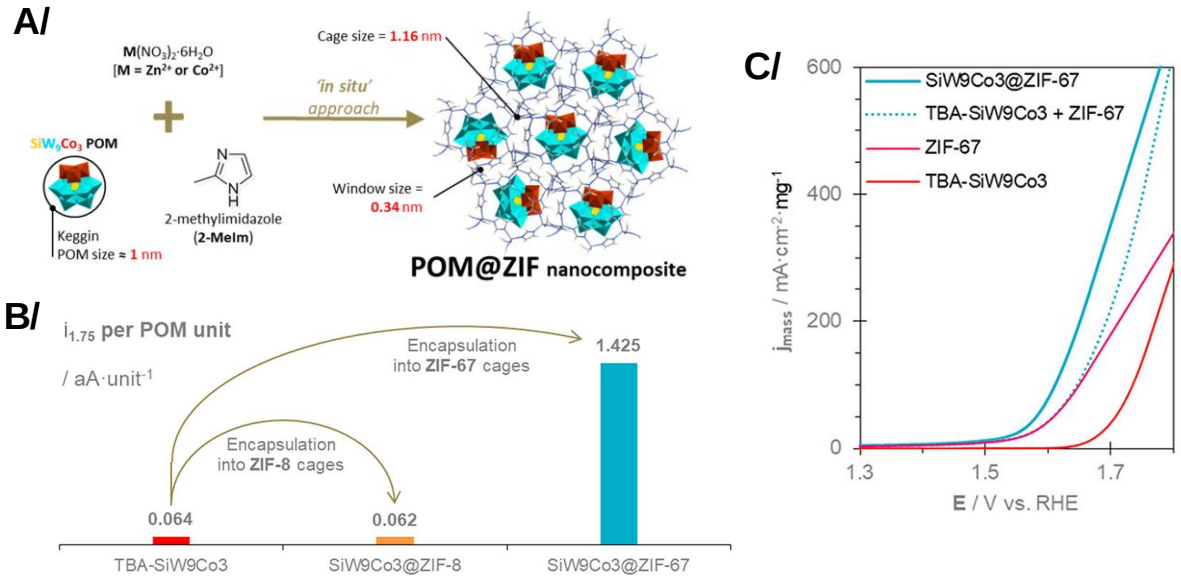

Figure 12. A/ Preparation of POM@ZIF nanocomposites by *in situ* one-pot approach. B/ SiW_9Co_3 unit activity estimations for "bulk" POMs $(TBA)_6H_4[SiW_9Co_3(H_2O)_3O_{37}]$ and ZIF-encapsulated POMs in the different nanocomposites—expressed as attoamperes, aA, per POM cluster. C/ Mass-normalized LSV polarization curves of OER for $[SiW_9Co_3(H_2O)_3O_{37}]^{10-}$@ZIF-67 compared with the sum (dash lines) of the respective individual components. Adapted with permission from ref 189. Copyright 2020 American Chemical Society.

Zhou *et al.* have recently prepared a POM@MOF composite prepared from silicotungstic acid $H_4[SiW_{12}O_{40}]$, Cu^{2+} and trimesic acid in water/ethanol mixture.[190] The authors proposed that the resulting material $\{Cu_2[SiW_{12}O_{40}]\}$@HKUST-1 corresponded to the Keggin anion $[SiW_{12}O_{40}]^{4-}$ encapsulated within HKUST-1 host where two copper ions per POM units neutralizes the negative charge of the polyanion. However, no convincing data supported this hypothesis. Anyway, the electrocatalytic activity for OER has been studied in 1.0 M KOH and the measured overpotentials and the Tafel slopes revealed the $\{Cu_2[SiW_{12}O_{40}]\}$@HKUST-1

(340 mV; 73 mV.dec^{-1}) exhibited better OER activity than the archetypal MOF, HKUST-1 (420 mV; 84 mV dec^{-1}). Nevertheless, such a catalyst had excellent long-term stability.

Besides initiating the development of heterogeneous pure POM@MOF OER electrocatalysts, the co-encapsulation of molecular transition metal complexes and POMs can improve the OER efficiency as shown by the co-encapsulation of the inorganic coordination complex $[Fe^{III}(salen)(H_2O)]^+$ and $[SiW_{12}O_{40}]^{4-}$ in the ZIF-8 pore system.[191] This study evidenced three important benefits of the co-encapsulation of the POM: *i*) faster formation of the hybrid composite, *ii*) higher loading of cationic Fe-based complex, and *iii*) lowering of overpotential for electrochemical OER by more than 150 mV in comparison with the ZIF-8 containing exclusively the $[Fe^{III}(salen)(H_2O)]^+$ complex. It was proposed that the introduction of the POMs can facilitate electrical charge conduction in the MOF. Importantly, the electrocatalytic studies had been performed in 1M KOH, while $[SiW_{12}O_{40}]^{4-}$ ion decomposed at pH values higher than 4, thus questioning on the true nature of the POMs in such conditions.

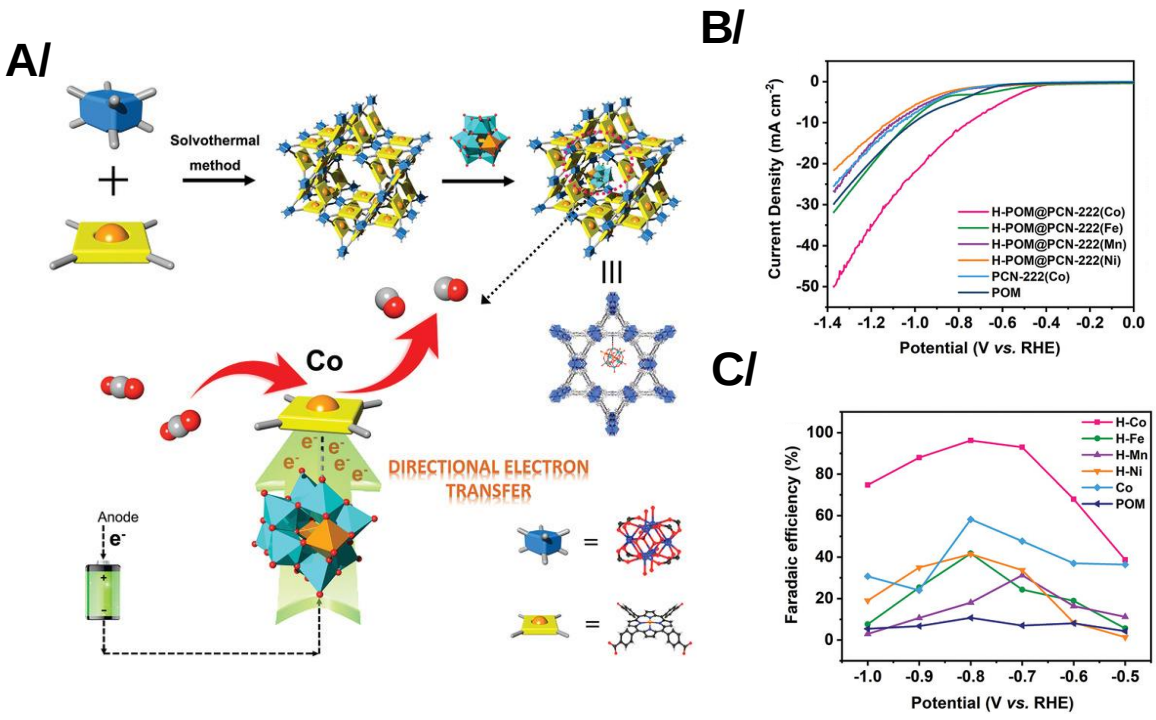

Figure 13. A) Illustration of the synthetic process and the structure of $[Co(H_2O)(CoW_{11}O_{39})]^{7-}$@PCN-222(Co). In this composite, the Keggin-type POM forms an electron-transfer channel from the electrode to active Co center of the metalloporpherin, and consequently favors the multi-electron-transfer process

to enrich the electron density of the active Co center wherein the CO_2-to-CO reduction occurs. B) Electrocatalytic CO_2RR performance of $[Co(H_2O)(CoW_{11}O_{39})]^{7-}$@PCN-222(M) in which the nature of the three 3d metallic cation of the porphyrin is varied (M = Co^{2+}, Fe^{2+}, Mn^{2+}, Mn^{2+}, Ni^{2+}). C) Evolution of the Faradaic efficiencies for CO formation with different metals and at different potentials. Adapted with permission from ref 195. Copyright 2021 Wiley-VCH.

The PCN-222 (PCN: Porous Coordination Network) corresponds to a robust mesoporous zirconium-porphyrin MOF used to design POM@MOF electrocatalysts for the reduction of CO_2.[195] The insertion of $[Co(H_2O)(CoW_{11}O_{39})]^{7-}$ within the channel of the MOFs has been performed by impregnation (see Figure 13A). The POM loading is strongly influenced by the nature of the metal center of the metalloporphyrin, and the best loading was obtained for the Co-based porphyrin. The electrocatalytic reduction of CO_2 has been studied in 0.5 M $KHCO_3$ solution, revealing that the onset potential for $[Co(H_2O)(CoW_{11}O_{39})]^{7-}$@PCN-222(Co) was reduced by 350 mV. Investigation of the electrochemical properties (onset potential and faradaic efficiency) of the POM@MOF materials revealed the key role of coordinated metal cations at the porphyrins (see Figure 13B and C). This electrocatalytic material gave a high faradaic efficiency of 96.2% for electroreduction of CO_2 into CO with a good stability over 10h of electrolysis. DFT calculations confirm that the directional electron transfer, which accelerates the multi-electron transfer from the electrode to active single-metal site Co, enriches the electron density of the Co center, and ultimately reduces the energy of the rate-determining step of the CO_2RR process.

The electrocatalytic activities of the POM@MOFs compounds have been also exploited for the electrochemical detection of H_2O_2 or bromate.[193,194] The electrocatalytic composite resulting from the combination of Ketjenblack carbon with the NENU-5 material (NENU: Northeast Normal University), an HKUST-1 (HKUST: Hong Kong University of Science and Technology) containing encapsulated Keggin-type POM $[PMo_{12}O_{40}]^{3-}$, enable electrochemical detection of H_2O_2 with a low detection limit of 1.03 μM, a broad linear range from 10–50 mM and an excellent selectivity and stability.[194] These electrocatalytic properties are believed to

result from synergistic effects between the redox activity of the POM, the high specific surface area of the MOF and the conductivity of the carbon material. The NENU-3 ($[PW_{12}O_{40}]^{3-}$@HKUST-1) and NENU-5 ($[PMo_{12}O_{40}]^{3-}$@HKUST-1) grown *in-situ* on carbon cloth have been obtained by a facile one-step solvothermal method.[193] Actually, these resulting materials behave as electrochemical sensors to detect bromate in aqueous solution with a low detection limit (0.55 and 1.18 μM for NENU-3 and NENU-5) and a large linear range (from 5 to 560 µmol L^{-1} for NENU-3 and from 15 to 380 µmol L^{-1} for NENU-5).

4.2.3.POMOFs

The electrocatalytic properties of POMOF compounds have been massively investigated with a special attention paid to the HER process, NO_2^- reduction, BrO_3^- reduction, IO_3^- reduction, H_2O_2 reduction and oxidation of ascorbic acid (see Tables 3 and 4).

The POMOFs built from the reduced ε-Keggin type POM capped by four zinc cations (see Figure 14A) have been identified as electrocatalytically active for hydrogen production in acidic conditions. Due to the insulating character of the POMOFs compounds, these solids are systematically combined with black carbon. The electrochemical properties and the HER activities of such POMOFs compounds have been evaluated in diluted H_2SO_4 aqueous solution. So far, the best HER properties have been observed for the compound NENU-500, formulated $(TBA)_3(\varepsilon\text{-}PMo_{12}O_{40}H_4Zn_4)(btb)_{4/3}$ (btb = benzene tribenzoate) exhibiting a 3D porous extended framework (see Figure 14B) with a permanent porosity (BET surface area = 195 $m^2\ g^{-1}$).[196] In 0.1 $mol \cdot L^{-1}$ H_2SO_4 aqueous solution, this compound shows three reversible redox waves, located at −0.09, +0.18, and +0.3 V *vs* Ag/AgCl (see Figure 14C). This electrochemical signature is similar to that observed for other POMOFs based on the ($\varepsilon\text{-}PMo_{12}O_{40}H_xZn_4$). These three redox waves are bielectronic. Two of them correspond to the reduction of the Mo^{VI} centers (events I and II), while the redox process observed at about +0.3V is thought to correspond to the oxidation of Mo^{V}. The polarization curves of the NENU-500 in 0.5 M H_2SO_4 revealed a

better HER electrocatalytic activity, featured by low overpotential (237 mV) and a Tafel plot of 96 mV dec^{-1}. This performance appears to be much higher than that observed for other POMOFs compounds (see Table 3), and has been attributed to the synergistic effects between the electrocatalytic activity of the POMs and porosity of the hybrid framework favoring the electrolyte diffusion to the catalytic sites.

Table 3. Electrocatalytic applications of POMOFs based on electron-rich ε-Keggin anion.

Anionic POM	Electrocatalytic Reaction	Overpotential (mV)	Tafel slope ($mV.dec^{-1}$)	Ref
$(TBA)_6[(\varepsilon\text{-}PMo_{12}O_{40}H_3Zn_4)_2(biphen)_3]$	HER pH = 1	N/A	N/A	197
$(TBA)_2[(\varepsilon\text{-}PMo_{12}O_{40}H_2Zn_4)(bim)_3(biphen)_{0.5}]$	HER pH = 1	N/A	N/A	197
$(TBA)_3[(\varepsilon\text{-}PMo_{12}O_{40}H_2Zn_4)(bim)_2(isop)]$	HER pH = 1	N/A	N/A	197
$(TBA)_{7/3}[(\varepsilon\text{-}PMo_{12}O_{40}H_2Zn_4)(bim)_2(trim)_{2/3}]$	HER pH = 1	N/A	N/A	197
$(TBA)_2(Co(2,2'\text{-}bipy)_3)[(\varepsilon\text{-}PMo_{12}O_{40}H_3Zn_4)_2(btb)_{4/3}]$	HER pH = 1	419 (10 mA cm^{-2})	N/A	198
$(Co(2,2'\text{-}bpy)_3)[(\varepsilon\text{-}PMo_{12}O_{40}H_3Zn_4)(trim)(2,2'\text{-}bpy)_2]$	HER pH = 1	452 (10 mA cm^{-2})	N/A	198
$(Ru(2,2'\text{-}bpy)_3)_3[(\varepsilon\text{-}PMo_{12}O_{40}H_2Zn_4)_2(trim)_2]$	HER pH = 1	617 (10 mA cm^{-2})	N/A	198
$(Ru(2,2'\text{-}bpy)_3)_3[(\varepsilon\text{-}PMo_{12}O_{40}H_3Zn_4)_2(biphen)_2]$	HER pH = 1	337 (10 mA cm^{-2})	N/A	198
$(PPh_4)[(\varepsilon\text{-}PMo_{12}O_{40}H_3Zn_4)_2(trim)_2]$	HER pH = 1	335 (10 mA cm^{-2})	N/A	198
$(TBA)_3[(\varepsilon\text{-}PMo_{12}O_{40}H_4Zn_4)(btb)_{4/3}]$	HER pH < 0.5	237 (10 mA cm^{-2})	96	196
$(TBA)_3[(\varepsilon\text{-}PMo_{12}O_{40}H_3Zn_4)(btt)]$	HER pH < 0.5	392 (10 mA cm^{-2})	137	196
$[\varepsilon\text{-}PMo_{12}O_{40}H_3Zn_4)(bimb)_2]$ + *ultrasmall Pt nanoparticles*	HER pH < 0.5	23 (10 mA cm^{-2})	71.3	199
$(TBA)_3[(\varepsilon\text{-}PMo_{12}O_{40}H_4Zn_4)(5\text{-}mip)_2]$	BrO_3^- reduction pH < 0.5	N/A	N/A	200
$(TBA)_3[(PMo_{12}O_{40}H_3Zn_4)_2(btb)]$	BrO_3^- reduction pH < 0.5	N/A	N/A	201
$(TBAOH)_{1.5}[(PMo_{12}O_{40}H_5Zn_4)_2(Co\text{-}TCPP)]$	CO_2 reduction pH = 7.2	N/A	98	202
$(TBAOH)_{1.5}[(PMo_{12}O_{40}H_5Zn_4)_2(Fe\text{-}TCPP)]$	CO_2 reduction pH = 7.2	N/A	211	202
$(TBAOH)_{1.5}[(PMo_{12}O_{40}H_5Zn_4)_2(Ni\text{-}TCPP)]$	CO_2 reduction pH = 7.2	N/A	675	202
$(TBAOH)_{1.5}[(PMo_{12}O_{40}H_5Zn_4)_2(Zn\text{-}TCPP)]$	CO_2 reduction pH = 7.2	N/A	206	202

Abbreviations: TBA = tetrabutylammonium; PPh = tetraphenylphosphonium; isop = 1,3-benzenedicarboxylate; trim = 1,3,5-benzenetricarboxylate; biphen = 4,4′-biphenyldicarboxylate; bim = benzimidazole; 2,2'-bpy = 2,2′-bipyridine; btt = [1,1′-biphenyl]-3,4′,5-tricarboxylate; bimb = 1,4-bis(imidazol-1-yl) benzene; btb = benzene tribenzoate; TCPP = tetrakis (4-carboxyphenyl) porphyrin; 5-mip = 5-methylisophthalate; N/A= not available

The HER electrocatalytic properties of POMOFs based on the reduced ε-Keggin type POM can be improved by doping with a low loading of Pt nanoparticles (<0.5 wt%).[199] The resulting

materials exhibited a remarkable HER performance in 0.5 M H_2SO_4 since it only requires an overpotential of 23 mV for a current density of about 10 mA cm^{-2}. Comparison with the commercial 20% Pt/C catalyst revealed the mass activity of Pt@POMOF was almost 100 times that of 20% Pt/C at an overpotential of 50 mV.

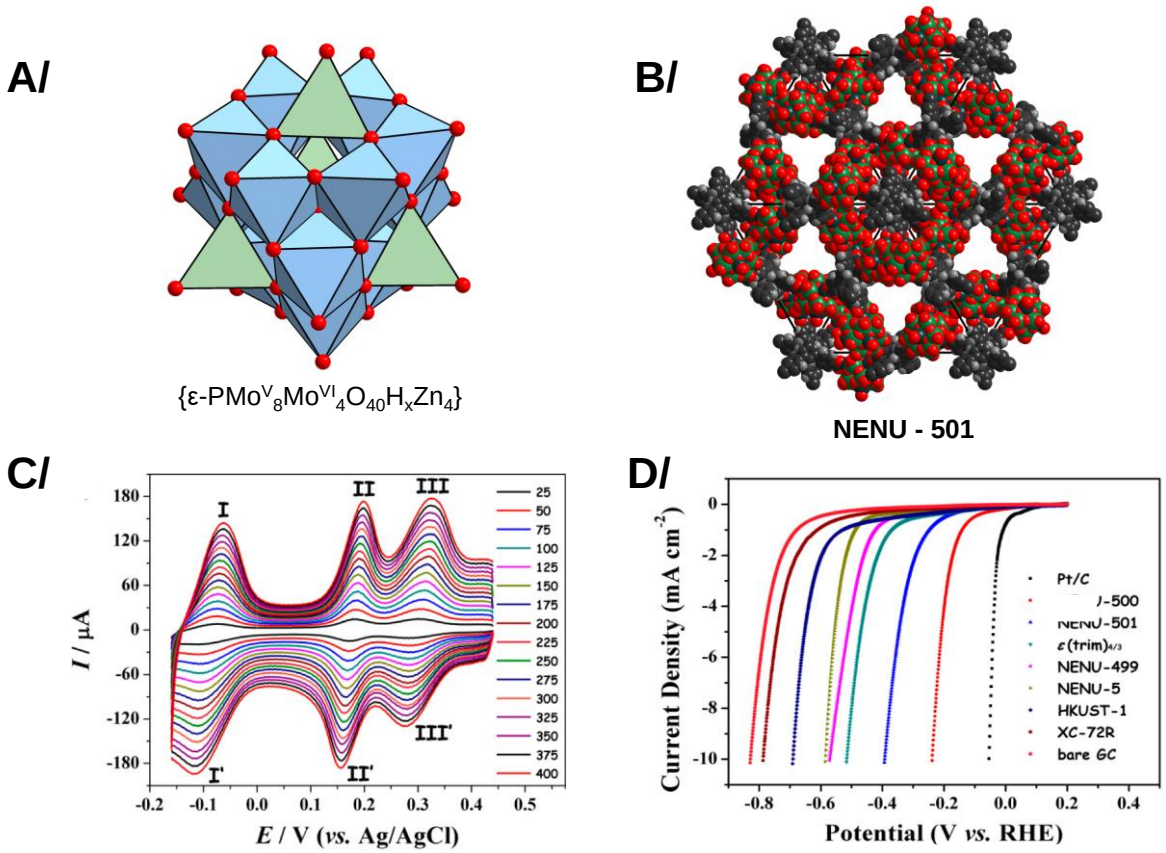

Figure 14. A/ Polyhedral representation of the Keggin core {ε-PMo$^{V}_{8}$Mo$^{VI}_{4}$O$_{36}$H$_x$Zn$_4$} with x= 2, 3, 4 or 5. B/ Space-filling representation of the compound (TBA)$_3$(ε-PMo$_{12}$O$_{40}$Zn$_4$)(btb)$_{4/3}$ (NENU- 501), showing voids in the hybrid organic-inorganic framework. C/ CVs of NENU-500-GCE at different scan rates (mV·s^{-1}) measured in 0.1 mol·L^{-1} H_2SO_4 aqueous solution. Adapted with permission from ref [196]. Copyright 2015 American Chemical Society. D/ Comparison of the polarization curve of the NENU-500-GCE (red curve) in 0.5 M H_2SO_4 aqueous solution with those obtained for other catalysts (other POMOFs or MOFs). Adapted with permission from ref 196. Copyright 2015 American Chemical Society.

Assembling electron-rich POMs, such as the ε-Keggin type POM capped by zinc cations, with metalloporphyrins to construct POMOFs, leads to highly stable, selective and efficient electrocatalysts for CO_2 reduction.[202] The performance of this material should arise from the presence of *i*) reduced POM units able to offer electrons, *ii*) the conjugated π-electron system

(metalloporphyrins) facilitating the electron mobility, and *iii*) the open hybrid framework which presumably induces an oriented electron transportation. Linear sweep voltammetry curves indicate that the POMOF material has a small onset potential of −0.35 V *vs* RHE for Co-based porphyrins in CO_2-saturated 0.5 M $KHCO_3$ (pH = 7.2) solution which is much less negative than that of the porphyrins containing other metals such as Fe (−0.53 V), Ni (−0.58 V) or Zn (−0.60 V). The POMOF containing Co centers selectively converted CO_2 to CO with a superior faradaic efficiency of 99% and high TOF of 1656 h^{-1} at −0.8 V *vs* RHE. These electrocalytic performances remained stable for more than 36 h of electrolysis.

In contrast to the POMOFs built from the ε-Keggin type POM, the POMOFs built from archetypal POMs, N-donor ligands and soft metal ions (Ag^{I}, $Cu^{I/II}$, Co^{II}..) have not yet been studied for HER or CO_2 reduction, but have been widely used for BrO_3^-, IO_3^-, H_2O_2 or NO_2^- reduction (see Table 3 and Table 4) and for the oxidation of ascorbic acid (see Table 4).

Table 4. Electrocatalytic applications of POMOFs built from the assembly of electron-poor POMs, transition metals and N-donor ligands.

Electrocatalytic Reaction	POMOF compounds[a]	Ref	Electrocatalytic Reaction	POMOF compounds[a]	Ref
BrO_3^- reduction *Acid media*	$Ag_4(2\text{-btz})_4(HPMo_{12}O_{40})$	203	IO_3^- reduction *p*H < 0.5	$Cu(bimb)_{1.5}(Mo_8O_{26})_{0.5}$	204
	$Ag_4(2\text{-btz})_4(SiW_{12}O_{40})$	203		$Cu(bimb)(Hbimb)_2(PMo_{12}O_{40})$	204
	$Ag_4(2\text{-btz})_4K(SiW_{12}O_{40})$	203		$Cu_4(bimb)_4(SiMo_{12}O_{40})$	204
	$Cu_4(2\text{-btz})_{16}(Mo_8O_{26})_2$	203		$Co_2(bimb)_3(VW_{12}O_{40})$	205
	$Cu_4(3\text{-btz})_8(PMo_{12}O_{40})_2$	203		$Co_5(bimb)_8(PW_{11}V_2O_{40})_2]$	206
	$Cu_7(3\text{-btz})_{16}(P_2W_{18}O_{62})_2$	203		$Co_2(bimb)_3(GeW_{12}O_{40})$	206
	$[Cu_2(2\text{-pdya})(CrMo_6(OH)_5O_{19})$	207		$Co_2(bimb)_2(BW_{12}O_{40})(Hbimb)$	206
	$Cu_4(\mu_3\text{-}OH)_2(3\text{-dpyh})(\gamma\text{-}Mo_8O_{27})$	207		$Co_2(bimb)_2(H_2W_{12}O_{40})(H_2bimb)$	206
	$Cu_3(3\text{-dpyb})_2(TeMo_6O_{24})$	207		$Cu(bimb)(BW_{12}O_{40})(H_2bimb)_2$	206
	$Cu_2(3\text{-dpyb})_2(C_2O_4)(CrMo_6(OH)_6O_{18})$	208		$(Hbib)Cu_2(bib)_2(PMo_{12}O_{40})$	209
	$Cu_4(OH)_2(4\text{-dpyh})(TeMo_6O_{24})$	208		$(Hbib)_2Cu(bib)(PMo_{12}O_{40})$	209
NO_2^- reduction *Acid or neutral media*	$Co_2(tib)_2(HBW_{12}O_{40})$	210	H_2O_2 reduction, *Acid or neutral media*	$(Hbib)Cu_2(bib)_2(PMo_{12}O_{40})$	209
	$Co_2(tib)_2(SiW_{12}O_{40})$	210		$(Hbib)_2Cu(bib)(PMo_{12}O_{40})$	209
	$Co_2(H_2tib)_4(BW_{12}O_{40})$	210		$Cu_2(3\text{-dpyb})_2(C_2O_4)(CrMo_6(OH)_6O_{18})$	208
	$Ag_4(2\text{-btz})_4(HPMo_{12}O_{40})$	203		$Cu_4(OH)_2(4\text{-dpyh})(TeMo_6O_{24})$	208
	$Ag_4(2\text{-btz})_4(SiW_{12}O_{40})$	203		$Cu_2(pbmbpc)_2(SiW_{12}O_{40})$	211
	$Ag_4(2\text{-btz})_4K(SiW_{12}O_{40})$	203		$Co_2(pbmbpc)_2(SiW_{12}O_{40})$	211
	$Cu_4(2\text{-btz})_{16}(Mo_8O_{26})_2$	203		$Ni_2(pbmbpc)_2(SiW_{12}O_{40})$	211
	$Cu_4(3\text{-btz})_8(PMo_{12}O_{40})_2$	203		$Ni_{13}(tri)_{24}(VW_{12}O_{40})_2$	212
	$Cu_7(3\text{-btz})_{16}(P_2W_{18}O_{62})_2$	203		$Ni_{13}(tri)_{24}(W_{10}V_5O_{40})(W_9V_6O_4)$	212
	$Cu_7(Hbat)_2(bat)_4(PMo_{12}O_{40})$	213		$[Cu_2(2\text{-pdya})(CrMo_6(OH)_5O_1)$	207
	$Ag_7(Hbat)_2(bat)_4(AsW_{12}O_{40})$	213		$Cu_4(\mu_3\text{-}OH)_2(3\text{-dpyh})(\gamma\text{-}Mo_8O_{27})$	207
	$Ag_9(H_2bim)_2(bim)_4(H_2PW_{12}O_{40})$	213		$Cu_3(3\text{-dpyb})_2(TeMo_6O_{24})$	207
	$(H_3bim)_3(H_2bim)(PMo_{12}O_{40})$	213		$Ag_4(2\text{-btz})_4(HPMo_{12}O_{40})$	203
	$Ni(Htib)_4(PW_{12}O_{40})_2$	214		$Ag_4(2\text{-btz})_4(SiW_{12}O_{40})$	203

	$Ni_2(tib)_2(GeW_{12}O_{40})$	214		$Ag_4(2\text{-}btz)_4K(SiW_{12}O_{40})$	203
	$Cu_2(pbmbpc)_2(SiW_{12}O_{40})$	211		$Cu_4(2\text{-}btz)_{16}(Mo_8O_{26})_2$	203
	$Co_2(pbmbpc)_2(SiW_{12}O_{40})$	211		$Cu_4(3\text{-}btz)_8(PMo_{12}O_{40})_2$	203
	$Ni_2(pbmbpc)_2(SiW_{12}O_{40})$	211		$Cu_7(3\text{-}btz)_{16}(P_2W_{18}O_{62})_2$	203
	$Ni_{13}(tri)_{24}(VW_{12}O_{40})_2$	212		$Co(icmp)(\beta\text{-}Mo_8O_{26})_{0.5}$	215
	$Ni_{13}(tri)_{24}(W_{10}V_5O_{40})(W_9V_6O_{40})$	212		$Co_2(icmp)_2(Mo_7O_{23})$	215
	$Co_2(tib)_2(HBW_{12}O_{40})$	210		$Co_2(icmp)_3(\beta\text{-}Mo_8O_{26})_{0.5}(\delta\text{-}Mo_8O_{26})_{0.5}$	215
	$Co_2(tib)_2(SiW_{12}O_{40})$	210		$Co_2(icmp)_3(H_4Mo_8O_{28})$	215
Ascorbic acid oxidation *Acid media*	$Co_2(H_2tib)_4(BW_{12}O_{40})$	210		$(Cu(pyr)_2)_6(As_2Mo_{18}O_{62})$	216
	$Co(icmp)(\beta\text{-}Mo_8O_{26})_{0.5}$	215		$(Cu(pyr)_2)_6(As_2Mo_{18}O_{62})$	216
	$Co_2(icmp)_2(Mo_7O_{23})$	215	Ascorbic acid oxidation *Acid media*	$Ni(Htib)_4(PW_{12}O_{40})_2$	214
	$Co_2(icmp)_3(\beta\text{-}Mo_8O_{26})_{0.5}(\delta\text{-}Mo_8O_{26})_{0.5}$	215		$Ni_2(tib)_2(GeW_{12}O_{40})$	214
	$Co_2(icmp)_3(H_4Mo_8O_{28})$	215			214

Abbreviations: bim = benzimidazole; 2,2'-bpy = 2,2′-bipyridine; btt = [1,1′-biphenyl]-3,4′,5-tricarboxylate; bimb = 1,4-bis(imidazol-1-yl) benzene ; 5-mip = 5-methylisophthalate. tib = 1,3,5-tris(1-imidazoly)benzene), 2-btz = 1-benzyl-1H-(1,2,4)triazole ; 3-btz = 1-benzyl-1H-(1,3,4)triazole ; icmp = 1,3-bis(1H-imidazole-4-carboxamido)metaphenylene ; pyr = pyrazole ; bat = benzotriazolate; 2-pdya = pyridyl–pyrazinamide 2-pyridyl–pyrazinamide ; 3-dpyb = *N*,*N*′-bis(3-pyridinecarboxamide)-1,4-butane, 3-dpyh = *N*,*N*′-bis(3-pyridinecarboxamide)-1,6-hexane) ; pbmbpc = 1,1′-(1,4-phenylene-bis(methylene))-bis(pyridine-3-carboxylic acid) ; tri = 1,2,4-triazole ; bib = 4-bis(imidazol-1-yl) benzene). [a] The solvent molecules (H_2O, DMF…) have been removed from the compound formula.

4.3. Carbon-based composite material/POM

4.3.1. POMs attached to reduced graphene oxide (POM/rGO)

The electrical conductivity properties of graphene make this 2D material an ideal candidate to elaborate POM-based electrocatalysts. However, the preparation of defect-free and single-layer graphene in large quantities is still a process under development. In contrast, the preparation of graphite oxide, which consists of stacks of individual graphene oxide (GO) sheets, is much easier and well mastered since the publication of the Hummer method in 1958.[217] Despite its ability to be completely exfoliated to individual GO sheets in different solvents, GO exhibits low conductivity due to the presence of the numerous oxygen functional groups. However, the properties of GO can be restored, at least partially, to those of graphene by reduction process. The resulting reduced graphene oxide (rGO) has been largely employed to develop POM/rGO composite electrocatalysts which were catalytically active for HER,[218,219] OER, ORR, alcohol oxidation, nitrite oxidation/reduction, or formic acid oxidation. Table 5 summarizes the different POM/rGO based systems used for electrocatalytic purposes.

Table 5. POM/rGO based systems for electrocatalytic applications.

POM	Carbon materials	Electrocatalytic Reaction	Overpotential (mV)	Tafel slope ($mV.dec^{-1}$)	Ref
$[H_7P_8W_{48}O_{184}]^{33-}$	rGO	HER pH < 0.5	28	38	218
$[H_2W_{12}O_{40}]^{6-}$	rGO	HER pH < 0.5	188	N/A	218
$[P_2W_{18}O_{62}]^{6-}$	rGO flakes	HER pH < 0.5	35	37	219
$[P_5W_{30}O_{110}]^{15-}$	rGO flakes	HER pH < 0.5	33	33	219
$[H_7P_8W_{48}O_{184}]^{33-}$	rGO flakes	HER pH < 0.5	44	41	219
$[PW_{11}NiO_{39}]^{5-}$	rGO	HER pH < 0.5	550-700	N/A	220
$[PW_{11}NiO_{39}]^{5-}$	rGO with Ru NPs	HER pH < 0.5	480	N/A	221
$[PW_{11}CoO_{39}]^{5-}$	rGO with Ru NPs	HER pH < 0.5	500	N/A	221
$[PW_{11}CuO_{39}]^{5-}$	rGO with Ru NPs	HER pH < 0.5	590	N/A	221
$[PMo_{12}O_{40}]^{3-}$	rGO with Au@Pd NPs	HER pH < 0.5	109	N/A	222
$[PW_{12}O_{40}]^{3-}$	rGO with Pt NPs and with cationic polymer (PDDA)	OER pH = 7	540 mV	190	223
$[PW_{12}O_{40}]^{3-}$	rGO with Ag NPs	ORR pH=13	N/A	N/A	224
$[\{(PW_9O_{34})Ni_3(OH)(H_2O)_2(alen)\}_2Ni]$	rGO	ORR pH=7	N/A	N/A	225
$[PMo_{12}O_{40}]^{3-}$	rGO with Pt NPs	Methanol oxidation	N/A	N/A	226
$[PMo_{12}O_{40}]^{3-}$	rGO with Pt NPs	Methanol oxidation	N/A	N/A	227
$[PW_{12}O_{40}]^{3-}$	rGO with PdNi NPs	Methanol oxidation	N/A	N/A	228
$[PW_{12}O_{40}]^{3-}$	rGO with PdNi NPs	Ethanol oxidation	N/A	N/A	228
$[PMo_{12}O_{40}]^{3-}$	rGO with Au@Pd NPs	Ethanol oxidation pH > 13	N/A	N/A	222
$[PMo_{12}O_{40}]^{3-}$	rGO	H_2O_2 reduction	N/A	N/A	229
$[PMo_{12}O_{40}]^{3-}$	rGO	H_2O_2 reduction	N/A	N/A	230
$[PMo_{12}O_{40}]^{3-}$	rGO	NO_2^- reduction	N/A	N/A	229
$[PMo_{11}VO_{40}]^{4-}$	PDDA- rGO	NO_2^- oxidation	N/A	N/A	231
$[PMo_{10}V_2O_{40}]^{5-}$	rGO with cationic polymers (PDDA)	NO_2^- oxidation	N/A	N/A	232
$[PMo_{11}VO_{40}]^{4-}$	rGO with cationic Gemini surfactants	NO_2^- oxidation	N/A	N/A	233
$[SiMo_{12}O_{40}]^{4-}$	rGO with chitosan	$S_2O_8^{2-}$ reduction	N/A	N/A	234
$[PMo_{10}V_2O_{40}]^{5-}$	rGO with cationic polymers (PDDA)	Dopamine oxidation	N/A	N/A	232
$[PMo_{10}V_2O_{40}]^{5-}$	rGO with cationic polymers (PDDA)	Ascorbic acid oxidation	N/A	N/A	232

Abbreviations: rGO= reduced graphene oxide; NPs= nanoparticles; PDDA= polydiallyldimethylammonium; alen= alendronate

The POM/rGO and NPs/POM/rGO (NPs: nanoparticles) composite electrocatalysts materials are generally prepared from an acidic aqueous mixture of reduced "heteropoly blues" POMs and graphene oxide (see Figure 15). The reduced POMs, usually belonging to the structural Type I and III, are reduced chemically, electrochemically or also photochemically in acidic aqueous medium, generating a solution of "heteropoly blues". It must be noticed the reduction state of the POMs is rarely reported in the synthetic procedures.[218,219] Then, a redox reaction between reduced POMs and graphene oxide occurs, giving rise to reduced graphene

oxide decorated by oxidized POMs. Such nanocomposites are usually characterized by microscopy techniques (low-magnification HAADF-STEM, EDS, TEM), XPS, Raman and FT-IR spectroscopies. Electron microscopy images and EDS analysis enable to control the good dispersion of the POMs on rGO surface. Raman and XPS spectroscopies allow the characterization of the rGO and evidence the decrease of oxygen functional groups (alcohols, epoxides, and carboxylic acids) concomitantly with the restoration of the sp^3/sp^2-hybridized carbon structures. IR and Raman spectroscopies combined with elemental analysis are particularly useful to assess the integrity of the POMs. Furthermore, it is worth mentioning that the solid-state NMR (^{31}P MAS) spectroscopy provides further structural insights on phosphorous-containing POMs attached to reduced graphene oxide.[218]

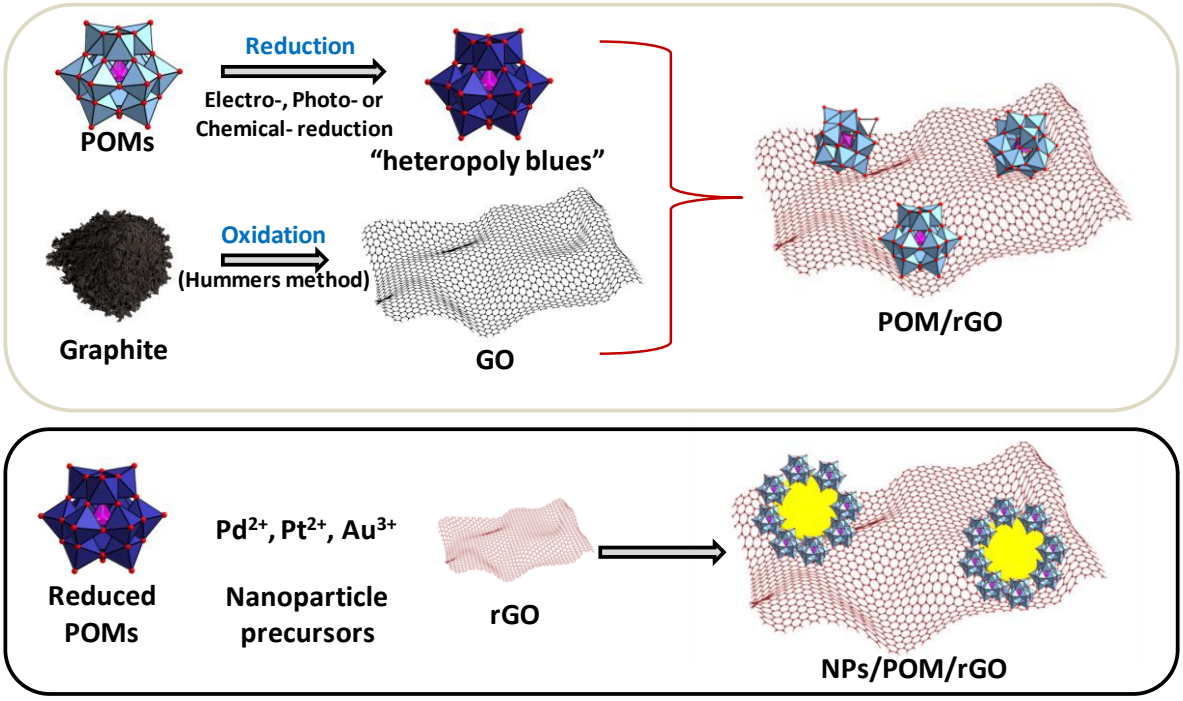

Figure 15. Schematic representations of the preparation of the POM/rGO and the NPs/POM/rGO composites.

Reported studies from different groups have evidenced the POM/rGO nanocomposites are excellent HER electrocatalysts characterized by both low overpotentials and small Tafel slopes, highlighting the excellent electrocatalytic activity of this material built exclusively from Earth-

abundant elements with performance metrics close to those of the state-of-the-art catalyst Pt/C.[218,219] It is also important to mention these excellent HER electrocatalysts are exclusively obtained with pure polyoxotungstates or polyoxomolybdates. In contrast, transition metal-containing POMs exhibit much lower electrocatalytic performance, even when Ru nanoparticles are present within the composite material.[221] Importantly, it should be mentioned the polyoxotungstate based rGO materials required an electrochemical activation step involving ~20 voltammetric cycles in the potential range -0.4 to +0.7 V *vs* RHE. This activation step yields a dramatic decrease of the overpotential (> 200 mV, see Figure 16A), associated with stable HER response. While the nature of this activation process remains unclear, it was proposed the exceptional high HER activity of polyoxotungstate/rGO composite was due to "microenvironment effects" resulting from the combination of high-quality rGO and a polyoxometalate behaving as high capacity proton and electron reservoir.[218] Activated polyoxotungstate/rGO composite materials exhibited long-term electrochemical stability for up to 1000 potential sweeps (see Figure 16A).[218,219] Systematic studies reported by Freire and co-workers revealed that the nature of the polyoxotungstate anions influenced moderately the HER activity. However, any clear trend has been observed since many other significant factors have also to be taken in consideration (POM shape, size, charge, composition, and redox activity).

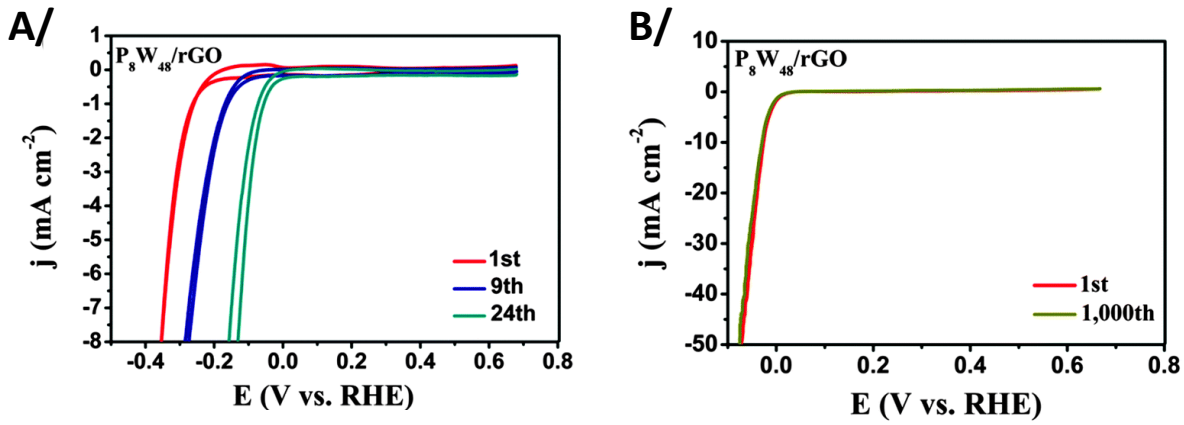

Figure 16. A) Evolution of the cyclic voltammograms of P_8W_{48}/rGO over a potentiodynamical cycling and B) stability tests for P_8W_{48}/rGO in 0.5 M H_2SO_4, initially and after 1,000 scans between +0.20 and

−0.30 V *vs.* RHE at 100 mV s^{-1}. Adapted with permission from ref 218. Copyright 2016 Royal Society of Chemistry.

POM/rGO composites in which the anionic 3d-substituted POM is associated with a cationic copper coordination complex, exhibit ORR activity in both neutral and basic media.[225] ORR electrocatalytic activity in basic medium (pH = 13) has also been observed for AgNPs/POM/rGO composites containing 15 nm-diameter Ag nanoparticles and a Keggin-type $[PW_{12}O_{40}]^{3-}$. The authors claimed the AgNPs/POM/rGO composite exhibited excellent long-term stability, supported by the measured so-called constant electrocatalytic current. However, poor hydrolytic stability of Keggin-type $[PW_{12}O_{40}]^{3-}$ at pH = 13 should lead to the POM degradation under such electrochemical conditions, and therefore the real catalyst is most likely generated from the hydrolytic degradation of the $[PW_{12}O_{40}]^{3-}$ ion.

4.3.2. Carbon nanotubes

The direct encapsulation of POMs within carbon nanotubes (CNTs) has been perceived as incompatible due to the apparent mismatch between the water-soluble POMs and the hydrophobic interiors of the CNTs. Consequently, pioneered studies on the association of POMs and CNTs have been achieved by either electrostatic grafting on cationic functionalized CNTs or functionalized POMs attached to the surface of CNTs through π–π interactions.[235–237] These methodologies required sophisticated time-consuming methodologies based on low-yield multi-step processes and constituted therefore an important drawback for the use of such advanced materials in some applications. Moreover, the covalent link can be hydrolytically fragile preventing its use in aqueous media and the conductivity of the CNTs can be dramatically reduced by the covalent modification of the sp^2 surface carbon.

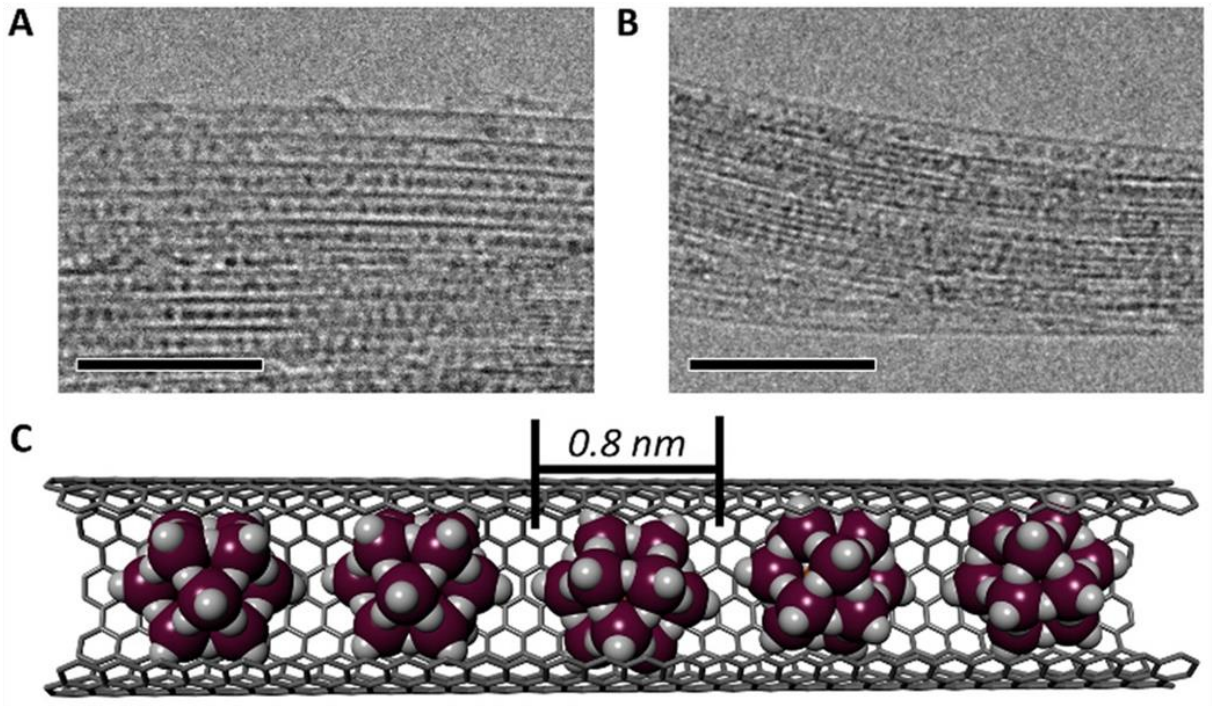

Figure 17. High-magnification transmission electron microscopy (TEM) images of polyoxomolybdates encapsulated $\{PMo_{12}O_{40}\}$ (A) and $\{P_2Mo_{18}O_{62}\}$ (B) within single-walled carbon nanotubes (SWNT). C) Illustration of host–guest structural arrangement of $\{PMo_{12}O_{40}\}$@SWNT. The POM units are closely packed and uniformly dispersed inside the nanotube. Adapted with permission from ref 238. Copyright 2022 Wiley-VCH.

It was recently evidenced that single-walled CNTs (SWNTs) and low charge density POMs, such as $[PM_{12}O_{40}]^{3-}$ and $[P_2M_{18}O_{62}]^{6-}$ with M = Mo or W, could spontaneously form in water host-guest POM@CNT nanohybrid materials.[238–240] TEM analysis of such systems has demonstrated the entrapment of POMs within the nanotube (see Figure 17), that are closely packed together defining POM-based wires. The mechanism of this nano-confinement occurs through a charge transfer that arises from the spontaneous reduction of the POMs and the concomitant oxidation of the CNTs. This redox process facilitates the encapsulation of the POMs within the CNTs, that can be mostly described as electrostatic interactions supported by desolvation of the chaotropic POMs. The formation of such unique host-guest systems requires that the redox potential of the first electron transfer step of the POM is more positive than the top of the valence band of CNTs. It was observed this encapsulation within the CNTs did not occur in acetonitrile, because the redox potential of the first reduction event of the POM was

dramatically shifted toward negative potentials in this solvent, preventing consequently the redox reaction between the POM and the CNTs. In such confining situations, the redox activity of the encapsulated POMs appears fully retained. More importantly, it was demonstrated that the nano-encapsulation of the POMs conferred a significant hydrolytic stability to POMs even in basic solution such as 1M NaOH. Clearly, all these recent discoveries offer new perspectives in the use of the host-guest POM@CNT hybrid materials for applications in (photo)electrocatalysis.

Table 6. POM/CNTs based systems for electrocatalytic applications

POM	Carbon materials	Electrocatalytic Reaction	Ref
$[PMo_{12}O_{40}]^{3-}$ $[PMo_{11}VO_{40}]^{4-}$ $[PMo_{10}V_2O_{40}]^{5-}$	Single-walled CNTs	Oxidation of ascorbic acid (pH = 2.5)	241
$[PMo_{11}O_{39}]^{7-}$	Single-walled CNTs	Reduction of NO_2^- *p*H=1	242
$[PMo_{11}VO_{40}]^{4-}$	Single-walled CNTs	ORR *p*H=2.5	243
$[Co_4(H_2O)_2(PW_9O_{34})_2]^{10-}$	Multi-walled CNTs	Triiodide reduction	244
$[PMo_{12}O_{40}]^{3-}$	Multi-walled CNTs + Polyanline	Reduction of IO_3^-	245
$[PMo_{11}VO_{40}]^{4-}$ $[PMo_{10}V_2O_{40}]^{5-}$ $[PMo_9V_3O_{40}]^{3-}$	Multi-walled CNTs + Ag@Pt	ORR	246

Before the recent discovery evidencing Keggin anions are spontaneous encapsulated by SWCNTs when the both entities are in water, few studies was reported on the electrocatalytic activities of hybrid systems resulting from the association of POMs $\{PMo_{12-x}V_xO_{40}\}$ and SWCNTs in organic solvents (see Table 6).[241] The characterizations of $\{PMo_{12-x}V_xO_{40}\}$/SWCNT composites did not provide any experimental evidence on the encapsulation phenomenon. The electrocatalytic performance of $\{PMo_{12-x}V_xO_{40}\}$/SWCNT materials toward the ascorbic acid oxidation was superior to that of the free POM. This efficieny enhancement arises from the strong electronic communication between POMs $\{PMo_{12-x}V_xO_{40}\}$ and

SWCNTs. Using the same synthetic way, the hybrid materials prepared by incorporation of $\{PMo_{11}VO_{40}\}$ in CNTs, showed an electrocatalytic activity for ORR in acid medium.[243] It was observed that the electrocatalytic ORR performance was better when $\{PMo_{11}VO_{40}\}$ was associated with CNTs than when this POM was combined with carbon black. Nevertheless, graphene appears to be the best carbon-based matrix for boosting the ORR activity of $\{PMo_{11}VO_{40}\}$. Similarly, composite materials based on single-walled CNTs and lacunary Keggin-type POMs, such as $[PMo_{11}O_{39}]^{7-}$, have proven to be effective for the electrocatalytic reduction of NO_2^-.[242] This system has been elaborate with the perspective of developing amperometric sensors for nitrite ions. Such a sensor exhibited a low detection limit, a wide range of the response linearity and also low sensitivity towards interfering ions such as phosphate, chlorate or nitrate.

Some electrocatalysts prepared from POMs and multi-walled CNTs have been studied for various other applications.[244–246] Among them, the highly dispersed POM/CNT nanocomposites prepared by a simple ultrasonic driving strategy, have been identified as efficient electrocatalysts for the triiodide reduction in dye-sensitized solar cells.[244] For such electrocatalytic reactions, a series of POMs ($[PMo_{12}O_{40}]^{3-}$, $[PW_{12}O_{40}]^{3-}$, $[P_2Mo_{18}O_{62}]^{6-}$, $[P_2W_{18}O_{62}]^{6-}$ and $[Co_4(H_2O)_2(PW_9O_{34})_2]^{10-}$) have been tested and the Co-containing POM showed the best performances.

4.4. POM/Metal composites

4.4.1. Ni foam

Metal foams, and particularly Ni foam, have been used as POMs immobilization supports in order to take advantage of their well-established conducting and three-dimensional porous nature, their high accessible specific area and high electronic conductivity as well. Such characteristics are thus beneficial for generating high electrochemical currents with improved mass transfer and facilitated release of gas bubbles (e.g. H_2 and O_2) during the HER and OER

electrolytic tests.[247] Also interestingly, Ni foam may play a dual role acting as both a conducting electrode with high specific area and a material chemically reacting with POMs to form composites, as highlighted by Streb and co-workers.[248] In their report, Dexter-Silverton POM microcrystals $[M_8W_{12}O_{42}(OH)_4(H_2O)_8]$ (with M = Co, Zn, Mn) were synthesized on Ni foam by hydrothermal reaction between a Keggin-type POM precursor $[PW_{12}O_{40}]^{3-}$ and a transition metal (Ni, Co, Mn, Zn) salt in the presence of Ni foam (Figure 18). During this step, Ni^{2+} ions were released from the Ni foam and were incorporated into the POM lattice to generate the composite NiM-POM/Ni. Among the as-prepared composites, the NiCo-POM/Ni exhibited the best electrocatalytic performance for HER in alkaline aqueous solution (pH 13) with low overpotential of 64 mV at 10 mA cm^{-2} and without significant degradation of its electrochemical response after 2,000 voltammetric cycles.[248]

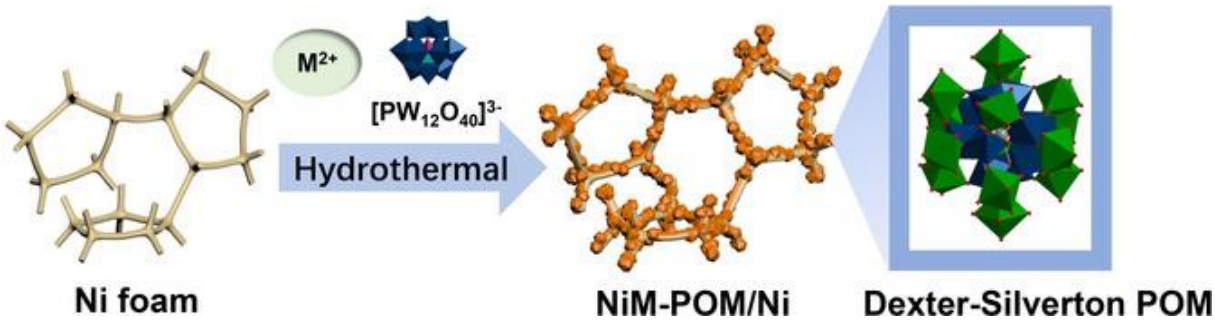

Figure 18. Left) Deposition of Dexter-Silverton polyoxometalate microcrystals on Ni foam electrode. Right) Structural representation of the Dexter–Silverton POM catalyst. W blue, Ni grey, M (M=Co, Zn, Mn) green, O red and hydrogen atoms omitted for clarity. Reprinted with permission from ref [248]. Copyright 2019 Wiley-VCH.

Such an electrode also showed a remarkable OER activity (360 mV overpotential at 10 mA cm^{-2}) under the same pH conditions, with no chemical or mechanical degradation observed after prolonged operation time (>10 h) as evidenced by post-electrolysis SEM and XRD data.[249]

The decoration of such Dexter-Silverton POM-based composites with transition metal based phosphides, such as Co_2P, yielded bifunctional electrodes active for both HER and OER in alkaline medium, with overpotentials of 130 mV and 336 mV at 50 mA cm^{-2} for HER and OER, respectively.[250] Besides metal phosphides, earth-abundant transition metal sulfides have also

emerged as low-cost and bifunctional electrocatalysts for HER and OER.[251] Thus, such POMs-incorporating heterostructures constitute good candidates for boosting both the electrocatalytic activity and the stability in operation. So, Keggin-type $[PW_{12}O_{40}]^{3-}$ anchored ZnCo sulfide nanowires on Ni foam displayed significantly low HER and OER overpotentials of 170/337 and 200/300 mV to reach a current density of 10/40 and 20/50 mA cm^{-2}, respectively.[252]

In another study, a tetra-ruthenium-containing POM $[Ru_4O_4(OH)_2(H_2O)_4(\gamma\text{-}SiW_{10}O_{36})_2]^{10-}$ was immobilized on nickel foam through a silane coupling and the POM-modified electrode was effective for OER under near neutral pH conditions (pH 6) with a moderate 550 mV overpotential at 10 mA cm^{-2} and a stability in operation longer than 10 h.[253] As emphasized in Section 4.1, the frequently remarkable stability of these aforementioned composites under such electrochemical conditions (both alkaline and oxidative) is somewhat unexpected even though experimental evidence has been provided in the concerned reports on both the chemical and structural integrity of immobilized POMs. Besides heteropolyoxotungstates, polyoxomolybdates in the form of organometallic-functionalized POM clusters, $H_3[(Cp^*Rh)_4(PMo_8O_{32})]$ and $H_5[Na_2(Cp^*Ir)_4PMo_8O_{34}]$ (with Cp = cyclopentadienyl), have been attached onto nickel foam through a hydrothermal process.[254] The electrocatalytic activity of the so modified electrodes has been examined for HER in 0.1M KOH. The immobilized POMs were converted to metal oxide MoO_2 after a 48h electrolysis and the newly generated material exhibited significantly higher electrocatalytic HER rates than their parent POMs.

4.4.2. Metal nanostructures

The passivation of catalytically active metal nanostructures by POMs acting as inorganic ligands is a valuable strategy to elaborate nanomaterials with controllable size and morphology exhibiting synergistic effects for electrocatalytic reactions of interest. The most commonly explored method to produce such POM/Metal composites consists in the electrochemical reduction of a metal salt in the presence of reduced POM.[255] Following this way, semi-noble

(Ag),[256] noble (Au,[257,258] Pt[259,260] and Pd[259,261–264]) and transition (Cu[262,265]) metal nanostructures (nanoparticles, nanocrystals and nanodendrites) have been decorated and stabilized with various POM shells (Figure 19). Interestingly, the POMs may play a crucial role in both the nucleation and growth kinetics of metal nanostructures, giving access to different morphology-controlled nanostructures.[261] Owing to its high reduction potential and the propensity of its reduced form to strongly adsorb on various types of surfaces,[266] the Keggin-type $[PMo_{12}O_{40}]^{3-}$ was the most employed POM to produce POM/Metal composites with controlled morphology. Globally, the electrocatalytic performance of the POM/Metal nanostructures for diverse reactions of interest was superior to those of metal and POM components tested alone. Clear synergistic effects resulting in an decrease in the overpotential, an enhancement in the electrocatalytic current density and an improvement of the stability of the catalytic electrodes in operation, were reported for the electrocatalysis of CO_2-to-CO reduction,[256] alcohol[257,259,263] or formic acid[261,262] oxidation, HER[260,265] and O_2[264] reduction (see Table 7). Such a catalytic performance enhancement was ascribed not only to well-known remarkable electron reservoir/transfer properties of POMs[265] but also to changes in the electronic structure of metal induced by the POM[264] or a strong interaction between the POM and some reaction intermediates.[256,261] As a representative example, $[PMo_{12}O_{40}]^{3-}$ boosted the catalytic activity of Pd nanocrystals toward formic acid oxidation owing to the formation of oxygen-containing species at a lower potential following the easy activation of water molecules by Mo atoms present in $[PMo_{12}O_{40}]^{3-}$.[261] This event resulted in an increase of the measured peak current densities and the corresponding mass activity of $[PMo_{12}O_{40}]^{3-}$/Pd nanocrystals by three and two times, respectively, compared with POM-free Pd nanocrystals.

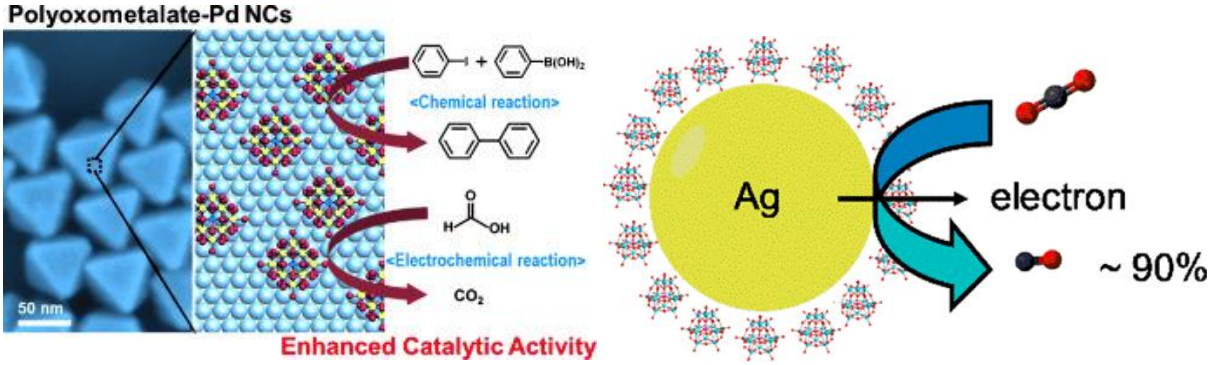

Figure 19. POM/Metal nanostructures composites. Left) POM/Pd nanocrystals with controlled shapes and sizes for the electrocatalytic oxidation of formic acid to CO_2. Reprinted with permission from ref [261]. Copyright 2015 Wiley-VCH Right) Adsorption of POMs on the surface of Ag nanoparticles for the electrocatalytic reduction of CO_2 to CO. Adapted with permission from ref [267]. Copyright 2018 American Chemical Society.

Table 7. POM/Metal nanostructures composites.

POM	Metal nanostructures	Shape	Electrocatalytic reaction	Ref
$[PMo_{12}O_{40}]^{3-}$	Ag	Oval-shaped NPs	CO_2-to-CO reduction	256
$[PMo_{12}O_{40}]^{3-}$	Au	Spherical NPs	Ethanol oxidation	257
$[PW_{12}O_{40}]^{3-}$	Au	Pseudo-spherical NPs	Acetaminophenol or NADH oxidation, H_2O_2 reduction	258
$[PMo_{12}O_{40}]^{3-}$	Pd@Pt	Core-shell octahedral NCs	Methanol oxidation	259
$[SiW_{11}O_{39}]^{8-}$, $[SiW_{12}O_{40}]^{4-}$, $[P_2W_{18}O_{62}]^{6-}$	Pt	Pseudo-spherical NPs	HER	260
$[PMo_{12}O_{40}]^{3-}$	Pd	Octahedral, cubic and concave cubic NCs	Formic acid oxidation	261
$[PW_{12}O_{40}]^{3-}$	PdCu	Bimetallic spherical NPs	Formic acid oxidation	262
$[PMo_{12}O_{40}]^{3-}$	Pd	Pseudo-spherical NPs	Ethanol oxidation	263
$[PMo_{12}O_{40}]^{3-}$	Pd	Pseudo-spherical NPs	O_2 reduction	264
$[H_6NiMo_6O_{24}]^{4-}$, $[H_6CrMo_6O_{24}]^{3-}$, $[H_6AlMo_6O_{24}]^{3-}$	Cu	Dendrites	HER	265

Abbreviation**s:** NPs = Nanoparticles; NCs = Nanocrystals. NADH = Nicotinamide adenine dinucleotide

5. POMs-Functionalized Semiconducting Photoelectrodes

As emphasized in Section 3.2, the use of photoactive semiconducting materials as immobilization supports for POMs provides a real benefit in the field of the electrochemical catalysis because it allows that the electrocatalytic process to be activated by light. This energy-saving route is therefore an exciting solution to convert solar power into clean, energy dense and storable fuels, such as H_2 and CO_2 reduction products. In that context, numerous SCs with a bandgap comprised in the range of 1.1 eV (Si) to 3.2 eV (TiO_2) have been derivatized with POMs to efficiently promote light-driven cathodic or anodic reactions (Figure 8). Among these SCs, silicon has appeared as one of the most promising candidates to be used as a photocathode because of its abundance, biocompatibility, and ability to harvest photons from a large portion of the solar spectrum, as well as its tunable electronic properties.[268,269] Moreover, the position of its conduction band is particularly appropriate relatively to the H^+/H_2 redox potential for HER and the different proton-assisted multielectron reduction potentials for CO_2.[268,270,271] Nevertheless, bare silicon like other SCs fail to promote efficient multielectron transfers because of slow charge-transfer kinetics.[268,272] Additionally, these are often susceptible to be degraded under certain harsh electrochemical conditions by the notorious photocorrosion phenomenom. Therefore, the interfacing between the semiconductor and the POM constitutes a critical step to sustain an efficient and durable photoelectrocatalysis. Toward this goal, some essential criteria must be fulfilled to prepare catalytically effective POM-functionalized photoelectrodes. Although it is obvious for an electrocatalyst, the immobilization of POM onto an appropriate semiconducting surface must lead to an increase in the charge transfer kinetics. Second, the immobilized POM alone or tied to another stabilizing coating must efficiently and durably protect the SC while not substantially reducing light intensity transmitted to the SC.

Lacunary Keggin $[PW_{11}O_{39}]^{7-}$-type POM hybrids have been covalently grafted on Si/SiO_2 substrates through carboxylic acid binding units.[273] However, the presence of electrically

insulating SiO_2 layer precluded the use of these modified surfaces for photoelectrocatalytic purposes. Improved interfacial electron transfer properties have been obtained when these hybrid assemblies were covalently attached to hydrogen-terminated, oxide-free Si (Si-H) surfaces through the aryldiazonium chemistry.[274,275] Unlike SiO_2, Si-H possesses a very low density of electrically active surface defects (the so-called surface states),[276,277] which renders it particularly attractive for electrical applications. But again, the applied grafting procedure has introduced a significant amount of surface silicon oxide resulting from Si-H decomposition. Using the secondary functionalization of Si-H based on the two-step chlorination/methylation procedure pioneered by the N. S. Lewis' group,[278] M. J. Rose and co-workers have prepared high electronic quality and densely packed lacunary Keggin $[PW_{11}O_{39}]^{7-}$ POM monolayers covalently bound to *p*- or *n*-type Si(111).[279] Despite promising photoelectrochemical properties evidencing the redox integrity of the POM after immobilization with 150-310 mV photovoltage values, these POM-modified photoelectrodes have not been used for photoelectrocatalytic applications. The principal drawback of the monolayer approach vs multilayer/polymer one for electrocatalytic applications is that it leads usually to smaller surface coverage of the electrocatalyst and smaller electrochemical currents which often make less efficient electrocatalysis, weaker apparent electrochemical stability, and less efficient passivating layer.[154]

Recently, Fabre, Cadot and co-workers have reported on the remarkable catalytic properties for HER of silicon photocathodes functionalized with polyoxothiometalate-incorporating polymer assemblies. The so-called anionic thio-POM resulting from the covalent association of the $[Mo_3S_4(H_2O)_9]^{4+}$ cluster with the robust macrocyclic polyoxotungstate $[H_7P_8W_{48}O_{184}]^{33-}$ was electrostatically entrapped into a conducting polymer film, namely poly(3,4-ethylenedioxythiophene) (PEDOT) to retain durably the catalyst at the interface of the silicon photocathode.[138] In the context of HER, it makes sense to covalently link such an

electron/proton collecting POM module to the $[Mo_3S_4(H_2O)_9]^{4+}$ core which has been identified as one as the most promising MoS_x-based HER electrocatalysts.[138,280] This covalent association produced a striking synergistic effect featured by high HER performance both in homogeneous conditions[138,281,282] and in supported phase using a microstructured silicon surface[283,284,285] as the immobilization substrate instead of flat silicon. So, this molecular and material engineering strategy has led to thio-POM/PEDOT-coated micropyramidal silicon photocathodes able to produce H_2 under one Sun illumination at a rate of ca. 100 μmol cm^{-2} h^{-1} at 0 V *vs* RHE (Figure 20).[138]

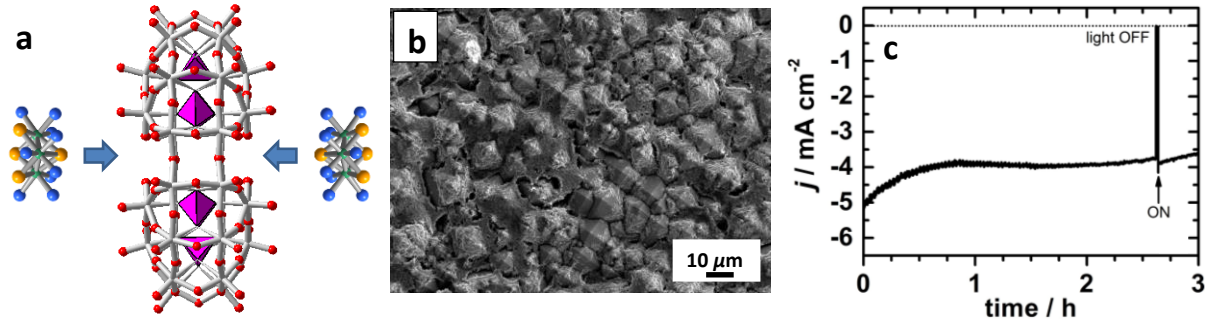

Figure 20. Polyoxothiometalate (thio-POM)/PEDOT-coated micropyramidal silicon photocathodes for solar-driven HER. (a) Schematic view of the electrocatalyst resulting from the covalent association of $[Mo_3S_4(H_2O)_9]^{4+}$ cluster with the robust macrocyclic polyoxotungstate $[H_7P_8W_{48}O_{184}]^{33-}$; (b) SEM picture of the thio-POM/PEDOT-coated micropyramidal silicon surface and (c) photocurrent density-time curve obtained during the potentiostatic electrolysis at 0 V vs RHE using the functionalized photocathode under simulated sunlight (AM 1.5G, 100 mW cm^{-2}) in 1.0 mol L^{-1} H_2SO_4. Adapted with permission from ref 138. Copyright 2019 American Chemical Society.

Besides silicon, a *p*-type Cu_2O photocathode with a direct bandgap of 2.0 eV (Figure 10) has been modified with a catalytic multilayer of anionic Ni-containing Weakley-type POM $[Ni_4(H_2O)_2(PW_9O_{34})_2]^{10-}$ using a cationic polyethyleneimine as an electrostatic adhesive.[286] The POM-incorporating multilayer is expected to enhance catalytic charge transfer and protect Cu_2O against some detrimental reactions, such as its well-documented deactivation to CuO and Cu by self-oxidation and photocorrosion, respectively.[287,288] Despite a significant improvement in the stability of the photocathode under HER electrolytic conditions, the maximum

photocurrent densities reached for the POM-functionalized photocathode were quite low (ca. 0.2 mA cm^{-2} at 0.35 V *vs* RHE) and only weakly higher than those measured for a bare Cu_2O photocathode.[286]

In parallel to these POM-modified *p*-type SC photocathodes designed for photoelectrocatalytic HER, some studies focused on the fabrication of POM-modified *n*-type photoanodes to catalytically promote oxidation reactions with photogenerated holes. A ternary nanocomposite photoanode consisting of TiO_2 nanoparticles, Dawson-type POM $[P_2W_{18}O_{62}]^{6-}$ and Cu quantum dots has been fabricated to perform the photoelectrocatalytic oxidation of formic acid. However, anodic photocurrents in the μA range were measured revealing poor catalytic performance which can be probably explained by unefficient charge transfer processes between the three components. In another recent report, an organic lead halide perovskite (bandgap of 1.5 eV,[289] see Figure 10) photoanode was judiciously modified with dual POMs, namely $[PW_{12}O_{40}]^{3-}$ and $[Ag_{10}[Co(H_2O)_{32}\{CoBi_2W_{19}O_{66}(OH)_4\}]$, both to improve the quality of the perovskite film and facilitate transfer of photogenerated holes.[290] By effectively reducing the photogenerated charge carrier recombination, the photoelectrocatalytic efficiency for the oxidation of benzene into phenol was obviously boosted. Compared with a pure perovskite photoanode, the modified photoanode showed 2.6-fold higher photocurrent densities and a significantly increased conversion yield (32% vs. 26%) (see Figure 21).

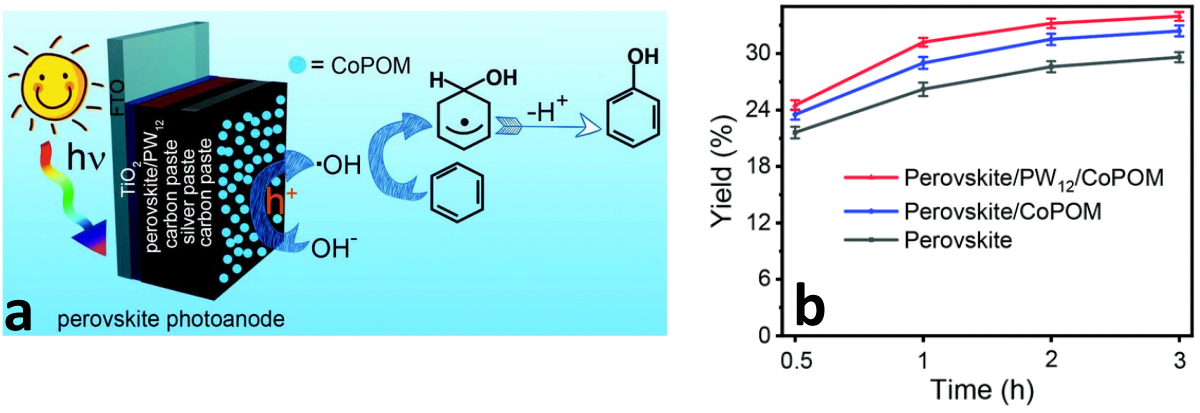

Figure 21. Perovskite photoanode modified with dual POMs, $[PW_{12}O_{40}]^{3-}$ (PW_{12}) and $[Ag_{10}[\{Co(H_2O)_3\}_2\{CoBi_2W_{19}O_{66}(OH)_4\}]$ (CoPOM), for the photoelectrocatalytic oxidation of benzene

to phenol (a). Yield of benzene oxidation to phenol for diversely modified perovskite photoanodes (b). Conditions: 1M KOH with 0.1 mM benzene, 0.96 V *vs* RHE under 100 mW cm^{-2} illumination. Adapted with permission from ref 290. Copyright 2020 Royal Society of Chemistry.

Apart from the two aforementioned examples, all the other recent studies dealt with POM-modified photoanodes for sunlight-driven OER. As a matter of fact, it is anticipated that the selected SCs efficiently transfer photogenerated holes from their valence band which is well positioned relatively to the O_2/H_2O redox potential for OER (see Figure 10). In the report published by C. L. Hill and co-workers, a Earth-abundant and cost-effective hematite α-Fe_2O_3 photoanode (bandgap of 2.0-2.2 eV,[287] see Figure 10) was decorated with $[Ru^{IV}_4(OH)_2(H_2O)_4(\gamma\text{-}SiW_{10}O_{34})_2]^{10-}$ and then protected by an optimized 4 nm-thick Al_2O_3 stabilizing layer.[291] Thanks to this protecting layer, the POM-modified photoanode was able to sustain the photoelectrochemical production of O_2 at 1.24 V *vs* RHE in aqueous solution pH = 8.3 with nearly 100% Faradaic yield and a stability in operation >12 h which is much greater than that of an unfunctionalized photoanode. In another study, semiconducting photoanodes consisting of TiO_2 nanoparticles and electrostatically immobilized tetra-ruthenium POMs ($[Ru^{IV}_4O_5(OH)(H_2O)_4(\gamma\text{-}PW_{10}O_{36})_2]^{9-}$ and $[Ru^{IV}_4(OH)_2(H_2O)_4(\gamma\text{-}SiW_{10}O_{34})_2]^{10-}$) have been prepared and operated UV light-driven OER with photocurrent densities of 1.2 mA cm^{-2} at 1.5 V *vs* RHE and pH = 10.[292] Even though POMs and the Al_2O_3 layer enabled the photoanode stability to be increased, the delivered photocurrent was however too low for practical applications. Such a situation is common for a large bandgap metal oxide semiconductor like TiO_2 that is able to absorb only the UV range of the solar spectrum thus resulting in a low energy conversion efficiency.[293]

Besides binary metal oxides, there is also some examples of POM-modified photoanodes using the ternary oxide $BiVO_4$ as the electrode material. This SC has emerged as one of the most promising materials for photoelectrochemical water splitting because of its suitable bandgap of 2.4 eV and its very favorable conduction band position allowing it to theoretically

achieve more than 1 V of photovoltage for water oxidation.[287,294] In the first example, a $BiVO_4$ photoanode modified with Keggin-type POMs ($[PW_{12}O_{40}]^{3-}$ or $[CoW_{12}O_{40}]^{6-}$) was prepared. Nevertheless, such assemblies exhibited poor photoelectrocatalytic performance with disappointingly low photocurrent densities of 0.2 mA cm^{-2} at about 1.8 V *vs* RHE in sulfate solution (pH = 5.9).[295] Better performance was reported for a $BiVO_4$ photoanode modified with an anionic Co-containing Weakley-type POM $[Co_4(H_2O)_2(VW_9O_{34})_2]^{10-}$ electrostatically entrapped into a cationic polyethyleneimine multilayer.[286] Indeed, such a photoanode working at pH = 7, showed an onset potential for OER of 0.24 V *vs* RHE and a photocurrent density of 2.3 mA cm^{-2} at 1.23 V *vs* RHE. The beneficial effect of the immobilized POM was clearly evidenced by a ca. 400 mV cathodic shift of the onset potential and a three-fold higher photocurrent relative to the pristine $BiVO_4$ photoanode. Based on the significant photoelectrocatalytic activity of the individual $[Ni_4(H_2O)_2(PW_9O_{34})_2]^{10-}$ -modified Cu_2O photocathode and $[Co_4(H_2O)_2(VW_9O_{34})_2]^{10-}$ -modified $BiVO_4$ photoanode for sunlight-driven HER and OER, respectively, a bias-free photoelectrochemical cell for overall solar water splitting has been fabricated.[286] Despite a low operating current of 0.2 mA cm^{-2} and a limited stability (~2 h), this demonstrator constitutes the only and promising achievement of a complete photoelectrochemical cell incorporating POMs in both photocathode and photoanode.

In addition to metal oxide semiconductors, a recent exploratory study has focused on the potential of graphitic carbon nitride (g-C_3N_4) as POM-integrating composite material. This SC has received a tremendous attention due to its intrinsic fascinating properties, such as moderate bandgap (~2.7 eV), nontoxicity, low cost, good stability, and easy preparation.[296] However, the photo(electro)catalytic performance of g-C_3N_4 is limited by the high recombination rate of its photogenerated charge carriers and its weak light absorption. Therefore, the combination of POMs with g-C_3N_4 could reduce some of the intrinsic drawbacks of g-C_3N_4. To examine this aspect, g-C_3N_4 was combined with an anionic Preyssler-type POM $[NaP_5W_{30}O_{110}]^{14-}$ and the so

formed composite was then deposited on an optically transparent fluorine-doped SnO_2 (FTO) electrode.[297] The presence of the POM was obviously beneficial for the photoelectrocatalytic OER activity of the photoanode. Compared with pristine g-C_3N_4, higher photocurrent densities were measured at 1.23 V *vs* RHE in sulfate solution at pH = 6.4 (44 *vs* 18 µA cm^{-2}) and the photoconversion efficiency was 3.45 times greater. Overall, these modest performance metrics are however encouraging and can be improved by optimizing the g-C_3N_4/POM composite formulation and engineering the interface with the electrode material.

6. Conclusions and Outlook

The transposition of homogeneous electrocatalysis to (photo)electrode-supported electrocatalysis using POMs and its derivatives constitutes a really promising avenue toward the development of modern electrochemical devices, which could be of high interest for applications in chemical sensing, biosensing, electroanalysis and solar-driven fuel cells. Overall, considerable efforts have been paid by researchers to decrease the kinetic limitations and improve both chemical and electrochemical stabilities of the immobilized POM assemblies, in order to produce catalytically effective and robust POMs-modified (photo)electrodes. Numerous immobilization platforms, such as MOFs, carbon nanomaterials and metal nanostructures, have been used with the aim of (*i*) strongly attaching POMs onto semiconducting and conducting electrodes, (*ii*) increasing the electron conductivity in the POM-incorporating film, (*iii*) enhancing the electron transfer across the film to the electrode surface, and (*iv*) controlling the structural organization of the POM-incorporating assembly or the three-dimensional distribution of the immobilized POM. It is obvious that achieving all of these goals is nowadays still challenging.

It must be also emphasized that the majority of POMs attached to (photo)electrode surfaces pertains the family of Keggin-, Dawson-type structures, their lacunary and metal-substituted

derivatives. Although these basic structures are appealing for building robust and effective catalytic electrodes, they suffer sometimes from non-optimal electron/proton-collecting properties and/or fail often to promote electrocatalytic reactions with high selectivity. As a representative example, a POM-modified electrode which delivers both high electrocatalytic current density (> 10 mA cm^{-2}) and is highly selective for the multi-electron and multi-proton reduction of CO_2 has still to be discovered. In that context, the elaboration of modified electrodes from engineered and structurally complex POMs, such as giant POMs, shown in Figure 1 (Keplerates, 3d metal containing macrocyclic cryptates…), and cluster-POMs as well, could pave the way towards innovative and multifunctional catalytic systems with improved redox properties. Unfortunately, the attachment of such sophisticated structures to electrodes has been either scarcely or not explored at all. It is also worth mentioning the chaotropic properties of POMs have not been exploited so far for the building of electrodes functionalized with hierarchical multi-component POM-based architectures. Overall, these facts raise the question of the obvious lack of interactions and knowledge sharing between the communities of molecular chemists and surface/interface physicochemists. It is therefore highly desirable that these communities meet together in the future to propose breakthrough molecular engineering POMs allowing, amongst others, the selectivity of the electrocatalytic reaction to be controlled and to reach outstanding performance metrics (in terms of stability in operation, current density and overpotential) and high sensitivity when an electrochemical detection is targeted.

Importantly, compared with the large number of examples devoted to POMs-modified conducting electrodes, the immobilization of POMs on semiconducting surfaces has been much less studied. This thematic area is clearly under-explored, and the few promising studies aimed at integrating POM electrocatalysts into different semiconductors should prompt other research groups to pursue this route toward novel modified photoelectrodes. Let us recall here that the

key difference between photoactive semiconducting photoelectrodes and non-photoactive working electrodes traditionally used for electrocatalytic applications (e.g., metals, carbon) is that for the semiconductors, light serves as an important source of energy input. Such a property based on photovoltaic conversion can achieve an energy-saving route to electrochemical catalysis. Therefore, the production of solar fuels other than H_2, such as CO_2 reduction products (e.g. CO and CH_4) and ammonia, from POMs attached to photocathodes merits exploration. It is also noteworthy that the photoelectrocatalytic oxidation of water and some organics from POMs-modified photoanodes requires effective and convenient engineering and protection strategies to avoid the so-called photocorrosion phenomenon of the semiconductor (particularly prominent for low bandgap semiconductors, such as silicon) and its oxidation under anodic polarization which result in disappointingly low current densities and poor stability of the photoanode in operation. Interestingly, the thoughtful mix between the photocatalytic activity of some POMs with the photoactivity of SCs could yield particularly innovative modified photoelectrodes which could find applications in photoelectrochemistry and in the design of light-addressable or switchable devices.

References

(1) Long, D.-L.; Tsunashima, R.; Cronin, L. Polyoxometalates: Building Blocks for Functional Nanoscale Systems. *Angew. Chem. Int. Ed.* **2010**, *49* (10), 1736–1758.

(2) Wang, S.-S.; Yang, G.-Y. Recent Advances in Polyoxometalate-Catalyzed Reactions. *Chem. Rev.* **2015**, *115* (11), 4893–4962.

(3) Gumerova, N. I.; Rompel, A. Synthesis, Structures and Applications of Electron-Rich Polyoxometalates. *Nat. Rev. Chem.* **2018**, *2* (2), 0112.

(4) López, X.; Carbó, J. J.; Bo, C.; Poblet, J. M. Structure, Properties and Reactivity of Polyoxometalates: A Theoretical Perspective. *Chem. Soc. Rev.* **2012**, *41* (22), 7537.

(5) Proust, A.; Thouvenot, R.; Gouzerh, P. Functionalization of Polyoxometalates: Towards Advanced Applications in Catalysis and Materials Science. *Chem. Commun.* **2008**, No. 16, 1837–1852.

(6) Li, N.; Liu, J.; Dong, B.; Lan, Y. Polyoxometalate-Based Compounds for Photo- and Electrocatalytic Applications. *Angew. Chem. Int. Ed.* **2020**, *59* (47), 20779–20793.

(7) Walsh, J. J.; Bond, A. M.; Forster, R. J.; Keyes, T. E. Hybrid Polyoxometalate Materials for Photo(Electro-) Chemical Applications. *Coord. Chem. Rev.* **2016**, *306*, 217–234.

(8) Ueda, T. Electrochemistry of Polyoxometalates: From Fundamental Aspects to Applications. *ChemElectroChem* **2018**, *5* (6), 823–838.

(9) Horn, M. R.; Singh, A.; Alomari, S.; Goberna-Ferrón, S.; Benages-Vilau, R.; Chodankar, N.; Motta, N.; Ostrikov, K. (Ken); MacLeod, J.; Sonar, P.; Gomez-Romero, P.; Dubal, D. Polyoxometalates (POMs): From Electroactive Clusters to Energy Materials. *Energy Environ. Sci.* **2021**, *14* (4), 1652–1700.

(10) Vazylyev, M.; Sloboda-Rozner, D.; Haimov, A.; Maayan, G.; Neumann, R. Strategies for Oxidation Catalyzed by Polyoxometalates at the Interface of Homogeneous and Heterogeneous Catalysis. *Top. Catal.* **2005**, *34* (1–4), 93–99.

(11) Pope, M. *Heteropoly and Isopoly Oxometalates*; Inorganic Chemistry Concepts; Springer-Verlag: Berlin Heidelberg, 1983.

(12) Pope, M. T. Heteropoly and Isopoly Anions as Oxo Complexes and Their Reducibility to Mixed-Valence Blues. *Inorg. Chem.* **1972**, *11* (8), 1973–1974.

(13) Yin, Q.; Tan, J. M.; Besson, C.; Geletii, Y. V.; Musaev, D. G.; Kuznetsov, A. E.; Luo, Z.; Hardcastle, K. I.; Hill, C. L. A Fast Soluble Carbon-Free Molecular Water Oxidation Catalyst Based on Abundant Metals. *Science* **2010**, *328* (5976), 342–345.

(14) Lv, H.; Guo, W.; Wu, K.; Chen, Z.; Bacsa, J.; Musaev, D. G.; Geletii, Y. V.; Lauinger, S. M.; Lian, T.; Hill, C. L. A Noble-Metal-Free, Tetra-Nickel Polyoxotungstate Catalyst for Efficient Photocatalytic Hydrogen Evolution. *J. Am. Chem. Soc.* **2014**, *136* (40), 14015–14018.

(15) Sartorel, A.; Carraro, M.; Scorrano, G.; Zorzi, R. D.; Geremia, S.; McDaniel, N. D.; Bernhard, S.; Bonchio, M. Polyoxometalate Embedding of a Tetraruthenium(IV)-Oxo-Core by Template-Directed Metalation of $[\gamma\text{-}SiW_{10}O_{36}]^{8-}$: A Totally Inorganic Oxygen-Evolving Catalyst. *J. Am. Chem. Soc.* **2008**, *130* (15), 5006–5007.

(16) Blasco-Ahicart, M.; Soriano-López, J.; Carbó, J. J.; Poblet, J. M.; Galan-Mascaros, J. R. Polyoxometalate Electrocatalysts Based on Earth-Abundant Metals for Efficient Water Oxidation in Acidic Media. *Nat. Chem.* **2018**, *10* (1), 24–30.

(17) Martin-Sabi, M.; Soriano-López, J.; Winter, R. S.; Chen, J.-J.; Vilà-Nadal, L.; Long, D.-L.; Galán-Mascarós, J. R.; Cronin, L. Redox Tuning the Weakley-Type Polyoxometalate Archetype for the Oxygen Evolution Reaction. *Nat. Catal.* **2018**, *1* (3), 208–213.

(18) Müller, A.; Gouzerh, P. From Linking of Metal-Oxide Building Blocks in a Dynamic Library to Giant Clusters with Unique Properties and towards Adaptive Chemistry. *Chem. Soc. Rev.* **2012**, *41* (22), 7431–7463.

(19) Müller, A.; Krickemeyer, E.; Penk, M.; Rohlfing, R.; Armatage, A.; Bögge, H. Template-Controlled Formation of Cluster Shells or a Type of Molecular Recognition: Synthesis of $[HV_{22}O_{54}(ClO_4)]^{6-}$ and $[H_2V_{18}O_{44}(N_3)]^{5-}$. *Angew. Chem. Int. Ed. Engl.* **1991**, *30* (12), 1674–1677.

(20) Yu. Monakhov, K.; Linnenberg, O.; Kozłowski, P.; van Leusen, J.; Besson, C.; Secker, T.; Ellern, A.; López, X.; Poblet, J. M.; Kögerler, P. Supramolecular Recognition Influences Magnetism in $[X@HV^{IV}_{8}V^{V}_{14}O_{54}]^{6-}$ Self-Assemblies with Symmetry-Breaking Guest Anions. *Chem. – Eur. J.* **2015**, *21* (6), 2387–2397.

(21) Linnenberg, O.; Moors, M.; Solé-Daura, A.; López, X.; Bäumer, C.; Kentzinger, E.; Pyckhout-Hintzen, W.; Monakhov, K. Yu. Molecular Characteristics of a Mixed-Valence Polyoxovanadate $\{V^{IV/V}_{18}O_{42}\}$ in Solution and at the Liquid–Surface Interface. *J. Phys. Chem. C* **2017**, *121* (19), 10419–10429.

(22) Greiner, S.; Schwarz, B.; Ringenberg, M.; Dürr, M.; Ivanovic-Burmazovic, I.; Fichtner, M.; Anjass, M.; Streb, C. Redox-Inactive Ions Control the Redox-Activity of Molecular Vanadium Oxides. *Chem. Sci.* **2020**, *11* (17), 4450–4455.

(23) Bamba, I.; Falaise, C.; Marrot, J.; Gbassi, G.; Atheba, P.; Guillot, R.; Haouas, M.; Cadot, E. Revisiting the Three-Vanadium Sandwich Type Polyoxometalates: Structures, Solution Behavior and Redox Properties. *Inorg Chem.* **2022** *accepted*

(24) Sadakane, M.; Steckhan, E. Electrochemical Properties of Polyoxometalates as Electrocatalysts. *Chem. Rev.* **1998**, *98* (1), 219–238.

(25) Ueda, T. Electrochemistry of Polyoxometalates: From Fundamental Aspects to Applications. *ChemElectroChem* **2018**, *5* (6), 823–838.

(26) Altenau, J. J.; Pope, M. T.; Prados, R. A.; So, Hyunsoo. Models for Heteropoly Blues. Degrees of Valence Trapping in Vanadium(IV)- and Molybdenum(V)-Substituted Keggin Anions. *Inorg. Chem.* **1975**, *14* (2), 417–421.

(27) Chiang, M.-H.; Antonio, M. R.; Soderholm, L. Energetics of the Preyssler Anion's Molecular Orbitals: Quantifying the Effect of the Encapsulated-Cation's Charge. *Dalton Trans.* **2004**, No. 21, 3562–3567.

(28) Fernández, J. A.; López, X.; Bo, C.; de Graaf, C.; Baerends, E. J.; Poblet, J. M. Polyoxometalates with Internal Cavities: Redox Activity, Basicity, and Cation Encapsulation in $[X^{n+}P_5W_{30}O_{110}]^{(15-n)-}$ Preyssler Complexes, with X = Na^+, Ca^{2+}, Y^{3+}, La^{3+}, Ce^{3+}, and Th^{4+}. *J. Am. Chem. Soc.* **2007**, *129* (40), 12244–12253.

(29) Alizadeh, M. H.; Harmalker, S. P.; Jeannin, Y.; Martin-Frere, J.; Pope, M. T. A Heteropolyanion with Fivefold Molecular Symmetry That Contains a Nonlabile Encapsulated Sodium Ion. The Structure and Chemistry of $[NaP_5W_{30}O_{110}]^{14-}$. *J. Am. Chem. Soc.* **1985**, *107* (9), 2662–2669.

(30) Mbomekallé, I.-M.; López, X.; Poblet, J. M.; Sécheresse, F.; Keita, B.; Nadjo, L. Influence of the Heteroatom Size on the Redox Potentials of Selected Polyoxoanions. *Inorg. Chem.* **2010**, *49* (15), 7001–7006.

(31) Domaille, P. J.; Watunya, G. Synthesis and Tungsten-183 NMR Characterization of Vanadium-Substituted Polyoxometalates Based on B-Type Tungstophosphate $PW_9O_{34}^{9-}$ Precursors. *Inorg. Chem.* **1986**, *25* (8), 1239–1242.

(32) Cadot, E.; Thouvenot, R.; Teze, A.; Herve, G. Syntheses and Multinuclear NMR Characterizations of .Alpha.-$[SiMo_2W_9O_{39}]^{8-}$ and .Alpha.-$[SiMo_{3-X}V_xW_9O_{40}]^{(4+x)-}$ (x = 1, 2) Heteropolyoxometalates. *Inorg. Chem.* **1992**, *31* (20), 4128–4133.

(33) Sanchez, C.; Livage, J.; Launay, J. P.; Fournier, M.; Jeannin, Y. Electron Delocalization in Mixed-Valence Molybdenum Polyanions. *J. Am. Chem. Soc.* **1982**, *104* (11), 3194–3202.

(34) Contant, R.; Ciabrini, J.-P. Stereospecific Preparations of New N-Molybdo-(18-n)-Tungsto-2-Phosphates and Related "Defect" Compounds (n = 2, 4 or 5). *J. Inorg. Nucl. Chem.* **1981**, *43* (7), 1525–1528.

(35) Massart, R. Premiers Stades de Réduction de l'acide Silicomolybdique. *Ann. Chim.* **1969**, *4*, 365.

(36) Souchay, P.; Hervé, G. Etude de La Réduction de l'acide Silico-12-Tungstique. *C. R. Acad. Sc. Paris* **1965**, No. 261, 2486.

(37) Hervé, G. Etude de La Réduction de l'acide Silico-Tungstique En Milieu Alcalin. *C. R. Acad. Sc. Paris* **1966**, *263*, 413.

(38) Keita, B.; Bouaziz, D.; Nadjo, L. Solvent Effects on the Redox Potentials of Potassium 12-Tungstosilicate and 18-Tungstodiphosphate. *J. Electrochem. Soc.* **1988**, *135* (1), 87.

(39) Ueda, T.; Kodani, K.; Ota, H.; Shiro, M.; Guo, S.-X.; Boas, J. F.; Bond, A. M. Voltammetric and Spectroscopic Studies of α- and β-$[PW_{12}O_{40}]^{3-}$ Polyoxometalates in Neutral and Acidic Media: Structural Characterization as Their $[(n\text{-}Bu_4N)_3][PW_{12}O_{40}]$ Salts. *Inorg. Chem.* **2017**, *56* (7), 3990–4001.

(40) Eda, K.; Osakai, T. How Can Multielectron Transfer Be Realized? A Case Study with Keggin-Type Polyoxometalates in Acetonitrile. *Inorg. Chem.* **2015**, *54* (6), 2793–2801.

(41) Himeno, S.; Takamoto, M.; Ueda, T. Cation Effects on the Voltammetric Behavior of α-Keggin-Type $[SiMo_{12}O_{40}]^{4-}$ and $[PMo_{12}O_{40}]^{3-}$ Complexes in CH_3COCH_3 and CH_3CN. *J. Electroanal. Chem.* **2000**, *485* (1), 49–54.

(42) Konishi, T.; Kodani, K.; Hasegawa, T.; Ogo, S.; Guo, S.-X.; Boas, J. F.; Zhang, J.; Bond, A. M.; Ueda, T. Impact of the Lithium Cation on the Voltammetry and Spectroscopy of $[XVM_{11}O_{40}]^{n-}$ (X = P, As (n = 4), S (n = 3); M = Mo, W): Influence of Charge and Addenda and Hetero Atoms. *Inorg. Chem.* **2020**, *59* (15), 10522–10531.

(43) Grigoriev, V. A.; Hill, C. L.; Weinstock, I. A. Role of Cation Size in the Energy of Electron Transfer to 1:1 Polyoxometalate Ion Pairs $\{(M^+)(X^{n+}VW_{11}O_{40})\}^{(8-n)-}$ (M = Li, Na, K). *J. Am. Chem. Soc.* **2000**, *122* (14), 3544–3545.

(44) Yao, S.; Falaise, C.; Ivanov, A. A.; Leclerc, N.; Hohenschutz, M.; Haouas, M.; Landy, D.; Shestopalov, M. A.; Bauduin, P.; Cadot, E. Hofmeister Effect in the Keggin-Type Polyoxotungstate Series. *Inorg. Chem. Front.* **2021**, *8* (1), 12–25.

(45) Yao, S.; Falaise, C.; Khlifi, S.; Leclerc, N.; Haouas, M.; Landy, D.; Cadot, E. Redox-Responsive Host–Guest Association between γ-Cyclodextrin and Mixed-Metal Keggin-Type Polyoxometalates. *Inorg. Chem.* **2021**, *60* (10), 7433–7441.

(46) Robin, M. B.; Day, P. Mixed Valence Chemistry-A Survey and Classification. In *Advances in Inorganic Chemistry and Radiochemistry*; Emeléus, H. J., Sharpe, A. G., Eds.; Academic Press, 1968; Vol. 10, pp 247–422.

(47) Papaconstantinou, E.; Pope, M. T. Heteropoly Blues. V. Electronic Spectra of One- to Six-Electron Blues of 18-Metallodiphosphate Anions. *Inorg. Chem.* **1970**, *9* (3), 667–669.

(48) Varga, G. M.; Papaconstantinou, E.; Pope, M. T. Heteropoly Blues. IV. Spectroscopic and Magnetic Properties of Some Reduced Polytungstates. *Inorg. Chem.* **1970**, *9* (3), 662–667.

(49) Prados, R. A.; Pope, M. T. Low-Temperature Electron Spin Resonance Spectra of Heteropoly Blues Derived from Some 1:12 and 2:18 Molybdates and Tungstates. *Inorg. Chem.* **1976**, *15* (10), 2547–2553.

(50) Sanchez, C.; Livage, J.; Launay, J. P.; Fournier, M. Electron Delocalization in Mixed-Valence Tungsten Polyanions. *J. Am. Chem. Soc.* **1983**, *105* (23), 6817–6823.

(51) Kozik, Mariusz.; Hammer, C. F.; Baker, L. C. W. Direct Determination by Tungsten-183 NMR of the Locations of Added Electrons in ESR-Silent Heteropoly Blues. Chemical Shifts and Relaxation Times in Polysite Mixed-Valence Transition Metal Species. *J. Am. Chem. Soc.* **1986**, *108* (10), 2748–2749.

(52) Duncan, D. C.; Hill, C. L. Synthesis and Characterization of the Mixed-Valence Diamagnetic Two-Electron-Reduced Isopolytungstate $[W_{10}O_{32}]^{6-}$. Evidence for an Asymmetric d-Electron Distribution over the Tungsten Sites. *Inorg. Chem.* **1996**, *35* (20), 5828–5835.

(53) Clemente-Juan, J. M.; Coronado, E.; Gaita-Ariño, A.; Suaud, N. Mixed-Valence Polyoxometalates: Spin-Coupling and Electron Distribution in the Decawolframate Anion Reduced by Two Electrons. *J. Phys. Chem. A* **2007**, *111* (39), 9969–9977.

(54) Borrás-Almenar, J. J.; Clemente, J. M.; Coronado, E.; Tsukerblat, B. S. Mixed-Valence Polyoxometalate Clusters. I. Delocalization of Electronic Pairs in Dodecanuclear Heteropoly Blues with Keggin Structure. *Chem. Phys.* **1995**, *195* (1), 1–15.

(55) Borrás-Almenar, J. J.; Clemente, J. M.; Coronado, E.; Tsukerblat, B. S. Mixed-Valence Polyoxometalate Clusters. II. Delocalization of Electronic Pairs in 18-Site Heteropoly Blues with Wells-Dawson Structure. *Chem. Phys.* **1995**, *195* (1), 17–28.

(56) Casan-Pastor, N.; Baker, L. C. W. Magnetic Properties of Mixed-Valence Heteropoly Blues. Interactions within Complexes Containing Paramagnetic Atoms in Various Sites as Well as "Blue" Electrons Delocalized over Polytungstate Frameworks. *J. Am. Chem. Soc.* **1992**, *114* (26), 10384–10394.

(57) Kozik, Mariusz.; Casan-Pastor, Nieves.; Hammer, C. F.; Baker, L. C. W. Ring Currents in Wholly Inorganic Heteropoly Blue Complexes. Evaluation by a Modification of Evans' Susceptibility Method. *J. Am. Chem. Soc.* **1988**, *110* (23), 7697–7701.

(58) Suaud, N.; Gaita-Ariño, A.; Clemente-Juan, J. M.; Sánchez-Marín, J.; Coronado, E. Electron Delocalization in Mixed-Valence Keggin Polyoxometalates. Ab Initio Calculation of the Local Effective Transfer Integrals and Its Consequences on the Spin Coupling. *J. Am. Chem. Soc.* **2002**, *124* (50), 15134–15140.

(59) Suaud, N.; Gaita-Ariño, A.; Clemente-Juan, J. M.; Coronado, E. Electron Delocalization and Electrostatic Repulsion at the Origin of the Strong Spin Coupling in Mixed-Valence Keggin Polyoxometalates: Ab Initio Calculations of the One- and Two-Electron Processes. *Chem. – Eur. J.* **2004**, *10* (16), 4041–4053.

(60) Cadot, E.; Fournier, M.; Tézé, A.; Hervé, G. Electrochemical Properties and ESR Characterization of Mixed Valence α-$[XMo_{3-X}V_xW_9O_{40}]^{n-}$ Heteropolyanions with X = PV and SiIV, x = 1, 2, or 3. *Inorg. Chem.* **1996**, *35* (2), 282–288.

(61) Geletii, Y. V.; Hill, C. L.; Bailey, A. J.; Hardcastle, K. I.; Atalla, R. H.; Weinstock, I. A. Electron Exchange between α-Keggin Tungstoaluminates and a Well-Defined Cluster-Anion Probe for Studies in Electron Transfer. *Inorg. Chem.* **2005**, *44* (24), 8955–8966.

(62) Kozik, M.; Baker, L. C. W. Electron Exchange Reactions between Heteropoly Anions: Comparison of Experimental Rate Constants with Theoretically Predicted Values. *J. Am. Chem. Soc.* **1990**, *112* (21), 7604–7611.

(63) Kozik, Mariusz.; Hammer, C. F.; Baker, L. C. W. NMR of Phosphorus-31 Heteroatoms in Paramagnetic 1-Electron Heteropoly Blues. Rates of Intra- and Intercomplex Electron Transfers. Factors Affecting Line Widths. *J. Am. Chem. Soc.* **1986**, *108* (24), 7627–7630.

(64) Sutin, N. Nuclear, Electronic, and Frequency Factors in Electron Transfer Reactions. *Acc. Chem. Res.* **1982**, *15* (9), 275–282.

(65) Tsunashima, R.; Nakamura, I.; Oue, R.; Koga, S.; Oki, H.; Noro, S.; Nakamura, T.; Akutagawa, T. Inter-Cluster Distance Dependence of Electrical Properties in Single Crystals of a Mixed-Valence Polyoxometalate. *Dalton Trans.* **2017**, *46* (37), 12619–12624.

(66) Chen, L.; San, K. A.; Turo, M. J.; Gembicky, M.; Fereidouni, S.; Kalaj, M.; Schimpf, A. M. Tunable Metal Oxide Frameworks via Coordination Assembly of Preyssler-Type Molecular Clusters. *J. Am. Chem. Soc.* **2019**, *141* (51), 20261–20268.

(67) Turo, M. J.; Chen, L.; Moore, C. E.; Schimpf, A. M. Co2+-Linked $[NaP_5W_{30}O_{110}]^{14-}$: A Redox-Active Metal Oxide Framework with High Electron Density. *J. Am. Chem. Soc.* **2019**, *141* (11), 4553–4557.

(68) Tsunashima, R.; Iwamoto, Y.; Baba, Y.; Kato, C.; Ichihashi, K.; Nishihara, S.; Inoue, K.; Ishiguro, K.; Song, Y.-F.; Akutagawa, T. Electrical Network of Single-Crystalline Metal Oxide Nanoclusters Wired by π-Molecules. *Angew. Chem. Int. Ed.* **2014**, *53* (42), 11228–11231.

(69) Souchay, P.; Launay, J. P. Réduction de l'ion Métatungstique Jusqu'au Stade à Six Électrons. *C. R. Acad. Sc. Paris* **1969**, *268*, 1354.

(70) Launay, J. P.; Massart, R.; Souchay, P. Gradual Reduction of Molybdosilicates and Related Compounds. *J. Common Met.* **1974**, *36* (1), 139–150.

(71) Launay, J. P. Reduction de l'ion métatungstate: Stades élevés de réduction de $H_2W_{12}O_{40}^{6-}$, dérivés de l'ion $HW_{12}O_{40}^{7-}$ et discussion générale. *J. Inorg. Nucl. Chem.* **1976**, *38* (4), 807–816.

(72) Launay, J. P. Mécanisme de La Réduction de l'ion Métatungstique Au Delà Du Stade à 6électrons. *C R Acad Sc* **1969**, No. 269, 971.

(73) Hervé, G. Stade de Réduction Élevés de l'ion 12-Tungstosilicate. *Ann Chim* **1971**, No. 5, 287–296.

(74) Hervé, G. Premiers Stades de Réduction de l'ion 12-Tungstosilicate. *Ann Chim* **1971**, *6*, 219.

(75) Contant, R.; Fruchart, J.-M.; Hervé, G.; Massart, R. Etude de La Reduction de l'ion 12-Tungstoborate. *C. R. Acad. Sc. Paris* **1970**, No. 270, 1952.

(76) Fruchart, J.-M.; Hervé, G. Réduction de Ions 12-Tunsgtophosphate et 12-Tungstoborate. *Ann. Chim* **1971**, *6*, 337.

(77) Chen, J.-J.; Symes, M. D.; Cronin, L. Highly Reduced and Protonated Aqueous Solutions of $[P_2W_{18}O_{62}]^{6-}$ for on-Demand Hydrogen Generation and Energy Storage. *Nat. Chem.* **2018**, *10* (10), 1042–1047.

(78) Jeannin, Y.; Launay, J. P.; Sedjadi, M. A. S. Crystal and Molecular Structure of the Six-Electron-Reduced Form of Metatungstate $Rb_4H_8[H_2W_{12}O_{40}]$..Apprx.$18H_2O$: Occurrence of a Metal-Metal Bonded Subcluster in a Heteropolyanion Framework. *Inorg. Chem.* **1980**, *19* (10), 2933–2935.

(79) Yamase, T.; Ishikawa, E. Structural Characterization of the Brown Six-Electron-Reduced Form of Dodecatungstoborate, $K_5[BW_{12}O_{37}(H_2O)_3]\cdot 13.5H2O$. *J. Chem. Soc. Dalton Trans.* **1996**, No. 8, 1619–1627.

(80) Piepgrass, K.; Pope, M. T. Heteropoly "Brown" as Class I Mixed Valence (W(IV,VI)) Complexes. Tungsten-183 NMR of W(IV) Trimers. *J. Am. Chem. Soc.* **1987**, *109* (5), 1586–1587.

(81) Boskovic, C.; Sadek, M.; Brownlee, R. T. C.; Bond, A. M.; Wedd, A. G. Electrosynthesis and Solution Structure of Six-Electron Reduced Forms of Metatungstate, $[H_2W_{12}O_{40}]^{6-}$. *J. Chem. Soc. Dalton Trans.* **2001**, No. 2, 187–196.

(82) Cotton, F. A. Metal Atom Clusters in Oxide Systems. *Inorg. Chem.* **1964**, *3* (9), 1217–1220.

(83) Smith, S. P. E.; Christian, J. B. Mechanism of the Coupled 24-Electron Reduction and Transformations among the "Blues", the "Browns" and the "Reds" of Ammonium Metatungstate. *Electrochim. Acta* **2008**, *53* (6), 2994–3001.

(84) Müller, A.; Das, S. K.; Fedin, V. P.; Krickemeyer, E.; Beugholt, C.; Bögge, H.; Schmidtmann, M.; Hauptfleisch, B. Rapid and Simple Isolation of the Crystalline Molybdenum-Blue Compounds with Discrete and Linked Nanosized Ring-Shaped Anions: $Na_{15}[Mo_{154}O_{462}H_{14}(H_2O)_{70}]_{0.5}[Mo_{152}O_{457}H_{14}(H_2O)_{68}]_{0.5}\cdot$ca.400 H_2O and $Na_{22}[Mo_{142}O_{442}H_{14}(H_2O)_{58}]\cdot$ ca. 250 H_2O. *Z. Für Anorg. Allg. Chem.* **1999**, *625* (7), 1187–1192.

(85) Müller, A.; Shah, S. Q. N.; Bögge, H.; Schmidtmann, M. Molecular Growth from a Mo_{176} to a Mo_{248} Cluster. *Nature* **1999**, *397* (6714), 48–50.

(86) Garrido Ribó, E.; Bell, N. L.; Xuan, W.; Luo, J.; Long, D.-L.; Liu, T.; Cronin, L. Synthesis, Assembly, and Sizing of Neutral, Lanthanide Substituted Molybdenum Blue Wheels $\{Mo_{90}Ln_{10}\}$. *J. Am. Chem. Soc.* **2020**, *142* (41), 17508–17514.

(87) Falaise, C.; Khlifi, S.; Bauduin, P.; Schmid, P.; Shepard, W.; Ivanov, A. A.; Sokolov, M. N.; Shestopalov, M. A.; Abramov, P. A.; Cordier, S.; Marrot, J.; Haouas, M.; Cadot, E. "Host in Host" Supramolecular Core–Shell Type Systems Based on Giant Ring-Shaped Polyoxometalates. *Angew. Chem. Int. Ed.* **2021**, *60* (25), 14146–14153.

(88) Katsoulis, D. E.; Pope, M. T. New Chemistry for Heteropolyanions in Anhydrous Nonpolar Solvents. Coordinative Unsaturation of Surface Atoms. Polyanion Oxygen Carriers. *J. Am. Chem. Soc.* **1984**, *106* (9), 2737–2738.

(89) Liu, J.; Ortéga, F.; Sethuraman, P.; Katsoulis, D. E.; Costello, C. E.; Pope, M. T. Trimetallo Derivatives of Lacunary 9-Tungstosilicate Heteropolyanions. Part 1. Synthesis and Charaterization. *J. Chem. Soc. Dalton Trans.* **1992**, No. 12, 1901–1906.

(90) Mizuno, N.; Nozaki, C.; Kiyoto, I.; Misono, M. Highly Efficient Utilization of Hydrogen Peroxide for Selective Oxygenation of Alkanes Catalyzed by Diiron-Substituted Polyoxometalate Precursor. *J. Am. Chem. Soc.* **1998**, *120* (36), 9267–9272.

(91) Anderson, T. M.; Neiwert, W. A.; Hardcastle, K. I.; Hill, C. L. Multi-Iron Silicotungstates: Synthesis, Characterization, and Stability Studies of Polyoxometalate Dimers. *Inorg. Chem.* **2004**, *43* (23), 7353–7358.

(92) Tézé, A.; Vaissermann, J. Un nouveau dimère hétéropolytungstique $[(SiW_{10}O_{37})_2Fe_4(OH)_4]^{12-}$ formé par la réunion par deux ponts hydroxo de deux unités α-

$SiW_{10}Fe_2O_{39}$. Synthèse et structure de son sel de rubidium. *C. R. Acad. Sc. - Ser. IIC - Chem.* **2000**, *3* (2), 101–105.

(93) Kortz, U.; Tézé, A.; Hervé, G. A Cubane-Substituted Polyoxoanion: Structure and Magnetic Properties of $Cs_2[H_2PW_9Ni_4O_{34}(OH)_3(H_2O)_6]\cdot 5H_2O$. *Inorg. Chem.* **1999**, *38* (9), 2038–2042.

(94) Li, S.; Liu, S.; Tang, Q.; Liu, Y.; He, D.; Wang, S.; Shi, Z. Borate-Templated Self-Assembly of Multinuclear Nickel(II)-Containing POMs. *Dalton Trans.* **2013**, *42* (37), 13319–13322.

(95) Ibrahim, M.; Xiang, Y.; Bassil, B. S.; Lan, Y.; Powell, A. K.; de Oliveira, P.; Keita, B.; Kortz, U. Synthesis, Magnetism, and Electrochemistry of the Ni14- and Ni5-Containing Heteropolytungstates $[Ni_{14}(OH)_6(H_2O)_{10}(HPO_4)_4(P_2W_{15}O_{56})_4]^{34-}$ and $[Ni_5(OH)_4(H_2O)_4(\beta\text{-}GeW_9O_{34})(\beta\text{-}GeW_8O_{30}(OH))]^{13-}$. *Inorg. Chem.* **2013**, *52* (15), 8399–8408.

(96) Goura, J.; Bassil, B. S.; Ma, X.; Rajan, A.; Moreno-Pineda, E.; Schnack, J.; Ibrahim, M.; Powell, A. K.; Ruben, M.; Wang, J.; Ruhlmann, L.; Kortz, U. Ni^{II}_{36}-Containing 54-Tungsto-6-Silicate: Synthesis, Structure, Magnetic and Electrochemical Studies. *Chem. – Eur. J.* **2021**, *27* (61), 15081–15085.

(97) Dong, K.; Ma, P.; Wu, H.; Wu, Y.; Niu, J.; Wang, J. Cobalt- and Nickel-Containing Germanotungstates Based on Open Wells–Dawson Structure: Synthesis and Characterization of Tetrameric Anion. *Inorg. Chem.* **2019**, *58* (9), 6000–6007.

(98) Blasco-Ahicart, M.; Soriano-López, J.; Galán-Mascarós, J. R. Conducting Organic Polymer Electrodes with Embedded Polyoxometalate Catalysts for Water Splitting. *ChemElectroChem* **2017**, *4* (12), 3296–3301.

(99) Ahmad, W.; Gao, Q.; Zhang, X.-L.; Tan, W.; Zhang, L.; Gao, M.-R.; Yu, S.-H. Sandwich-Type Polyoxometalate Mediates Cobalt Diselenide for Hydrogen Evolution in Acidic Electrolyte. *ChemNanoMat* **2020**, *6* (8), 1164–1168.

(100) Duan, Y.; Clemente-Juan, J. M.; Fierro, J. L. G.; Giménez-Saiz, C.; Coronado, E. A Decacobalt(II) Cluster with Triple-Sandwich Structure Obtained by Partial Reductive Hydrolysis of a Pentacobalt(II/III) Weakley-Type Polyoxometalate. *Chem. Commun.* **2016**, *52* (90), 13245–13248.

(101) Zhang, X.; Pope, M. T. High-Valent Manganese in Polyoxotungstates. 4. Catalytic and Stoichiometric Alkene Oxidation. *J. Mol. Catal. Chem.* **1996**, *114* (1), 201–208.

(102) Bassil, B. S.; Ibrahim, M.; Al-Oweini, R.; Asano, M.; Wang, Z.; van Tol, J.; Dalal, N. S.; Choi, K.-Y.; Ngo Biboum, R.; Keita, B.; Nadjo, L.; Kortz, U. A Planar $Mn_{19}(OH)_{122}^{6+}$ Unit Incorporated in a 60-Tungsto-6-Silicate Polyanion. *Angew. Chem. Int. Ed.* **2011**, *50* (26), 5961–5964.

(103) Gupta, R.; Khan, I.; Hussain, F.; Bossoh, A. M.; Mbomekallé, I. M.; de Oliveira, P.; Sadakane, M.; Kato, C.; Ichihashi, K.; Inoue, K.; Nishihara, S. Two New Sandwich-Type Manganese {Mn5}-Substituted Polyoxotungstates: Syntheses, Crystal Structures, Electrochemistry, and Magnetic Properties. *Inorg. Chem.* **2017**, *56* (15), 8759–8767.

(104) Goura, J.; Bassil, B. S.; Bindra, J. K.; Rutkowska, I. A.; Kulesza, P. J.; Dalal, N. S.; Kortz, U. Fe^{III}_{48}-Containing 96-Tungsto-16-Phosphate: Synthesis, Structure, Magnetism and Electrochemistry. *Chem. – Eur. J.* **2020**, *26* (68), 15821–15824.

(105) Singh, V.; Chen, Z.; Ma, P.; Zhang, D.; Drew, M. G. B.; Niu, J.; Wang, J. Unprecedented $\{Fe^{14}\}/\{Fe^{10}\}$ Polyoxotungstate-Based Nanoclusters with Efficient Photocatalytic H_2 Evolution Activity: Synthesis, Structure, Magnetism, and Electrochemistry. *Chem. – Eur. J.* **2016**, *22* (31), 10983–10989.

(106) Godin, B.; Chen, Y.-G.; Vaissermann, J.; Ruhlmann, L.; Verdaguer, M.; Gouzerh, P. Coordination Chemistry of the Hexavacant Tungstophosphate $[H_2P_2W_{12}O_{48}]^{12-}$ with Fe^{III} Ions: Towards Original Structures of Increasing Size and Complexity. *Angew. Chem. Int. Ed.* **2005**, *44* (20), 3072–3075.

(107) Mialane, P.; Dolbecq, A.; Marrot, J.; Rivière, E.; Sécheresse, F. A Nonanuclear Copper(II) Polyoxometalate Assembled Around a μ-1,1,1,3,3,3-Azido Ligand and Its Parent Tetranuclear Complex. *Chem. – Eur. J.* **2005**, *11* (6), 1771–1778.

(108) Zhou, Z.; Zhang, D.; Yang, L.; Ma, P.; Si, Y.; Kortz, U.; Niu, J.; Wang, J. Nona-Copper(II)-Containing 18-Tungsto-8-Arsenate(III) Exhibits Antitumor Activity. *Chem. Commun.* **2013**, *49* (45), 5189–5191.

(109) Su, Z.-M.; Zhang, M.; An, Q.; Qin, D.; Li, H.-L.; Lv, H.; Jia, Z.; Zhang, Q.; Yang, G.-Y. Synthesis of Two New Copper-Sandwiched Polyoxotungstates and the Influence of Nuclear Number on Catalytic Hydrogen Evolution Activity. *New J. Chem.* **2020**, *44* (26), 11035–11041.

(110) Rosu, C.; Rasu, D.; Weakley, T. J. R. X-Ray Structure of Dodecasodium Tricopper(II)Bis[Nonatungstabismuthate(III) Hydrate, a Polyoxometalate Salt Containing α-B-BiW_9O_{33} Units. *J. Chem. Crystallogr.* **2003**, *33* (10), 751–755.

(111) Drewes, D.; Piepenbrink, M.; Krebs, B. The First Structurally Characterized Mn(III) Substituted Sandwich-Type Polyoxotungstates. *J. Clust. Sci.* **2006**, *17* (2), 361–374.

(112) Weakley, T. J. R.; Evans, H. T.; Showell, J. S.; Tourné, G. F.; Tourné, C. M. 18-Tungstotetracobalto(II)Diphosphate and Related Anions: A Novel Structural Class of Heteropolyanions. *J. Chem. Soc. Chem. Commun.* **1973**, No. 4, 139–140.

(113) Zhang, C.-H.; Chen, Y.-G.; Liu, S.-X. Weakley Sandwich-Type Anion in Organic–Inorganic Hybrid Compound with 3D Framework. *Inorg. Chem. Commun.* **2013**, *29*, 45–48.

(114) Wang, C.-L.; Liu, S.-X.; Sun, C.-Y.; Xie, L.-H.; Ren, Y.-H.; Liang, D.-D.; Cheng, H.-Y. Bimetals Substituted Germanotungstate Complexes with Open Wells-Dawson Structure: Synthesis, Structure, and Electrochemical Behavior of $[\{M(H_2O)\}(\mu\text{-}H_2O)_2K\{M(H_2O)_4\}(Ge_2W_{18}O_{66})]^{11-}$(M=Co, Ni, Mn). *J. Mol. Struct.* **2007**, *841* (1), 88–95.

(115) Wang, J.; Ma, P.; Shen, Y.; Niu, J. Tetra-Transition-Metal Substituted Weakley-Type Sandwich Germanotungstates and Their Derivatives Decorated by Transition-Metal Complexes. *Cryst. Growth Des.* **2008**, *8* (9), 3130–3133.

(116) Yao, S.; Yan, J.; Yu, Y.; Wang, E. Mixed-Valence Manganese Cluster Containing a Sandwich-Type Polyoxometalate. *J. Coord. Chem.* **2012**, *65* (8), 1451–1458.

(117) Bösing, M.; Loose, I.; Pohlmann, H.; Krebs, B. New Strategies for the Generation of Large Heteropolymetalate Clusters: The β-B-SbW_9 Fragment as a Multifunctional Unit. *Chem. – Eur. J.* **1997**, *3* (8), 1232–1237.

(118) Haouas, M.; Diab, M.; Moussawi, M. A.; Cadot, E.; Floquet, S.; Henry, M.; Taulelle, F. Investigation of the Protonation State of the Macrocyclic $\{H_nP_8W_{48}O_{184}\}$ Anion by Modeling ^{183}W NMR Chemical Shifts. *New J. Chem.* **2017**, *41* (14), 6112–6119.

(119) Mal, S. S.; Dickman, M. H.; Kortz, U.; Todea, A. M.; Merca, A.; Bögge, H.; Glaser, T.; Müller, A.; Nellutla, S.; Kaur, N.; van Tol, J.; Dalal, N. S.; Keita, B.; Nadjo, L. Nucleation Process in the Cavity of a 48-Tungstophosphate Wheel Resulting in a 16-Metal-Centre Iron Oxide Nanocluster. *Chem. – Eur. J.* **2008**, *14* (4), 1186–1195.

(120) Sankar Mal S., Bassil B., Ibrahim M., Nellutla S., van Tol J., Dalal N., Fernández J., López X., Poblet J., Ngo Biboum R., Keita B., Kortz U. Wheel-Shaped Cu20-Tungstophosphate $[Cu_{20}X(OH)_{24}(H_2O)_{12}(P_8W_{48}O_{184})]^{25-}$ Ion (X = Cl, Br, I) and the Role of the Halide Guest *Inorg. Chem* **2009**, 48, 24, 11636-11645

(121) Leyrie, M.; Herve, G. Synthesis and Chemical Behavior of a New Heteropolytungstate - $(MnAs_4W_{40}O_{140})^{(28-n)-}$, an Inorganic Cryptate (M^{n+}=Na^+, K^+, Ba^{2+}). *Nouv. J. Chim.* **1978**, *2* (3), 233–237.

(122) Robert, F.; Leyrie, M.; Herve, G.; Teze, A.; Jeannin, Y. Crystal Structure of Ammonium Dicobalto(II)-40-Tungstotetraarsenate(III). Allosteric Effects in the Ligand. *Inorg. Chem.* **1980**, *19* (6), 1746–1752.

(123) Gang-Lin, X.; Bin, L.; Wen-Liang, W.; Qian-Ding, L.; Ji-Wu, W.; Da-Qi, W. Crystal Structure and Characterization of a Large Polyoxotungstate $(NH_4)_{21}La(H_2O)_5[Ni(H_2O)]_2As_4W_{40}O_{140}\cdot 53H_2O$. *Chin. J. Chem.* **2003**, *21* (3), 282–286.

(122) Sanchez, C.; Livage, J.; Leyrie, M.; Herve, G.; Morgenstern, I. Magnetic Exchange Over a Long-Distance in the $K_{23}(KAs_4W_{40}O_{140}Cu_2(H_2O)_2)$,$18H_2O$ and $K_{23}(KAs_4W_{40}O_{140}(VO)_2)$,$18H_2O$ Complexes. *Bull. Soc. Chim. Fr. Partie -Physicochim. Syst. Liq. Electrochimie Catal. Genie Chim.* **1981**, No. 11–1, 397–398.

(125) Stuckart, M.; Izarova, N. V.; Glöß, M.; Klose, J.; Schmitz-Antoniak, C.; Kögerler, P.; Kersting, B.; Monakhov, K. Yu. Insertion of V^{IV} Ions into the Polyoxotungstate Archetype $\{As_4W_{40}\}$. *Inorg. Chem.* **2021**, *60* (12), 8437–8441.

(126) Lin, Z.; Izarova, N. V.; Mehari, F. T.; Kortz, U. Palladium(II) Incorporation in the All-Inorganic Cryptand $[As_4W_{40}O_{140}]^{28-}$: Synthesis and Structural Characterization of $[Pd_2Na_2KAs_4W_{40}O_{140}(H_2O)]^{21-}$. *Z. Für Anorg. Allg. Chem.* **2018**, *644* (22), 1379–1382.

(127) Wassermann, K.; Pope, M. T. Large Cluster Formation through Multiple Substitution with Lanthanide Cations (La, Ce, Nd, Sm, Eu, and Gd) of the Polyoxoanion $[(B\text{-}\alpha\text{-}AsO_3W_9O_{30})_4(WO_2)_4]^{28-}$. Synthesis and Structural Characterization. *Inorg. Chem.* **2001**, *40* (12), 2763–2768.

(128) Cotton, F. A. Transition-Metal Compounds Containing Clusters of Metal Atoms. *Q. Rev. Chem. Soc.* **1966**, *20* (3), 389–401.

(129) Lassalle-Kaiser, B.; Merki, D.; Vrubel, H.; Gul, S.; Yachandra, V. K.; Hu, X.; Yano, J. Evidence from in Situ X-Ray Absorption Spectroscopy for the Involvement of Terminal Disulfide in the Reduction of Protons by an Amorphous Molybdenum Sulfide Electrocatalyst. *J. Am. Chem. Soc.* **2015**, *137* (1), 314–321.

(130) Zhou, Q.; Su, S.; Cheng, P.; Hu, X.; Gao, X.; Zhang, Z.; Liu, J.-M. Vertically Conductive MoS_2 Pyramids with a High Density of Active Edge Sites for Efficient Hydrogen Evolution. *J. Mater. Chem. C* **2020**, *8* (9), 3017–3022.

(131) Lei, Y.; Yang, M.; Hou, J.; Wang, F.; Cui, E.; Kong, C.; Min, S. Thiomolybdate $[Mo_3S_{13}]^{2-}$ Nanocluster: A Molecular Mimic of MoS_2 Active Sites for Highly Efficient Photocatalytic Hydrogen Evolution. *Chem. Commun.* **2018**, *54* (6), 603–606.

(132) Jaramillo, T. F.; Bonde, J.; Zhang, J.; Ooi, B.-L.; Andersson, K.; Ulstrup, J.; Chorkendorff, I. Hydrogen Evolution on Supported Incomplete Cubane-Type [Mo3S4]4+ Electrocatalysts. *J. Phys. Chem. C* **2008**, *112* (45), 17492–17498.

(133) Hou, Y.; Abrams, B. L.; Vesborg, P. C. K.; Björketun, M. E.; Herbst, K.; Bech, L.; Setti, A. M.; Damsgaard, C. D.; Pedersen, T.; Hansen, O.; Rossmeisl, J.; Dahl, S.; Nørskov, J. K.; Chorkendorff, I. Bioinspired Molecular Co-Catalysts Bonded to a Silicon Photocathode for Solar Hydrogen Evolution. *Nat. Mater.* **2011**, *10* (6), 434–438.

(134) Cadot, E.; Sokolov, M. N.; Fedin, V. P.; Simonnet-Jégat, C.; Floquet, S.; Sécheresse, F. A Building Block Strategy to Access Sulfur-Functionalized Polyoxometalate Based Systems Using $\{Mo_2S_2O_2\}$ and $\{Mo_3S_4\}$ as Constitutional Units, Linkers or Templates. *Chem. Soc. Rev.* **2012**, *41* (22), 7335–7353.

(135) Duval, S.; Pilette, M.-A.; Marrot, J.; Simonnet-Jégat, C.; Sokolov, M.; Cadot, E. Selective Inclusion of Cu^+ and Ag^+ Electron-Rich Metallic Cations within Supramolecular Polyoxometalates Based on $\{AsW_9O_{33}\}\{Mo_3S_4\}$ Combinations. *Chem. – Eur. J.* **2008**, *14* (11), 3457–3466.

(136) Müller, A.; Fedin, V. P.; Kuhlmann, C.; Bögge, H.; Hauptfleisch, B.; Fedin, V. P.; Fenske, H.-D.; Baum, G. 'Adding' Stable Functional Complementary, Nucleophilic and Electrophilic Clusters: A Synthetic Route to $[\{(SiW_{11}O_{39})Mo_3S_4(H_2O)_3(\mu\text{-}OH)\}_2]^{10-}$ and $[\{(P_2W_{17}O_{61})Mo_3S_4(H_2O)_3(\mu\text{-}OH)\}_2]^{14-}$ as Examples. *Chem. Commun.* **1999**, No. 13, 1189–1190.

(137) Sokolov, M. N.; Kalinina, I. V.; Peresypkina, E. V.; Cadot, E.; Tkachev, S. V.; Fedin, V. P. Incorporation of Molybdenum Sulfide Cluster Units into a Dawson-Like Polyoxometalate Structure To Give Hybrid Polythiooxometalates. *Angew. Chem. Int. Ed.* **2008**, *47* (8), 1465–1468.

(138) Tourneur, J.; Fabre, B.; Loget, G.; Vacher, A.; Mériadec, C.; Ababou-Girard, S.; Gouttefangeas, F.; Joanny, L.; Cadot, E.; Haouas, M.; Leclerc-Laronze, N.; Falaise, C.; Guillon, E. Molecular and Material Engineering of Photocathodes Derivatized with Polyoxometalate-Supported $\{Mo_3S_4\}$ HER Catalysts. *J. Am. Chem. Soc.* **2019**, *141* (30), 11954–11962.

(139) Buchecker, T.; Schmid, P.; Grillo, I.; Prévost, S.; Drechsler, M.; Diat, O.; Pfitzner, A.; Bauduin, P. Self-Assembly of Short Chain Poly-N-Isopropylacrylamid Induced by

Superchaotropic Keggin Polyoxometalates: From Globules to Sheets. *J. Am. Chem. Soc.* **2019**, *141* (17), 6890–6899.

(140) Naskar, B.; Diat, O.; Nardello-Rataj, V.; Bauduin, P. Nanometer-Size Polyoxometalate Anions Adsorb Strongly on Neutral Soft Surfaces. *J. Phys. Chem. C* **2015**, *119* (36), 20985–20992.

(141) Falaise, C.; Moussawi, M. A.; Floquet, S.; Abramov, P. A.; Sokolov, M. N.; Haouas, M.; Cadot, E. Probing Dynamic Library of Metal-Oxo Building Blocks with γ-Cyclodextrin. *J. Am. Chem. Soc.* **2018**, *140* (36), 11198–11201.

(142) Moussawi, M. A.; Leclerc-Laronze, N.; Floquet, S.; Abramov, P. A.; Sokolov, M. N.; Cordier, S.; Ponchel, A.; Monflier, E.; Bricout, H.; Landy, D.; Haouas, M.; Marrot, J.; Cadot, E. Polyoxometalate, Cationic Cluster, and γ-Cyclodextrin: From Primary Interactions to Supramolecular Hybrid Materials. *J. Am. Chem. Soc.* **2017**, *139* (36), 12793–12803.

(143) Fa Bamba, I.; Falaise, C.; Marrot, J.; Atheba, P.; Gbassi, G.; Landy, D.; Shepard, W.; Haouas, M.; Cadot, E. Host-Guest Complexation Between Cyclodextrins and Hybrid Hexavanadates: What Are the Driving Forces? *Chem. – Eur. J.* **2021**, *27* (62), 15516–15527.

(144) Assaf, K. I.; Nau, W. M. The Chaotropic Effect as an Assembly Motif in Chemistry. *Angew. Chem. Int. Ed.* **2018**, *57* (43), 13968–13981.

(145) Buchecker, T.; Schmid, P.; Renaudineau, S.; Diat, O.; Proust, A.; Pfitzner, A.; Bauduin, P. Polyoxometalates in the Hofmeister Series. *Chem. Commun.* **2018**, *54* (15), 1833–1836.

(146) Hohenschutz, M.; Grillo, I.; Diat, O.; Bauduin, P. How Nano-Ions Act Like Ionic Surfactants. *Angew. Chem. Int. Ed.* **2020**, *59* (21), 8084–8088.

(147) Moussawi, M. A.; Haouas, M.; Floquet, S.; Shepard, W. E.; Abramov, P. A.; Sokolov, M. N.; Fedin, V. P.; Cordier, S.; Ponchel, A.; Monflier, E.; Marrot, J.; Cadot, E. Nonconventional Three-Component Hierarchical Host–Guest Assembly Based on Mo-Blue Ring-Shaped Giant Anion, γ-Cyclodextrin, and Dawson-Type Polyoxometalate. *J. Am. Chem. Soc.* **2017**, *139* (41), 14376–14379.

(148) Ivanov, A. A.; Falaise, C.; Shmakova, A. A.; Leclerc, N.; Cordier, S.; Molard, Y.; Mironov, Y. V.; Shestopalov, M. A.; Abramov, P. A.; Sokolov, M. N.; Haouas, M.; Cadot, E. Cyclodextrin-Assisted Hierarchical Aggregation of Dawson-Type Polyoxometalate in the Presence of {Re6Se8} Based Clusters. *Inorg. Chem.* **2020**, *59* (16), 11396–11406.

(149) Savéant, J. M. *Elements of Molecular and Biomolecular Electrochemistry: An Electrochemical Approach to Electron Transfer Chemistry*; The George Fisher Baker non-resident lectureship in chemistry at Cornell University; Wiley-Interscience: Hoboken, N.J, 2006.

(150) Cherevan, A. S.; Nandan, S. P.; Roger, I.; Liu, R.; Streb, C.; Eder, D. Polyoxometalates on Functional Substrates: Concepts, Synergies, and Future Perspectives. *Adv. Sci.* **2020**, *7* (8), 1903511.

(151) Zhang, X. G. *Electrochemistry of Silicon and Its Oxide*; Kluwer Academic/Plenum Publishers: New York, 2001.

(152) Koval, C. A.; Howard, J. N. Electron Transfer at Semiconductor Electrode-Liquid Electrolyte Interfaces. *Chem. Rev.* **1992**, *92* (3), 411–433.

(153) Tan, M. X.; Laibinis, P. E.; Nguyen, S. T.; Kesselman, J. M.; Stanton, C. E.; Lewis, N. S. Principles and Applications of Semiconductor Photoelectrochemistry. In *Progress in Inorganic Chemistry*; Karlin, K. D., Ed.; John Wiley & Sons, Inc.: Hoboken, NJ, USA, 2007; pp 21–144.

(154) Fabre, B. Functionalization of Oxide-Free Silicon Surfaces with Redox-Active Assemblies. *Chem. Rev.* **2016**, *116* (8), 4808–4849.

(155) Vagin, M. Yu.; Jeerapan, I.; Wannapob, R.; Thavarungkul, P.; Kanatharana, P.; Anwar, N.; McCormac, T.; Eriksson, M.; Turner, A. P. F.; Jager, E. W. H.; Mak, W. C. Water-Processable Polypyrrole Microparticle Modules for Direct Fabrication of Hierarchical Structured Electrochemical Interfaces. *Electrochim. Acta* **2016**, *190*, 495–503.

(156) Blasco-Ahicart, M.; Soriano-Lopez, J.; Galan-Mascaros, J. R. Conducting Organic Polymer Electrodes with Embedded Polyoxometalate Catalysts for Water Splitting. *ChemElectroChem* **2017**, *4*, 3296–3301.

(157) Ali, B.; Laffir, F.; Kailas, L.; Armstrong, G.; Kailas, L.; O'Connell, R.; McCormac, T. Electrochemical Characterisation of NiII-Crown-Type Polyoxometalate-Doped Polypyrrole Films for the Catalytic Reduction of Bromate in Water. *Eur. J. Inorg. Chem.* **2019**, *2019*, 394–401.

(158) Fabre, B.; Bidan, G.; Fichou, D. Électropolymérisation du thiophène, bithiophène, et terthiophène en présence d'hétéropolyanions de structure de Keggin. *J. Chim. Phys.* **1992**, *89*, 1053–1062.

(159) Fabre, B.; Bidan, G.; Lapkowski, M. Poly(N-Methylpyrrole) Films Doped with Iron-Substituted Heteropolytungstates: A New Sensitive Layer for the Amperometric Detection of Nitrite Ions. *J. Chem. Soc. Chem. Commun.* **1994**, No. 12, 1509–1511.

(160) Fabre, B.; Bidan, G. Electrosynthesis of Different Electronic Conducting Polymer Films Doped with an Iron-Substituted Heteropolytungstate: Choice of the Immobilization Matrix the Most Suitable for the Electrocatalytic Reduction of Nitrite Ions. *Electrochim. Acta* **1997**, *42* (16), 2587–2590.

(161) Keita, B.; Bouaziz, D.; Nadjo, L. Strategies for Entrapping Oxometalates in Polymeric Matrices: Example of Polyaniline as the Matrix. *J. Electroanal. Chem. Interfacial Electrochem.* **1988**, *255* (1), 307–313.

(162) Keita, B.; Nadjo, L. Surface Functionalization of Electrodes with Oxometalates Entrapped in Polymeric Matrices: Evidence for a Microenvironment Effect. *J. Electroanal. Chem. Interfacial Electrochem.* **1988**, *240* (1), 325–332.

(163) *Andrieux, C. P.; Savéant, J.-M. In Molecular Design of Electrode Surfaces*; Murray, R. W., Ed.; Techniques of Chemistry; Wiley: New York, 1992.

(164) Zhang, L.; Chen, L.; Liu, S.; Gong, J.; Tang, Q.; Su, Z. Honeycomb-Patterned Hybrid Films of Surfactant-Encapsulated Polyoxometalates by a Breath Figure Method and Its Electrocatalysis for BrO_3^-. *Dalton Trans.* **2018**, *47*, 105–111.

(165) Liu, Y.; Zhao, S.-F.; Guo, S.-X.; Bond, A. M.; Zhang, J.; Zhu, G.; Hill, C. L.; Geletii, Y. V. Electrooxidation of Ethanol and Methanol Using the Molecular Catalyst $[\{Ru_4O_4(OH)_2(H_2O)_4\}(\gamma\text{-}SiW_{10}O_{36})_2]^{10-}$. *J. Am. Chem. Soc.* **2016**, *138*, 2617–2628.

(166) Adhikary, S. D.; Tiwari, A.; Nagaiah, T. C.; Mandal, D. Stabilization of Cobalt-Polyoxometalate over Poly(Ionic Liquid) Composites for Efficient Electrocatalytic Water Oxidation. *ACS Appl. Mater. Interfaces* **2018**, *10*, 38872–38879.

(167) Gong, R.; Gao, D.; Liu, R.; Sorsche, D.; Biskupek, J.; Kaiser, U.; Rau, S.; Streb, C. Self-Activation of a Polyoxometalate-Derived Composite Electrocatalyst for the Oxygen Evolution Reaction. *ACS Appl. Energy Mater.* **2021**, *4* (11), 12671–12676.

(168) Stracke, J. J.; Finke, R. G. Electrocatalytic Water Oxidation Beginning with the Cobalt Polyoxometalate $[Co_4(H_2O)_2(PW_9O_{34})_2]^{10-}$: Identification of Heterogeneous CoO_x as the Dominant Catalyst. *J. Am. Chem. Soc.* **2011**, *133*, 14872–14875.

(169) Gumerova, N. I.; Rompel, A. Polyoxometalates in Solution: Speciation under Spotlight. *Chem. Soc. Rev.* **2020**, *49* (21), 7568–7601.

(170) Yaqub, M.; Imar, S.; Laffir, F.; Armstrong, G.; McCormac, T. Investigations into the Electrochemical, Surface, and Electrocatalytic Properties of the Surface-Immobilized Polyoxometalate, $TBA_3K[SiW_{10}O_{36}(PhPO)_2]$. *ACS Appl. Mater. Interfaces* **2015**, *7*, 1046–1056.

(171) Ali, B.; Imar, S.; Laffir, F.; McCormac, T. Electrochemical, Surface and Electrocatalytic Properties of Electrode Multilayer Assemblies Composed of a Ruthenium Metallodendrimer and a Wheel-Shaped Cu-20 Tungstophosphate. *J. Electroanal. Chem.* **2019**, *836*, 77–84.

(172) Naseer, R.; Mal, S. S.; Kortz, U.; Armstrong, G.; Laffir, F.; Dickinson, C.; Vagin, M.; McCormac, T. Electrocatalysis by Crown-Type Polyoxometalates Multi-Substituted by Transition Metal Ions; Comparative Study. *Electrochim. Acta* **2015**, *176*, 1248–1255.

(173) García, M.; Honores, J.; Quezada, D.; Díaz, C.; Dreyse, P.; Celis, F.; Kubiak, C. P.; Canzi, G.; Guzmán, F.; Aguirre, M. J.; Isaacs, M. Nitrite Reduction on a Multimetallic Porphyrin/Polyoxotungstate Layer-by-Layer Modified Electrodes. *Electrochim. Acta* **2016**, *192*, 61–71.

(174) Novais, H. C.; Fernandes, D. M.; Freire, C. Hybrid Methyl Green/Cobalt-Polyoxotungstate Nanostructured Films: Self-Assembly, Electrochemical and Electrocatalytic Properties. *Appl. Surf. Sci.* **2015**, *347*, 40–47.

(175) Ali, B.; McCormac, T.; Maccato, C.; Barreca, D.; Carraro, G. Multilayer Assemblies of a Cu-Phthalocyanine with Dawson Type Polyoxometalates (POMs) for the Electrocatalytic Reduction of Phosphate. *J. Electroanal. Chem.* **2020**, *858*, 113770.

(176) Imar, S.; Yaqub, M.; Maccato, C.; Dickinson, C.; Laffir, F.; Vagin, M.; McCormac, T. Nitrate and Nitrite Electrocatalytic Reduction at Layer-by-Layer Films Composed of Dawson-Type Heteropolyanions Mono-Substituted with Transitional Metal Ions and Silver Nanoparticles. *Electrochim. Acta* **2015**, *184*, 323–330.

(177) Imar, S.; Maccato, C.; Dickinson, C.; Laffir, F.; Vagin, M.; McCormac, T. Enhancement of Nitrite and Nitrate Electrocatalytic Reduction through the Employment of Self-Assembled Layers of Nickel- and Copper-Substituted Crown-Type Heteropolyanions. *Langmuir* **2015**, *31*, 2584–2592.

(178) Ali, B.; Imar, S.; Laffir, F.; Kailas, L.; Maccato, C.; McCormac, T. Electrochemical, Surface and Electrocatalytic Properties of Layer-by-Layer Multilayer Assemblies Composed of Silver Nanoparticles and a Ni(II)-Crown Type Polyoxometalate. *J. Electroanal. Chem.* **2018**, *824*, 75–82.

(179) Zhu, D.; Zuo, J.; Tan, L.; Pang, H.; Ma, H. Enzymeless Electrochemical Determination of Hydrogen Peroxide at a Heteropolyanion-Based Composite Film Electrode. *New J. Chem.* **2019**, *43*, 1053–1062.

(180) He, X.; Chen, L.; Li, Z.; Zhang, X.; Ma, A.; Lin, S. Enhanced Electrocatalysis for Methanol Oxidation on Ordered $\{[PdPW_{11}O_{39}]^{5-}/Pt/PAMAM\}_n$ Multilayer Composites. *Fuel Cells* **2015**, *15*, 221–229.

(181) Zhang, X.; Chen, H.; Zhang, H. Layer-by-Layer Assembly: From Conventional to Unconventional Methods. *Chem. Commun* **2007**, No. 14, 1395–1405.

(182) Furukawa, H.; Cordova, K. E.; O'Keeffe, M.; Yaghi, O. M. The Chemistry and Applications of Metal-Organic Frameworks. *Science* **2013**, *341* (6149).

(183) Mialane, P.; Mellot-Draznieks, C.; Gairola, P.; Duguet, M.; Benseghir, Y.; Oms, O.; Dolbecq, A. Heterogenisation of Polyoxometalates and Other Metal-Based Complexes in Metal–Organic Frameworks: From Synthesis to Characterisation and Applications in Catalysis. *Chem. Soc. Rev.* **2021**, *50* (10), 6152–6220.

(184) Buru, C. T.; Farha, O. K. Strategies for Incorporating Catalytically Active Polyoxometalates in Metal–Organic Frameworks for Organic Transformations. *ACS Appl. Mater. Interfaces* **2020**, *12* (5), 5345–5360.

(185) Samaniyan, M.; Mirzaei, M.; Khajavian, R.; Eshtiagh-Hosseini, H.; Streb, C. Heterogeneous Catalysis by Polyoxometalates in Metal–Organic Frameworks. *ACS Catal.* **2019**, *9* (11), 10174–10191.

(186) Han, J.; Wang, D.; Du, Y.; Xi, S.; Chen, Z.; Yin, S.; Zhou, T.; Xu, R. Polyoxometalate Immobilized in MIL-101(Cr) as an Efficient Catalyst for Water Oxidation. *Appl. Catal. Gen.* **2016**, *521*, 83–89.

(187) Shah, W. A.; Waseem, A.; Nadeem, M. A.; Kögerler, P. Leaching-Free Encapsulation of Cobalt-Polyoxotungstates in MIL-100 (Fe) for Highly Reproducible Photocatalytic Water Oxidation. *Appl. Catal. Gen.* **2018**, *567*, 132–138.

(188) Mukhopadhyay, S.; Debgupta, J.; Singh, C.; Kar, A.; Das, S. K. A Keggin Polyoxometalate Shows Water Oxidation Activity at Neutral pH: POM@ZIF-8, an Efficient and Robust Electrocatalyst. *Angew. Chem. Int. Ed.* **2018**, *57* (7), 1918–1923.

(189) Abdelkader-Fernández, V. K.; Fernandes, D. M.; Balula, S. S.; Cunha-Silva, L.; Freire, C. Oxygen Evolution Reaction Electrocatalytic Improvement in POM@ZIF

Nanocomposites: A Bidirectional Synergistic Effect. *ACS Appl. Energy Mater.* **2020**, *3* (3), 2925–2934.

(190) Liu, H.; Gong, L.-G.; Wang, C.-X.; Wang, C.-M.; Yu, K.; Zhou, B.-B. $\{Cu_2SiW_{12}O_{40}\}$@HKUST-1 Synthesized by a One-Step Solution Method with Efficient Bifunctional Activity for Supercapacitors and the Oxygen Evolution Reaction. *J. Mater. Chem. A* **2021**, *9* (22), 13161–13169.

(191) Mukhopadhyay, S.; Basu, O.; Kar, A.; Das, S. K. Efficient Electrocatalytic Water Oxidation by Fe(Salen)–MOF Composite: Effect of Modified Microenvironment. *Inorg. Chem.* **2020**, *59* (1), 472–483.

(192) Sun, M.-L.; Wang, Y.-R.; He, W.-W.; Zhong, R.-L.; Liu, Q.-Z.; Xu, S.; Xu, J.-M.; Han, X.-L.; Ge, X.; Li, S.-L.; Lan, Y.-Q.; Al-Enizi, A. M.; Nafady, A.; Ma, S. Efficient Electron Transfer from Electron-Sponge Polyoxometalate to Single-Metal Site Metal–Organic Frameworks for Highly Selective Electroreduction of Carbon Dioxide. *Small* **2021**, *17* (20), 2100762.

(193) Zhang, Y.; Zhang, Y.; Li, L.; Chen, J.; Li, P.; Huang, W. One-Step in Situ Growth of High-Density POMOFs Films on Carbon Cloth for the Electrochemical Detection of Bromate. *J. Electroanal. Chem.* **2020**, *861*, 113939.

(194) Wang, C.; Zhou, M.; Ma, Y.; Tan, H.; Wang, Y.; Li, Y. Hybridized Polyoxometalate-Based Metal–Organic Framework with Ketjenblack for the Nonenzymatic Detection of H2O2. *Chem. – Asian J.* **2018**, *13* (16), 2054–2059.

(195) Sun, M.-L.; Wang, Y.-R.; He, W.-W.; Zhong, R.-L.; Liu, Q.-Z.; Xu, S.; Xu, J.-M.; Han, X.-L.; Ge, X.; Li, S.-L.; Lan, Y.-Q.; Al-Enizi, A. M.; Nafady, A.; Ma, S. Efficient Electron Transfer from Electron-Sponge Polyoxometalate to Single-Metal Site Metal–Organic Frameworks for Highly Selective Electroreduction of Carbon Dioxide. *Small* **2021**, *17* (20), 2100762.

(196) Qin, J.-S.; Du, D.-Y.; Guan, W.; Bo, X.-J.; Li, Y.-F.; Guo, L.-P.; Su, Z.-M.; Wang, Y.-Y.; Lan, Y.-Q.; Zhou, H.-C. Ultrastable Polymolybdate-Based Metal–Organic Frameworks as Highly Active Electrocatalysts for Hydrogen Generation from Water. *J. Am. Chem. Soc.* **2015**, *137* (22), 7169–7177.

(197) Rousseau, G.; Rodriguez-Albelo, L. M.; Salomon, W.; Mialane, P.; Marrot, J.; Doungmene, F.; Mbomekallé, I.-M.; de Oliveira, P.; Dolbecq, A. Tuning the Dimensionality of Polyoxometalate-Based Materials by Using a Mixture of Ligands. *Cryst. Growth Des.* **2015**, *15* (1), 449–456.

(198) Salomon, W.; Paille, G.; Gomez-Mingot, M.; Mialane, P.; Marrot, J.; Roch-Marchal, C.; Nocton, G.; Mellot-Draznieks, C.; Fontecave, M.; Dolbecq, A. Effect of Cations on the Structure and Electrocatalytic Response of Polyoxometalate-Based Coordination Polymers. *Cryst. Growth Des.* **2017**, *17* (4), 1600–1609.

(199) Peng, H.; Yang, X.; Ma, Y.; Liu, J.; Wang, Y.; Tan, H.; Li, Y. Polyoxometalate-Based Metal–Organic Framework Loaded with an Ultra-Low Amount of Pt as an Efficient Electrocatalyst for Hydrogen Production. *CrystEngComm* **2018**, *20* (36), 5387–5394.

(200) Dong, B.-X.; Chen, L.; Zhang, S.-Y.; Wu, Y.-C.; Tian, H.; Ge, J.; Song, L.; Teng, Y.-L.; Liu, W.-L. A New 2D Network Constructed from the Extension of Transition-Metal-Grafted ε-Keggin Polyoxoanion by a Bridging Organic Carboxylate. *J. Clust. Sci.* **2015**, *26* (5), 1595–1605.

(201) Dong, B.-X.; Chen, L.; Zhang, S.-Y.; Ge, J.; Song, L.; Tian, H.; Teng, Y.-L.; Liu, W.-L. The First Tritopic Bridging Ligand 1,3,5-Tris(4-Carboxyphenyl)-Benzene (H_3BTB) Functionalized Porous Polyoxometalate-Based Metal–Organic Framework (POMOF): From Design, Synthesis to Electrocatalytic Properties. *Dalton Trans.* **2014**, *44* (3), 1435–1440.

(202) Wang, Y.-R.; Huang, Q.; He, C.-T.; Chen, Y.; Liu, J.; Shen, F.-C.; Lan, Y.-Q. Oriented Electron Transmission in Polyoxometalate-Metalloporphyrin Organic Framework for Highly Selective Electroreduction of CO_2. *Nat. Commun.* **2018**, *9* (1), 4466.

(203) Tian, A.-X.; Ning, Y.-L.; Ying, J.; Liu, G.-C.; Hou, X.; Li, T.-J.; Wang, X.-L. Subtly Tuning One N Site of Benzyl-1H-Triazole Ligands to Build Mono-Nuclear Subunits and Tri-Nuclear Clusters to Modify Polyoxometalates. *CrystEngComm* **2015**, *17* (29), 5569–5578.

(204) Li, S.; Zhang, L.; Ma, H.; Pang, H.; Zhao, C. Tuning the Topology Structures of Polymolybdate-Based Hybrids from Interpenetrated Framework to Interdigitated Architecture via Changing Polymolybdate Clusters. *New J. Chem.* **2015**, *39* (5), 3528–3535.

(205) Zhao, C.; Ma, H.; Pang, H.; Li, S.; Zhang, Z.; Yu, Y. A New POMOF Consisting of $[VW_{12}]^{4-}$ Clusters and Metal-Organic Nanotubes: Synthesis, Structure, Electrocatalytic and Luminescent Properties. *Inorg. Chem. Commun.* **2016**, *69*, 57–61.

(206) Zhao, C.; Li, S.; Ma, H.; Zhang, C.; Pang, H.; Yu, Y.; Zhang, Z. The Factors Affecting the Assembly of Keggin–Metal–Bimb Systems: Charge/Polarity of Keggin Polyanions and Coordination Modes of Metal Cations. *CrystEngComm* **2016**, *18* (33), 6233–6244.

(207) Wang, X.; Sun, J.; Lin, H.; Chang, Z.; Wang, X.; Liu, G. A Series of Anderson-Type Polyoxometalate-Based Metal–Organic Complexes: Their PH-Dependent Electrochemical Behaviour, and as Electrocatalysts and Photocatalysts. *Dalton Trans.* **2016**, *45* (31), 12465–12478.

(208) Wang, X.-L.; Sun, J.; Lin, H.; Chang, Z.; Bai, X.; Wang, X. Assembly, Structures, Electrocatalytic and Photocatalytic Properties of a Series of Anderson-Type Polyoxometalate-Based Metal–Organic Complexes Based on Flexible Pyridyl-Amide Ligands. *Polyhedron* **2017**, *124*, 30–40.

(209) Lu, B.; Wu, Y.; Li, S.; Yang, X.; Yan, E.; Chen, J.; Ma, H.; Wang, J.; Zhu, Y.; Tao, D. PH-Dependent Assembly of Two Polyoxometalate-Based Coordination Polymers: Structures and Electrocatalytic Properties. *J. Coord. Chem.* **2019**, *72* (2), 283–293.

(210) Zhou, W.; Peng, J.; Zhang, Z.; Shi, Z.; Ullah Khan, S.; Liu, H. Assembly of Hybrids Based on Polyoxotungstates and Co-Tris(Imidazolyl) Complexes with Bifunctional Electrocatalytic Activities. *RSC Adv.* **2015**, *5* (45), 35753–35759.

(211) Ren, Y.; Li, L.; Mu, B.; Li, C.; Huang, R. Electrocatalytic Properties of Three New POMs-Based Inorganic–Organic Frameworks with Flexible Zwitterionic Dicarboxylate Ligands. *J. Solid State Chem.* **2017**, *249*, 1–8.

(212) Wang, Y.-J.; Zhou, Y.-Y.; Hao, H.-G.; Song, M.; Zhang, N.; Yao, S.; Yan, J.-H.; Zhang, Z.-M.; Lu, T.-B. Capped Polyoxometalate Pillars between Metal–Organic Layers for Transferring a Supramolecular Structure into a Covalent 3D Framework. *Inorg. Chem.* **2018**, *57* (3), 1342–1349.

(213) Cao, Y.; Lv, J.; Yu, K.; Wang, C.; Su, Z.; Wang, L.; Zhou, B. Synthesis and Photo-/Electro-Catalytic Properties of Keggin Polyoxometalate Inorganic–Organic Hybrid Layers Based on d^{10} Metal and Rigid Benzo-Diazole/-Triazole Ligands. *New J. Chem.* **2017**, *41* (21), 12459–12469.

(214) Zhang, Z.; Sun, X.; Ma, H.; Pang, H.; Li, S.; Zhao, C. Two Hybrid Compounds Constructed from Ni-Tris(Imidazolyl) Complexes and Keggin Clusters: Syntheses, Structures and Electrochemical Properties. *J. Mol. Struct.* **2016**, *1116*, 174–179.

(215) Wang, X.; Zhang, S.; Wang, X.; Liu, G.; Lin, H.; Zhang, H. Various Polyoxomolybdate-Based Hybrids Induced by PH and Solvents: Structures, Adsorption Activities for Dyes and Bifunctional Electrocatalytic Properties. *Dalton Trans.* **2017**, *46* (47), 16580–16588.

(216) Cong, B.-W.; Su, Z.-H.; Zhao, Z.-F.; Yu, B.-Y.; Zhao, W.-Q.; Ma, X.-J. Two Unusual 3D Honeycomb Networks Based on Wells–Dawson Arsenomolybdates with D10 Transition-Metal-Pyrazole Connectors. *Dalton Trans.* **2017**, *46* (23), 7577–7583.

(217) Hummers, W. S.; Offeman, R. E. Preparation of Graphitic Oxide. *J. Am. Chem. Soc.* **1958**, *80* (6), 1339–1339.

(218) Liu, R.; Zhang, G.; Cao, H.; Zhang, S.; Xie, Y.; Haider, A.; Kortz, U.; Chen, B.; Dalal, N. S.; Zhao, Y.; Zhi, L.; Wu, C.-X.; Yan, L.-K.; Su, Z.; Keita, B. Enhanced Proton and Electron Reservoir Abilities of Polyoxometalate Grafted on Graphene for High-Performance Hydrogen Evolution. *Energy Environ. Sci.* **2016**, *9* (3), 1012–1023.

(219) Fernandes, D. M.; Araújo, M. P.; Haider, A.; Mougharbel, A. S.; Fernandes, A. J. S.; Kortz, U.; Freire, C. Polyoxometalate-Graphene Electrocatalysts for the Hydrogen Evolution Reaction. *ChemElectroChem* **2018**, *5* (2), 273–283.

(220) Ensafi, A. A.; Heydari-Soureshjani, E.; Jafari-Asl, M.; Rezaei, B. Polyoxometalate-Decorated Graphene Nanosheets and Carbon Nanotubes, Powerful Electrocatalysts for Hydrogen Evolution Reaction. *Carbon* **2016**, *99*, 398–406.

(221) Ensafi, A. A.; Heydari-Soureshjani, E.; Rezaei, B. Nanostructure Polyoxometalates Containing Co, Ni, and Cu as Powerful and Stable Catalysts for Hydrogen Evolution Reaction in Acidic and Alkaline Solutions. *Int. J. Hydrog. Energy* **2017**, *42* (8), 5026–5034.

(222) Ahmadpour, A.; Khadempir, S.; Ashraf, N.; Mitchell, S. G.; Ahangari, M. H. A One-Pot Route for the Synthesis of Au@Pd/PMo_{12}/RGO as a Dual Functional Electrocatalyst for Ethanol Electro-Oxidation and Hydrogen Evolution Reaction. *RSC Adv.* **2019**, *9* (64), 37537–37545.

(223) Li, Y.; Chang, X.-R.; Sang, X.-J.; Li, J.-S.; Luo, Y.-H.; Zhu, Z.-M.; You, W.-S. Keggin-Type Polyoxometalate Modified Ag/Graphene Composite Materials for Electrocatalytic Water Oxidation. *Eur. J. Inorg. Chem.* **2019**, *2019* (31), 3597–3604.

(224) Liu, R.; Xian, Z.; Zhang, S.; Chen, C.; Yang, Z.; Li, H.; Zheng, W.; Zhang, G.; Cao, H. Electrochemical-Reduction-Assisted Assembly of Ternary Ag Nanoparticles/Polyoxometalate/Graphene Nanohybrids and Their Activity in the Electrocatalysis of Oxygen Reduction. *RSC Adv.* **2015**, *5* (91), 74447–74456.

(225) Zhang, S.; Oms, O.; Hao, L.; Liu, R.; Wang, M.; Zhang, Y.; He, H.-Y.; Dolbecq, A.; Marrot, J.; Keita, B.; Zhi, L.; Mialane, P.; Li, B.; Zhang, G. High Oxygen Reduction Reaction Performances of Cathode Materials Combining Polyoxometalates, Coordination Complexes, and Carboneous Supports. *ACS Appl. Mater. Interfaces* **2017**, *9* (44), 38486–38498.

(226) Shi, H.; Wang, R.; Lou, M.; Jia, D.; Guo, Y.; Wang, X.; Huang, Y.; Sun, Z.; Wang, T.; Wang, L. A Novel Pt/Pyridine Ionic Liquid Polyoxometalate/RGO Tri-Component Hybrid and Its Enhanced Activities for Methanol Electrooxidation. *Electrochim. Acta* **2019**, *294*, 93–101.

(227) Gao, S.; Yang, X.; Wei, M.-J.; Liang, S.; Zang, H.-Y.; Tan, H.-Q.; Wang, Y.-H.; Li, Y.-G. One-Step Synthesis of Pt Based Electrocatalysts Encapsulated by Polyoxometalate for Methanol Oxidation. *New J. Chem.* **2017**, *42* (1), 198–203.

(228) Hu, J.; Wu, X.; Zhang, Q.; Gao, M.; Qiu, H.; Huang, K.; Feng, S.; Wang, T.; Yang, Y.; Liu, Z.; Zhao, B. Highly Active PdNi/RGO/Polyoxometalate Nanocomposite Electrocatalyst for Alcohol Oxidation. *Langmuir* **2018**, *34* (8), 2685–2691.

(229) Wei, X.; Wei, J.; Huang, L.; Yan, T.; Luo, F. Facile Fabricating the Polyoxometalates Functionalized Graphene Nanocomposite Applied in Electrocatalytic Reduction. *Inorg. Chem. Commun.* **2017**, *81*, 10–14.

(230) Yang, M.; Kim, D. S.; Lee, T. J.; Lee, S. J.; Lee, K. G.; Choi, B. G. Polyoxometalate-Grafted Graphene Nanohybrid for Electrochemical Detection of Hydrogen Peroxide and Glucose. *J. Colloid Interface Sci.* **2016**, *468*, 51–56.

(231) Zhang, L.; Li, S.; Zhang, Z.; Tan, L.; Pang, H.; Ma, H. Facile Fabrication of Reduced Graphene Oxide and Keggin-Type Polyoxometalates Nanocomposite Film for High Performance Electrocatalytic Oxidation of Nitrite. *J. Electroanal. Chem.* **2017**, *807*, 97–103.

(232) Wang, Q.; Khungwa, J.; Li, L.; Liu, Y.; Wang, X.; Wang, S. Fabrication of Polyoxometalate/GO/PDDA Hybrid Nanocomposite Modified Electrode and Electrocatalysis for Nitrite Ion, Ascorbic Acid and Dopamine. *J. Electroanal. Chem.* **2018**, *824*, 91–98.

(233) Chen, S.; Xiang, Y.; Katherine Banks, M.; Xu, W.; Peng, C.; Wu, R. Polyoxometalate-Coupled Graphene Nanohybrid via Gemini Surfactants and Its Electrocatalytic Property for Nitrite. *Appl. Surf. Sci.* **2019**, *466*, 110–118.

(234) Guo, W.; Tong, X.; Liu, S. Polyoxometalate/Chitosan–Electrochemically Reduced Graphene Oxide as Effective Mediating Systems for Electrocatalytic Reduction of Persulfate. *Electrochim. Acta* **2015**, *173*, 540–550.

(235) Toma, F. M.; Sartorel, A.; Iurlo, M.; Carraro, M.; Parisse, P.; Maccato, C.; Rapino, S.; Gonzalez, B. R.; Amenitsch, H.; Da Ros, T.; Casalis, L.; Goldoni, A.; Marcaccio, M.; Scorrano, G.; Scoles, G.; Paolucci, F.; Prato, M.; Bonchio, M. Efficient Water Oxidation at Carbon Nanotube–Polyoxometalate Electrocatalytic Interfaces. *Nat. Chem.* **2010**, *2* (10), 826–831.

(236) Toma, F. M.; Sartorel, A.; Iurlo, M.; Carraro, M.; Rapino, S.; Hoober-Burkhardt, L.; Da Ros, T.; Marcaccio, M.; Scorrano, G.; Paolucci, F.; Bonchio, M.; Prato, M. Tailored Functionalization of Carbon Nanotubes for Electrocatalytic Water Splitting and Sustainable Energy Applications. *ChemSusChem* **2011**, *4* (10), 1447–1451.

(237) Bosch-Navarro, C.; Matt, B.; Izzet, G.; Romero-Nieto, C.; Dirian, K.; Raya, A.; Molina, S. I.; Proust, A.; Guldi, D. M.; Martí-Gastaldo, C.; Coronado, E. Charge Transfer Interactions in Self-Assembled Single Walled Carbon Nanotubes/Dawson–Wells Polyoxometalate Hybrids. *Chem. Sci.* **2014**, *5* (11), 4346–4354.

(238) Jordan, J. W.; Cameron, J. M.; Lowe, G. A.; Rance, G. A.; Fung, K. L. Y.; Johnson, L. R.; Walsh, D. A.; Khlobystov, A. N.; Newton, G. N. Stabilization of Polyoxometalate Charge Carriers via Redox-Driven Nanoconfinement in Single-Walled Carbon Nanotubes. *Angew. Chem. Int. Ed.* **2022**, *61* (8), e202115619.

(239) Jordan, J. W.; Lowe, G. A.; McSweeney, R. L.; Stoppiello, C. T.; Lodge, R. W.; Skowron, S. T.; Biskupek, J.; Rance, G. A.; Kaiser, U.; Walsh, D. A.; Newton, G. N.; Khlobystov, A. N. Host–Guest Hybrid Redox Materials Self-Assembled from Polyoxometalates and Single-Walled Carbon Nanotubes. *Adv. Mater.* **2019**, *31* (41), 1904182.

(240) W. Jordan, J.; Y. Fung, K. L.; T. Skowron, S.; S. Allen, C.; Biskupek, J.; N. Newton, G.; Kaiser, U.; N. Khlobystov, A. Single-Molecule Imaging and Kinetic Analysis of Intermolecular Polyoxometalate Reactions. *Chem. Sci.* **2021**, *12* (21), 7377–7387.

(241) Fernandes, D. M.; Freire, C. Carbon Nanomaterial–Phosphomolybdate Composites for Oxidative Electrocatalysis. *ChemElectroChem* **2015**, *2* (2), 269–279.

(242) Boussema, F.; Haddad, R.; Ghandour, Y.; Belkhiria, M. S.; Holzinger, M.; Maaref, A.; Cosnier, S. Polyoxometalate $[PMo_{11}O_{39}]^{7-}$/Carbon Nanocomposites for Sensitive Amperometric Detection of Nitrite. *Electrochim. Acta* **2016**, *222*, 402–408.

(243) Nunes, M.; Fernandes, D. M.; Rocha, I. M.; Pereira, M. F. R.; Mbomekalle, I.-M.; de Oliveira, P.; Freire, C. Phosphomolybdate@Carbon-Based Nanocomposites as Electrocatalysts for Oxygen Reduction Reaction. *ChemistrySelect* **2016**, *1* (19), 6257–6266.

(244) Wang, T.; Xu, M.; Li, X.; Wang, C.; Chen, W. Highly Dispersed Redox-Active Polyoxometalates' Periodic Deposition on Multi-Walled Carbon Nanotubes for Boosting Electrocatalytic Triiodide Reduction in Dye-Sensitized Solar Cells. *Inorg. Chem. Front.* **2020**, *7* (8), 1676–1684.

(245) Xia, X.; Fan, D.; An, B.; Cai, Y.; Wei, Q. Electrochemical Behavior of Keggin-Type Heteropolyanion Doped Composite of Polyaniline and Multi-Walled Carbon Nanotubes. *J. Mol. Liq.* **2015**, *206*, 335–337.

(246) Yu, S.; Zhao, X.; Su, G.; Wang, Y.; Wang, Z.; Han, K.; Zhu, H. Synthesis and Electrocatalytic Performance of a P-Mo-V Keggin Heteropolyacid Modified Ag@Pt/MWCNTs Catalyst for Oxygen Reduction in Proton Exchange Membrane Fuel Cell. *Ionics* **2019**, *25* (11), 5141–5152.

(247) Zhu, W.; Zhang, R.; Qu, F.; Asiri, A. M.; Sun, X. Design and Application of Foams for Electrocatalysis. *ChemCatChem* **2017**, *9* (10), 1721–1743.

(248) Jia, X.; Streb, C.; Song, Y.-F. Devisable POM/Ni Foam Composite: Precisely Control Synthesis toward Enhanced Hydrogen Evolution Reaction at High PH. *Chem. - Eur. J.* **2019**, *25*, 15548–15554.

(249) Luo, W.; Hu, J.; Diao, H.; Schwarz, B.; Streb, C.; Song, Y.-F. Robust Polyoxometalate/Nickel Foam Composite Electrodes for Sustained Electrochemical Oxygen Evolution at High pH. *Angew. Chem. Int. Ed.* **2017**, *56*, 4941–4944.

(250) Zhang, L.; Ding, X.; Cong, M.; Wang, Y.; Zhang, X. Self-Adaptive Amorphous Co_2P@Co_2P/Co-Polyoxometalate/Nickel Foam as an Effective Electrode for Electrocatalytic Water Splitting in Alk. Electrolyte. *Int. J. Hydrog. Energy* **2019**, *44*, 9203–9209.

(251) Wang, M.; Zhang, L.; He, Y.; Zhu, H. Recent Advances in Transition-Metal-Sulfide-Based Bifunctional Electrocatalysts for Overall Water Splitting. *J. Mater. Chem. A* **2021**, *9* (9), 5320–5363.

(252) Gautam, J.; Liu, Y.; Gu, J.; Ma, Z.; Zha, J.; Dahal, B.; Zhang, L.; Chishti, A. N.; Ni, L.; Diao, G.; Wei, Y. Fabrication of Polyoxometalate Anchored Zinc Cobalt Sulfide Nanowires as a Remarkable Bifunctional Electrocatalyst for Overall Water Splitting. *Adv. Funct. Mater.* **2021**, *31* (46), 2106147.

(253) Ding, Y.; Li, H.; Hou, Y. Robust Polyoxometalate-Loaded Nickel Foam for Electrocatalytic Oxygen Evolution Reaction. *Mater. Lett.* **2018**, *221*, 264–266.

(254) Singh, V.; Ma, P.; Drew, M. G. B.; Niu, J.; Wang, J.; Jin, G.-X. Heterooctamolybdate-Based Clusters $H_3[(Cp^*Rh)_4PMo_8O_{32}]$ and $H_5[Na_2(Cp^*Ir)_4PMo_8O_{34}]$ and Derived Hybrid Nanomaterials with Efficient Electrocatalytic Hydrogen Evolution Reaction Activity. *Inorg. Chem.* **2017**, *56*, 12520–12528.

(255) Wang, Y.; Weinstock, I. A. Polyoxometalate-Decorated Nanoparticles. *Chem. Soc. Rev.* **2012**, *41* (22), 7479.

(256) Guo, S.-X.; Li, F.; Chen, L.; MacFarlane, D. R.; Zhang, J. Polyoxometalate-Promoted Electrocatalytic CO_2 Reduction at Nanostructured Silver in Dimethylformamide. *ACS Appl. Mater. Interfaces* **2018**, *10*, 12690–12697.

(257) Rutkowska, I. A.; Zoladek, S.; Kulesza, P. J. Polyoxometallate-Assisted Integration of Nanostructures of Au and ZrO_2 to Form Supports for Electrocatalytic PtRu Nanoparticles: Enhancement of Their Activity toward Oxidation of Ethanol. *Electrochim. Acta* **2015**, *162*, 215–223.

(258) Zhang, Y.; Bo, X.; Nsabimana, A.; Munyentwali, A.; Han, C.; Li, M.; Guo, L. Green and Facile Synthesis of an Au Nanoparticles@polyoxometalate/Ordered Mesoporous Carbon Tri-Component Nanocomposite and Its Electrochemical Applications. *Biosens. Bioelectron.* **2015**, *66*, 191–197.

(259) Seog, J. H.; Kim, D.; Kim, Y.; Kim, N. S.; Lee, S. B.; Woo Han, S. One-Pot Synthesis of Pd@Pt Core-Shell Nanocrystals for Electrocatalysis: Control of Crystal Morphology with Polyoxometalate. *CrystEngComm* **2016**, *18*, 6029–6034.

(260) Zhang, C.; Hong, Y.; Dai, R.; Lin, X.; Long, L.-S.; Wang, C.; Lin, W. Highly Active Hydrogen Evolution Electrodes via Co-Deposition of Platinum and Polyoxometalates. *ACS Appl. Mater. Interfaces* **2015**, *7*, 11648–11653.

(261) Kim, D.; Seog, J. H.; Kim, M.; Yang, M. H.; Gillette, E.; Lee, S. B.; Han, S. W. Polyoxometalate-Mediated One-Pot Synthesis of Pd Nanocrystals with Controlled Morphologies for Efficient Chemical and Electrochemical Catalysis. *Chem. - Eur. J.* **2015**, *21*, 5387–5394.

(262) Zhu, Z.; Lu, C.; Wang, J.; Zhang, X.; Cai, N.; Xue, Y.; Chen, W.; Yan, Z.; Yang, X.; Yu, F.; Yang, W.; Tian, Q. Polyoxometalate Modified Carbon Supported Pd-Cu Bimetallic Catalyst for Formic Acid Oxidation. *Int. J. Electrochem. Sci.* **2019**, *14*, 11019–11034.

(263) Khadempir, S.; Ahmadpour, A.; Hamed Mosavian, M. T.; Ashraf, N.; Bamoharram, F. F.; Fernandez-Pacheco, R.; de la Fuente, J. M.; Mitchell, S. G. Mechanistic Insights into the Activation Process in Electrocatalytic Ethanol Oxidation by Phosphomolybdic Acid-Stabilised Palladium(0) Nanoparticles (PdNPs@PMo_{12}). *RSC Adv.* **2016**, *6*, 5359–5366.

(264) Xie, X.; Nie, Y.; Chen, S.; Ding, W.; Qi, X.; Li, L.; Wei, Z. A Catalyst Superior to Carbon-Supported-Platinum for Promotion of the Oxygen Reduction Reaction: Reduced-Polyoxometalate Supported Palladium. *J. Mater. Chem. A* **2015**, *3*, 13962–13969.

(265) Zang, D.; Huang, Y.; Li, Q.; Tang, Y.; Wei, Y. Cu Dendrites Induced by the Anderson-Type Polyoxometalate $NiMo_6O_{24}$ as a Promising Electrocatalyst for Enhanced Hydrogen Evolution. *Appl. Catal. B Environ.* **2019**, *249*, 163–171.

(266) Sadakane, M.; Steckhan, E. Electrochemical Properties of Polyoxometalates as Electrocatalysts. *Chem. Rev. Wash. C* **1998**, *98*, 219–237.

(267) Guo, S.-X.; Li, F.; Chen, L.; MacFarlane, D. R.; Zhang, J. Polyoxometalate-Promoted Electrocatalytic CO_2 Reduction at Nanostructured Silver in Dimethylformamide. *ACS Appl. Mater. Interfaces* **2018**, *10*, 12690–12697.

(268) Sun, K.; Shen, S.; Liang, Y.; Burrows, P. E.; Mao, S. S.; Wang, D. Enabling Silicon for Solar-Fuel Production. *Chem. Rev.* **2014**, *114* (17), 8662–8719.

(269) Yao, T.; An, X.; Han, H.; Chen, J. Q.; Li, C. Photoelectrocatalytic Materials for Solar Water Splitting. *Adv. Energy Mater.* **2018**, *8* (21), 1800210.

(270) White, J. L.; Baruch, M. F.; Pander, J. E.; Hu, Y.; Fortmeyer, I. C.; Park, J. E.; Zhang, T.; Liao, K.; Gu, J.; Yan, Y.; Shaw, T. W.; Abelev, E.; Bocarsly, A. B. Light-Driven Heterogeneous Reduction of Carbon Dioxide: Photocatalysts and Photoelectrodes. *Chem. Rev.* **2015**, *115* (23), 12888–12935.

(271) Kumar, B.; Llorente, M.; Froehlich, J.; Dang, T.; Sathrum, A.; Kubiak, C. P. Photochemical and Photoelectrochemical Reduction of CO_2. *Annu. Rev. Phys. Chem.* **2012**, *63* (1), 541–569.

(272) Wrighton, M. S. Thermodynamics and Kinetics Associated with Semiconductor-Based Photoelectrochemical Cells for the Conversion of Light to Chemical Energy. *Pure Appl. Chem.* **1985**, *57* (1), 57–68.

(273) Laurans, M.; Trinh, K.; Dalla Francesca, K.; Izzet, G.; Alves, S.; Derat, E.; Humblot, V.; Pluchery, O.; Vuillaume, D.; Lenfant, S.; Volatron, F.; Proust, A. Covalent Grafting of Polyoxometalate Hybrids onto Flat Silicon/Silicon Oxide: Insights from POMs Layers on Oxides. *ACS Appl. Mater. Interfaces* **2020**, *12* (42), 48109–48123.

(274) Volatron, F.; Noël, J.-M.; Rinfray, C.; Decorse, P.; Combellas, C.; Kanoufi, F.; Proust, A. Electron Transfer Properties of a Monolayer of Hybrid Polyoxometalates on Silicon. *J. Mater. Chem. C* **2015**, *3* (24), 6266–6275.

(275) Laurans, M.; Dalla Francesca, K.; Volatron, F.; Izzet, G.; Guerin, D.; Vuillaume, D.; Lenfant, S.; Proust, A. Molecular Signature of Polyoxometalates in Electron Transport of Silicon-Based Molecular Junctions. *Nanoscale* **2018**, *10* (36), 17156–17165.

(276) The surface states are electronic energy levels created in the forbidden gap region of silicon and are capable of transferring charges with the semiconductor and contact solution.

(277) Yablonovitch, E.; Allara, D. L.; Chang, C. C.; Gmitter, T.; Bright, T. B. Unusually Low Surface-Recombination Velocity on Silicon and Germanium Surfaces. *Phys. Rev. Lett.* **1986**, *57* (2), 249–252.

(278) Bansal, A.; Li, X.; Lauermann, I.; Lewis, N. S.; Yi, S. I.; Weinberg, W. H. Alkylation of Si Surfaces Using a Two-Step Halogenation/Grignard Route. *J. Am. Chem. Soc.* **1996**, *118* (30), 7225–7226.

(279) Gurrentz, J. M.; Rose, M. J. Covalent Attachment of Polyoxometalates to Passivated Si(111) Substrates: A Stable and Electronic Defect-Free Si|POM Platform. *J. Phys. Chem. C* **2021**, *125* (26), 14287–14298.

(280) Seger, B.; Herbst, K.; Pedersen, T.; Abrams, B.; Vesborg, P. C. K.; Hansen, O.; Chorkendorff, I. Mo_3S_4 Clusters as an Effective H_2 Evolution Catalyst on Protected Si Photocathodes. *J. Electrochem. Soc.* **2014**, *161* (12), H722–H724.

(281) Fu, D.; Fabre, B.; Loget, G.; Mériadec, C.; Ababou-Girard, S.; Cadot, E.; Leclerc-Laronze, N.; Marrot, J.; de Ponfilly, Q. Polyoxothiometalate-Derivatized Silicon Photocathodes for Sunlight-Driven Hydrogen Evolution Reaction. *ACS Omega* **2018**, *3* (10), 13837–13849.

(282) Smortsova, Y.; Falaise, C.; Fatima, A.; Ha-Thi, M.; Méallet-Renault, R.; Steenkeste, K.; Al-Bacha, S.; Chaib, T.; Assaud, L.; Lepeltier, M.; Haouas, M.; Leclerc, N.; Pino, T.; Cadot, E. Time-Resolved Spectroscopy and High-Efficiency Light-Driven Hydrogen Evolution of a $\{Mo_3S_4\}$-Containing Polyoxometalate-Based System. *Chem. – Eur. J.* **2021**, *27* (68), 17094–17103.

(283) Hou, Y.; Abrams, B. L.; Vesborg, P. C. K.; Björketun, M. E.; Herbst, K.; Bech, L.; Setti, A. M.; Damsgaard, C. D.; Pedersen, T.; Hansen, O.; Rossmeisl, J.; Dahl, S.; Nørskov, J. K.; Chorkendorff, I. Bioinspired Molecular Co-Catalysts Bonded to a Silicon Photocathode for Solar Hydrogen Evolution. *Nat. Mater.* **2011**, *10* (6), 434–438.

(284) Ding, Q.; Zhai, J.; Cabán-Acevedo, M.; Shearer, M. J.; Li, L.; Chang, H.-C.; Tsai, M.-L.; Ma, D.; Zhang, X.; Hamers, R. J.; He, J.-H.; Jin, S. Designing Efficient Solar-Driven Hydrogen Evolution Photocathodes Using Semitransparent MoQ_xCl_y (Q = S, Se) Catalysts on Si Micropyramids. *Adv. Mater.* **2015**, *27* (41), 6511–6518.

(285) Truong, T.-G.; Mériadec, C.; Fabre, B.; Bergamini, J.-F.; de Sagazan, O.; Ababou-Girard, S.; Loget, G. Spontaneous Decoration of Silicon Surfaces with MoO_x Nanoparticles for the Sunlight-Assisted Hydrogen Evolution Reaction. *Nanoscale* **2017**, *9* (5), 1799–1804.

(286) Kim, H.; Bae, S.; Jeon, D.; Ryu, J. Fully Solution-Processable Cu_2O-$BiVO_4$ Photoelectrochemical Cells for Bias-Free Solar Water Splitting. *Green Chem.* **2018**, *20*, 3732–3742.

(287) Kang, D.; Kim, T. W.; Kubota, S. R.; Cardiel, A. C.; Cha, H. G.; Choi, K.-S. Electrochemical Synthesis of Photoelectrodes and Catalysts for Use in Solar Water Splitting. *Chem. Rev.* **2015**, *115* (23), 12839–12887.

(288) Morales-Guio, C. G.; Liardet, L.; Mayer, M. T.; Tilley, S. D.; Grätzel, M.; Hu, X. Photoelectrochemical Hydrogen Production in Alkaline Solutions Using Cu_2O Coated with Earth-Abundant Hydrogen Evolution Catalysts. *Angew. Chem. Int. Ed.* **2015**, *54* (2), 664–667.

(289) Hu, Z.; Lin, Z.; Su, J.; Zhang, J.; Chang, J.; Hao, Y. A Review on Energy Band-Gap Engineering for Perovskite Photovoltaics. *Sol. RRL* **2019**, *3* (12), 1900304.

(290) Fang, W.; Yan, D.; Tao, R.; Sun, Z.; Li, F.; Xu, L. Polyoxometalates Acting as a Hole-Transfer Mediator and Crystallization Accelerant in a Perovskite Photoanode for the Photoelectrocatalytic Oxidation of Benzene into Phenol. *Dalton Trans.* **2020**, *49* (29), 10084–10090.

(291) Lauinger, S. M.; Piercy, B. D.; Li, W.; Yin, Q.; Collins-Wildman, D. L.; Glass, E. N.; Losego, M. D.; Wang, D.; Geletii, Y. V.; Hill, C. L. Stabilization of Polyoxometalate Water Oxidation Catalysts on Hematite by Atomic Layer Deposition. *ACS Appl. Mater. Interfaces* **2017**, *9*, 35048–35056.

(292) Lauinger, S. M.; Sumliner, J. M.; Yin, Q.; Xu, Z.; Liang, G.; Glass, E. N.; Lian, T.; Hill, C. L. High Stability of Immobilized Polyoxometalates on TiO_2 Nanoparticles and Nanoporous Films for Robust, Light-Induced Water Oxidation. *Chem. Mater.* **2015**, *27* (17), 5886–5891.

(293) Xu, X.-T.; Pan, L.; Zhang, X.; Wang, L.; Zou, J.-J. Rational Design and Construction of Cocatalysts for Semiconductor-Based Photo-Electrochemical Oxygen Evolution: A Comprehensive Review. *Adv. Sci.* **2019**, *6* (2), 1801505.

(294) Park, Y.; McDonald, K. J.; Choi, K.-S. Progress in Bismuth Vanadate Photoanodes for Use in Solar Water Oxidation. *Chem. Soc. Rev.* **2013**, *42* (6), 2321–2337.

(295) Xi, L.; Jin, Z.; Sun, Z.; Liu, R.; Xu, L. Enhanced Photoelectrocatalytic Performance for Water Oxidation by Polyoxometalate Molecular Doping in $BiVO_4$ Photoanodes. *Appl. Catal. Gen.* **2017**, *536*, 67–74.

(296) Liu, J.; Wang, H.; Antonietti, M. Graphitic Carbon Nitride "Reloaded": Emerging Applications beyond (Photo)Catalysis. *Chem. Soc. Rev.* **2016**, *45* (8), 2308–2326.

(297) Yousefi, M.; Eshghi, H.; Karimi-Nazarabad, M.; Farhadipour, A. P_5W_{30}/g-C_3N_4 Heterojunction Thin Film with Improved Photoelectrochemical Performance for Solar Water Splitting. *New J. Chem.* **2020**, *44* (46), 20470–20478.